

University of Texas at Arlington

MavMatrix

Mechanical and Aerospace Engineering
Dissertations

Mechanical and Aerospace Engineering
Department

2023

On the Development of a Sensing System Methodology to Evaluate the Viscoelastic Properties of Soft Tissues as a Means of Disease Prognosis

Shashank S. Kumat

Follow this and additional works at: https://mavmatrix.uta.edu/mechaerospace_dissertations



Part of the [Aerospace Engineering Commons](#), and the [Mechanical Engineering Commons](#)

Recommended Citation

Kumat, Shashank S., "On the Development of a Sensing System Methodology to Evaluate the Viscoelastic Properties of Soft Tissues as a Means of Disease Prognosis" (2023). *Mechanical and Aerospace Engineering Dissertations*. 413.

https://mavmatrix.uta.edu/mechaerospace_dissertations/413

This Dissertation is brought to you for free and open access by the Mechanical and Aerospace Engineering Department at MavMatrix. It has been accepted for inclusion in Mechanical and Aerospace Engineering Dissertations by an authorized administrator of MavMatrix. For more information, please contact leah.mccurdy@uta.edu, erica.rousseau@uta.edu, vanessa.garrett@uta.edu.

On the Development of a Sensing System Methodology to Evaluate the Viscoelastic Properties of Soft Tissues as a Means of Disease Prognosis

Presented to the Faculty of the Graduate School of

The University of Texas at Arlington

In Partial Fulfillment of the Requirements of the Degree of

Doctor of Philosophy

by

Shashank Sanjay Kumat

December 2023

Copyright © by SHASHANK SANJAY KUMAT 2023

All Rights Reserved



Acknowledgments

I want to utilize this space, to recognize some of the influencing people who have helped me in the recent past years of my research. Foremost and above all, I am eternally grateful for the lifelong sacrifices my father and mother have made to support me in achieving my dreams. I am grateful for the nourishment they have provided me. I want to thank my wife for her love, and support during difficult times and for keeping me motivated time and again. My brother Dr. Kshitij Kumat, M.D. has contributed to my success by not only taking care of my parents in difficult times but also spending his time with me in thoughtful conversations.

I would like to express my gratitude to my supervising professor Dr. Panos Shiakolas for accepting me as his student, and for his extensive support and guidance in all the stages of my educational research career. I wish to thank my committee members, Dr. Bo P. Wang, Dr. Ashfaq Adnan, Dr. Jacqueline Michael, and Dr. Prashanth Ravi for their feedback, comments and serving on my committee. I also want to extend my gratitude to Dr. James Grover, for appointing me as his research assistant and providing me financial support and scholarships and letting me be a part of CIRTL-UTA.

I would like to appreciate the help provided by the staff members at the Mechanical Engineering Department, University of Texas at Arlington. I am thankful to Mr. Kermit Beird, Mr. Rex Winfrey, Mr. Scott Eichmann, Mr. David MacNeil, and Mr. Michael Baker for their help in developing the prototypes of the micro-force sensor and/or characterization fixtures. I also want to thank Ms. Wendy Ryan for her administrative assistance. Along with that I also want to recognize and thank all the participants who volunteered in the tissue characterization experiments.

I would like to thank my team at mMARS lab (Dr. Samson Adejokun, Tushar Saini, Sudip

Hazra, and Abdul Rahman Abdul Hafiz, Rohan Bhandikeri, and Makrand Karbhari, Dr. M.D. Abu Hasan, and Dr. Christopher Abrego) for the engaging group discussions and challenging my thought process.

Lastly, I wish to extend my appreciation to all my friends and family for their encouragement and unwavering support.

Abstract

Identification of tissue viscoelastic properties could provide valuable information for assessing its healthiness or disease state. Current technologies present challenges to access and perform localized tissue assessment in confined spaces in the human body through contact indentation/palpation. As such, there is a need for a diagnostic system capable of measuring tissue relaxation response at the local site by accessing the tissue through a natural orifice. This dissertation presents a strain gauge based uniaxial micro-force sensor, part of the aforementioned system, capable of measuring tissue response data in confined human space environments. A sensing system design methodology is developed and presented. The sensor operational requirements are used to define design specifications and constraints. An exhaustive search discrete optimization approach is formulated, and finite element analysis is employed to identify optimal sensor components design values. A micro-force sensor with an overall diameter of approximately 3.5mm was prototyped and characterized. Characterization test beds were developed in-house to evaluate the performance of the prototyped micro-force sensor using experimentally collected equivalent force data. The performance of the sensor as it relates to its load-bearing capacity, resolution, sensitivity, accuracy, precision, repeatability error, and hysteresis were evaluated to be 1.07N , 0.13mN , $859.7\mu\epsilon/\text{N}$, $\pm 28.6\text{mN}$, $87.2\%(23\text{mN})$, $\pm 3.13\% (\pm 25\text{mN})$, and 118mN respectively.

The characterized micro-force sensor was subsequently employed to perform in vivo tissue characterization experiments on the human forearm through normal contact palpation at different control indentation depths and indentation rates according to approved Institutional Review Board protocol 2023-0306. Tissue characterization experiments were performed on 30+ participants ranging in age (20 to 79 years old), race (Asian, Caucasian, Others), gender (male, female), and

arm strength training or not. A three-element Maxwell-Wiechert viscoelastic model, commonly used for soft tissue characterization, was employed to evaluate the viscoelastic parameters of instantaneous shear modulus and relaxation time constant. The analysis of the results showed that the tissue became compliant as one aged. No identifiable differences were observed for the viscoelastic properties of the tissue as a function of race. The result revealed that females exhibited relatively stiffer tissue. Individuals associated with arm strength training had stiffer tissue. The experimental results provide confidence to employ the sensor to distinguish healthy from diseased tissue *in vivo*. The dissertation concludes with the importance of this research as a component of a diagnostic system along with a discussion on future research direction.

Table of Contents

Acknowledgments	iii
Abstract	v
List of Figures	ix
List of Tables	xii
1 Introduction	1
1.1 Introduction to Confined Space Applications	3
1.2 Motivation	4
1.3 Current Technologies: Diagnostic Methods	5
1.4 Tissue Viscoelastic Models	8
1.5 Significance and Contribution of Research	12
1.6 Dissertation Overview	13
2 Micro-Force Sensor Design and Fabrication	15
2.1 Introduction to Sensor Design Methodology	15
2.1.1 Force Sensor Characteristics	16
2.1.2 Design Methodology	19
2.2 Desired Design Specifications	22
2.3 Conceptual Design	24
2.4 Design Optimization	31
2.4.1 Exhaustive Search Algorithm	35
2.4.2 Parametric Finite Element Simulation	36
2.4.3 Optimal Design	41
2.5 Micro-Force Sensor Fabrication Methodologies	44
2.5.1 Manufacturing of Sensor Housing Components	44
2.5.2 Manufacturing of Sensing Element	45
2.5.3 Micro-Force Sensor Assembly	48
3 Micro-Force Sensor Characterization	50
3.1 Introduction	50
3.2 Characterization Setup-I	51
3.2.1 Resolution-I	53
3.2.2 Sensitivity-I	54

3.2.3	Accuracy-I	56
3.2.4	Precision-I	58
3.3	Characterization Setup-II	60
3.3.1	Sensitivity-II	65
3.3.2	Resolution-II	68
3.3.3	Accuracy-II	69
3.3.4	Precision-II	70
3.3.5	Repeatability-II	71
3.3.6	Hysteresis-II	72
3.4	Performance Matrix Summary	74
4	Tissue Characterization	75
4.1	Introduction	75
4.2	Mathematical Formulation of Viscoelastic Model	76
4.3	Current Technologies: Tissue Characterization	81
4.4	Manual Characterization Setup- Results and Discussion	84
4.4.1	Results and Discussion	86
4.5	Automated Characterization Setup, Results and Discussion	87
4.5.1	Process Parameters Effects on Viscoelastic Constants	89
4.5.2	Results and Discussion of Viscoelastic Properties of Tissue	92
4.5.3	Effect of Indentation Depth	93
4.5.4	Effect of Strain Rate	95
4.5.5	High-Indentation Depth and Strain Rate	96
4.5.6	Effect of Age	98
4.5.7	Effect of Race	99
4.5.8	Effect of Gender	100
4.5.9	Effect of Arm Strength Training	101
4.6	Summary of Tissue Characterization Results	103
5	Conclusions and Future Directions	104
5.1	Conclusions	104
5.2	Recommendations for Future Direction	106
Appendix A		108
A.1	Matlab snippet to post process and develop sensor characterization plots	108
Appendix B		119
B.1	Matlab code to evaluate viscoelastic coefficients using three element Maxwell-Wiechert model	119
Appendix C		130
C.1	LabVIEW Stepper-Motor Control VI	130
C.2	LabVIEW Servo-Motor Control VI for Tissue characterization	131
Bibliography		132

List of Figures

1.1	Anatomical model with organs located in the confined space of lower abdomen	3
1.2	Bladder access using a flexible cystoscope via urinary meatus and urethra	4
2.1	Characteristics to be considered for the development of a force sensor for medical diagnostics purposes	17
2.2	Sensing system methodology for biomedical applications	20
2.3	Schematic models of (a) metal foil strain gauge with total dimensions and active grid dimensions (b) sensor base component with a bounding box feature provided to encapsulate sensing element, slot feature as a guide-way, and block feature for its assembly with a micro-robot	26
2.4	Solid model of the developed sensor design concept #1, (a) Section view of the micro-force sensor subsystem, (b) Schematic of the micro-force sensor with key design parameters as bend radius R , bend angle θ , and thickness t , as well as an inset with tentative strain gauge attachment location	31
2.5	Aluminum sheet with thickness 0.3mm bent at a 90° angle with a bend radius 0.1mm developed a crack on the outer surface	34
2.6	Process flow diagram to obtain optimal design from the discrete design points using exhaustive search criteria	37
2.7	FE-based model with (a) half model cut at the plane of symmetry (b) Boundary conditions (c) an overview of the generated mesh	39
2.8	FE-based model with (a) location at which strain will be evaluated, (b) von Mises stress for the beam element with manufactured design variables, (c) Normal elastic strain distribution along the global Y-axis, due to an applied load of $0.5N$	40
2.9	Cost of the objective function evaluated for 129 design points, along with the one for the manufactured sensing element, where the overlaying circle represents the design yielding a factor of safety greater than 3.50	42
2.10	Effect of bend radius and bend angle on the cost of the objective function for feasible design points and fabricated beam ($Beam_{fab}$) with 0.3mm thick sensing element	43
2.11	Actual scale cured (a) sensor head component fabricated in different orientations to highlight good and bad orientations and defects (b) sensor base component fabricated in different orientations	45
2.12	Sensing element with attached strain gauge; (a) side view orientation showing beam length, bend angle, and radius of curvature, (b) front view orientation showing dimensions of width and mounting hole of the beam (c) front view of the sensing element with the strain gauge attached in an orientation that caused wire harnessing issues	47

2.13	Fabricated micro-force components (a) Exploded view of manufactured components that will be used to develop the performance matrix of the micro-force sensor, (b) assembled micro-force sensor without sensor element with a pencil tip alongside for size comparison	49
3.1	Sensor calibration platform with micro-force sensor encompassed in a fixture along with National Instruments based data acquisition system and a sample graphical output generated using National Instruments LabVIEW™ interface when loaded with a dead weight	51
3.2	Micro-force sensor response for characterization experiments for 15 different loading and unloading stages	55
3.3	Micro-force sensor sensitivity plot with applied load ranging from 0.09 to 1.07 N (9.63 to 109.68 grams). A large variation 132.2, 108.3, 89.4 and 296.1 $\mu\epsilon$ was recorded at loading conditions 0.37, 0.62, 0.68, and 0.94N respectively	56
3.4	Sensitivity response for the FE-based simulation and the experimental data over full scale range of the micro-force sensor	57
3.5	Micro-force sensor response for all four experiments sorted in ascending loading order with loading stage 1 – 15 corresponding to an applied load of 0.09N, 0.15N, 0.20N, 0.29N, 0.37N, 0.41N, 0.48N, 0.57N, 0.62N, 0.68N, 0.75N, 0.79N, 0.87N, 0.94N and 1.07N respectively	59
3.6	Micro-force sensor response as a time series graph for 0.29N obtained from all four characterization experiments	60
3.7	Modified calibration platform with micro-force sensor encompassed in a fixture	62
3.8	Front panel screen capture for position and velocity control of the stepper motor	62
3.9	DC servo motor controlled calibration platform with micro-force sensor encompassed within the movable plate fixture an a load cell attached at the base	64
3.10	Process flow diagram of the characterization setup, with input signal generated through NI LabVIEW™ and sent to NI myRIO microcontroller, which is then amplified and fed to the linear servo actuator, the data from the load cell and the micro force sensor is recorded and stored for postprocessing	65
3.11	Average response data from the micro-force sensor as a function of the linear actuator displacement	66
3.12	Sensitivity responses for the FE-based simulation and experimental data as a function of force experienced by the load cell	67
3.13	Load raw data collected from the load cell and postprocessed micro-force sensor as a time series plot (negative values indicate compressive loads)	69
3.14	Sensor precision calculation based on evaluated force from measured ΔR_{SG} as a function of applied displacement for each of the three experiments	71
3.15	Sensor repeatability evaluated from measured resistance changes ΔR_{SG} as a function of applied displacement for the three experiments	73
3.16	Postprocessessed hysteresis response from the calibrated micro-force sensor	74
4.1	Three element Maxwell Wiechert model with free body diagram	77
4.2	Testbed for evaluation of in vivo forearm tissue relaxation response	85

4.3	Representative sensor response due to indentation of forearm tissue with the inset showing the tissue relaxation response characterization equation	87
4.4	Testbed for in vivo human forearm tissue characterization with linear actuator	88
4.5	Representative actuator position and velocity profiles with a desired indentation rate of $1mm/s$ and indentation depth of $5mm$	89
4.6	Process flow diagram to perform indentation experiments and proposed outcomes	90
4.7	Representative process flow diagram, presenting tissue indentation performed on selected experiment followed by postprocessing to obtain viscoelastic properties of soft tissue of a participant	93
4.8	Instantaneous shear modulus and time constant as a function of indentation depth for all strain rates for the forearm for the 30 participants	94
4.9	Instantaneous shear modulus and time constant for different strain rates for all depths applied on the forearm tissue for the 30 participants	96
4.10	Tissue characterization experimental response of a participant for low, medium and high indentation depths and strain rates. (Note: ID is the indentation depth and SR is the strain rate)	97
4.11	Effect of age on the viscoelastic properties of soft tissue	98
4.12	Effect of race (Asian, Caucasian, and Others) on the viscoelastic properties of soft tissue	100
4.13	Effect of gender on the viscoelastic properties of soft tissue	101
4.14	Effect of arm strength training on the viscoelastic properties of soft tissue	102
C.1	Stepper motor control block diagram	130
C.2	Servo motor control front panel	131

List of Tables

1.1	Summary of existing technologies with limitations	9
1.2	Viscoelastic models with mathematical representation along with their governing equation, creep compliance and relaxation modulus	11
2.1	Micro-force sensor design specifications	23
2.2	Comparison of as-designed and as-fabricated dimensions of the 3D printed components of the sensor	46
3.1	Precision matrix of the sensor evaluated using results obtained from characterization setup-I experiments	61
3.2	Precision matrix of the strain gauge-based sensor evaluated using results obtained from the three calibration experiments using characterization setup-II	72
3.3	Performance Matrix of the Prototyped Micro-Force Sensor	74
4.1	Factors and levels investigated for tissue characterization	94

CHAPTER 1

INTRODUCTION

Medicine has long used tissue/organ palpation, a subjective technique, for assessing the health of an organ [1, 2, 3, 4]. The use of quantitative measurements as opposed to subjective assessments established significant improvements in diagnosing an underlying condition of healthiness of an individual. Viscoelasticity has proven to be an innate property of tissue and its biomechanical characteristics must be investigated concurrently when evaluating the disease state. More specifically, several human illnesses or disease phases have been connected to the cell mechanics [5, 6, 7, 8]. Numerous soft tissues, including the breast, kidney, liver, and muscles have been investigated for their viscoelasticity as a diagnostic biomarker [9, 10, 11, 12]. Viscoelasticity has, however, only just begun to be given significant consideration in biological settings, encompassing both healthy and diseased states.

Recent advancements in the medical device industry have prompted to scrutinize the diagnosis procedure to evaluate the diseased state of internal organs. Traditional tissue assessment methodology comprises palpation, biopsy, and visual assessment. Hsu et al. emphasized the importance of abdominal palpation in assessing patients with acute abdominal pain [13]. They introduced an integrated system that combines force sensing and position tracking during palpation. Clinical trials were performed on healthy participants and demonstrated the potential to quantitatively obtaining force measurements during abdominal palpation. A study conducted by Czech et al. over 134 patients demonstrated the impact of performing bimanual palpation over imaging/visual aid [14]. The study assessed the accuracy of examination under anesthesia (EUA) for clinical T staging in

patients with bladder cancer undergoing cystectomy. Clinical T staging results were compared to pathological T staging, and the results suggested that bimanual palpation was a valuable clinical staging tool for diagnosing bladder cancer. Culmer et al. developed a laparoscopic palpation device that presents the need for developing a haptic feedback system during minimally invasive surgical procedures [15]. In their study, they discussed the importance as well as methods of tissue palpation to assess tissue properties including, size, shape, texture, consistency, and anatomical relationships. Although important, these methods are highly subjective and would require specific skill-set before any conclusive outcomes can be drawn. According to their findings, minimally invasive surgical procedures presents potential benefits but incur from challenges due to the lack of tactile feedback. Zhu et al. conducted a review and assessed various methods for detecting bladder cancer [16]. They analyzed the sensitivity (true positive/cancer cases) and specificity (true negative/non cancer cases) data that were collected from groups of patients. They reviewed nine research articles for urine markers with a total number of 3272 participants, and five articles for cystoscopy with a total number of 690 patients. They found that urine markers and cystoscopy had the highest sensitivity and specificity of 97.2% and 97% respectively. However, these methodologies lack the ability to obtain localized assessments of the healthiness of organs. Moreover, these diagnostic means present a challenge as it relates to performing in vivo localized examinations.

While ex vivo measurements to characterize a tissue sample is a relatively common practice, it is associated with several shortcomings. This includes the need for surgical intervention to excise the tissue from target site and the necessity to preserve the tissue sample. Additionally, ex vivo assessments may result in alterations to the biomechanical properties of soft tissue compared to in vivo measurements.

1.1 Introduction to Confined Space Applications

The human bladder is a distensible hollow sac-like organ in the lower abdomen that retains urine.

Figure 1.1 is a pictorial view of the human anatomical model highlighting various organs in the lower abdominal region.

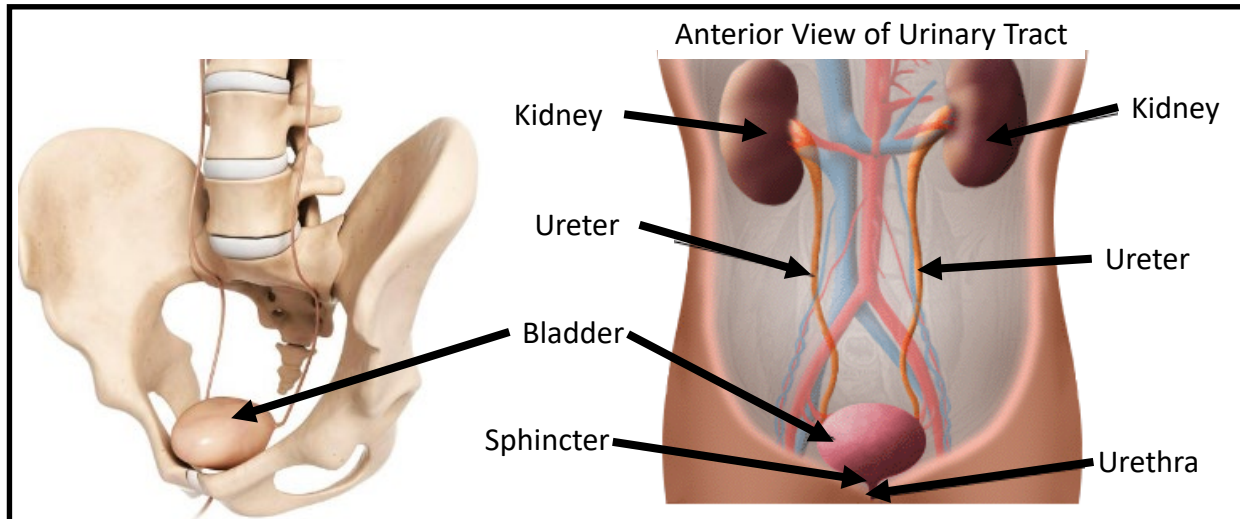


Figure 1.1: Anatomical model with organs located in the confined space of lower abdomen [17, 18]

The bladder is located in the pelvic cavity and supported by the pelvic bones from the bottom and either side. The human bladder could be accessed via a natural orifice from the urinary meatus which leads to the urethra. Figure 1.2 presents a picture of a cystoscope entering the urinary meatus, through the urethra to reach the interior bladder wall for visual inspection [19]. Accessing the interior bladder enforces a need to perform dexterous manipulation of the diagnostics tool. Accordingly it will be critical to develop a system that could access the internal bladder wall through natural openings in the human body, while reducing patient trauma and improving comfort to palpate localized internal tissue surface anywhere in the bladder and collect tissue relaxation response.

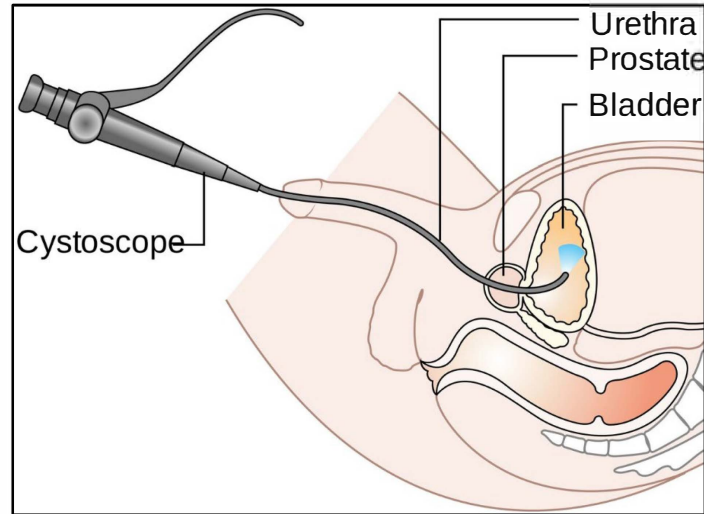


Figure 1.2: Bladder access using a flexible cystoscope via urinary meatus and urethra [20]

1.2 Motivation

Some of the common abnormalities relating to the bladder are cystitis, urinary incontinence, over-active bladder, interstitial cystitis, and bladder cancer. Bladder cancer is the fourth most common cancer in males [21]. About 81,180 (61,700 in men and 19,480 in women) new bladder cancer cases were recorded in the year of 2022, which is estimated to increase to about 82,290 (about 62,420 in men and 19,870 in women) in 2023 in the US alone [21, 22]. The mortality due to bladder cancer was recorded at 17,100 ($\approx 21\%$) (12,120 in men and 4,980 in women) in 2022 while it is estimated to drop to 16,710 ($\approx 20\%$) (about 12,160 in men and 4,550 in women) in 2023 [21, 22]. About 9 out of 10 individuals over the age of 55 are more likely to be diagnosed with bladder cancer [21].

The tumor is usually diagnosed in the inner layer of the bladder wall in about half of all bladder cancer cases [21]. Hence, physicians cannot depend solely on visual cues to detect early-stage bladder anomalies. A quantitative palpation record of the localized viscoelasticity of the bladder

wall tissue may offer a more accurate diagnosis. Clark et al. reported that for an approximately 82,532 reported newly diagnosed bladder cancer patients in 2021, a projected total cost of treatment was US \$2.5 billion [23]. Clark et al. suggested implementation of more efficient treatment at an earlier stage of the disease may aid delay recurrence or progression of bladder cancer, potentially improving the effects of the economic impact associated with the condition. According to studies conducted by Milsom et al., and Coyne et al. the estimated total national cost due to overactive bladder with urinary incontinence in 2007 was US \$65.9 billion [24, 25]. As such, the ability to test and keep track of quantitative time history data could provide the means for early stage diagnosis and assess potential onset of disease progression. Subsequently, a need arises to diagnose abnormalities in the bladder at an early stage or as disease progresses.

1.3 Current Technologies: Diagnostic Methods

A study conducted by Ansardamavandi et al. reported on the impact of quantification of cancerous breast tissue by employing atomic force microscopy (AFM) [26]. Using the information collected by performing AFM to characterize the layer of malignant breast tissue, a fuzzy logic algorithm was implemented to evaluate the mechanical stiffness of the tissue. It was reported that when breast cancer progresses, the cellular region of the tissue softens, while the fibrous region hardens. Studies conducted by Kaur et al., Prevost et al. and Ottensmeyer et al. reported that the viscoelastic properties obtained through in vivo measurements differ from those obtained through in vitro measurements [27, 28, 29]. Current technologies are limited and experience difficulties in quantitatively evaluating in vivo, in situ tissue viscoelastic properties. Evaluating the tissue properties in their natural form is desirable for obtaining accurate representations of the viscoelastic response

[29]. However, due to accessibility, variability, and uncontrolled boundary condition difficulties this could be challenging to obtain. Moreover, obtaining in vivo viscoelastic measurements could require an incision on the surface of the body to access the host organ via minimally invasive or open surgical procedures [30, 31]. Measurement of viscoelastic properties of the tissue in vivo located in confined space accessed via natural orifice such as the ear, nose, mouth, urinary meatus, vaginal and rectal openings possesses a challenge due to factors relating to the device to access the target tissue, the sensor to interact with and interrogate the tissue, the overall dimensions of the instrumentation, and the ability to record real-time data from the sensor. Barnes et al. empirically analyzed the viscoelastic properties of tumorous and normal bladder tissue and compared their storage modulus (viscoelastic property derived from compression testing) [32]. They reported that normal tissue has a higher storage modulus than malignant one. Barnes et al. emphasize that there are currently no instruments available to quantitatively classify viscoelastic properties of the bladder tissue and that if such a device could be developed, it may be a preferable solution in comparison to cystoscopy, biopsy or cross-sectional imaging. Puangmali et al. designed and presented a 3-axis distal force sensor for minimally invasive surgical palpation, particularly during laparoscopic interventions [33]. One of their goals for designing this sensor was to offer a quantitative evaluation of the viscoelastic properties of the tissues undetectable by visual methods like magnetic resonance imaging (MRI) which suffers from identifying small-sized tumors (typically $< 1\text{cm}$ diameter). This sensor design was based upon an optical sensing system, having an outside diameter of 5mm with the capability of being able to measure axial and radial loads of $\pm 3\text{N}$ and $\pm 1.5\text{N}$ respectively. The resolution of the sensor was evaluated to be 0.02N . Lee et al. presented a polydimethylsiloxane (PDMS)-based capacitive force sensor that can measure both normal and shear forces [34]. This tactile sensor was designed to simulate human perception

during complex manipulations. The sensor full range scale was listed as $10mN$ in all three directions, with an axial sensitivity of $2.9\%/mN$. The size of the sensor was measured to be a square with planar dimensions of $22mm$. Polygerinos et al. outlined the design and working prototype of a fiber optics-based micro-force sensor for cardiac catheterizing procedures [35]. Their objective was to provide a remedy for patients undergoing minimally invasive surgery as it relates to patient trauma and rapid recovery. The force sensor had an overall diameter of $4.00mm$ and could withstand an axial load of $1N$. Any force beyond this would result in permanent deformation of their sensor, thus limiting the operating range of the sensor far less than $1N$ when considering a safety factor (≥ 3.00) as recommended in the medical industry. Their sensor provided a resolution of $4mN$. Tanimoto et al. reported a piezoresistive-based micro-force sensor for intravascular neurosurgery application [36]. The diameter of the force sensor was $1.6mm$ and had a length of $12mm$. However, this force sensor was capable of measuring load equivalent to only $29mN$ compared to $0.5N - 0.8N$ which is the preferred force range for soft tissue indentation procedures [30, 37, 38, 39, 40]. As such, the micro-force sensor proposed by Tanimoto et al. is not suitable for measurements to evaluate viscoelastic properties of soft tissue.

Yip et al. developed a fiber optic-based uniaxial micro-force sensor, to measure tissue interaction force during mitral valve annuloplasty [41]. The overall diameter of the sensor was $5.5mm$ and the length was measured to be $12mm$. The sensor was capable of measuring a normal force ranging up to $4N$ with a root mean squared error of $0.13N$. As suggested by Yip et al. the sensitivity of the sensor depends on the bending of the optical fiber. Moreover, attempting to measure reaction loads with a bend radius below a few centimeters would lead to erroneous measurements. Consequently, a drawback of the fiber optics-based sensor is prominent in reliably operating in confined spaces and areas that would demand for dexterous maneuverability. Research conducted

by Alekya et al. investigated a mesoscale diaphragm-based piezoresistive force sensor to characterize tracheal tissue viscoelastic properties [42]. The overall footprint dimensions of this sensor were $3.5 \times 3.5 \times 0.5$ (all dimensions in mm). The sensor was capable to capture normal load within the range of $0 - 250mN$ [42]. The range of the normal load of the sensor developed by Alekya et al. is 3.2 times smaller than the expected load from soft tissue indentation of $0.8N$ [30, 37, 38, 39, 40]. Table 1.1 presents a summary of various sensor devices investigated while performing the literature review. Table 1.1 also highlights the overall limitations of the individual sensor design as it applies to this work.

Although several researchers have attempted to construct a diagnostics device for tissue palpation, they have not been successful in achieving the necessary design specifications in terms of being able to access the organ through the natural orifice as well as recording tissue viscoelastic properties in vivo in situ [43, 44]. Currently the techniques for evaluating tissue viscoelasticity use elastography, but this method assumes the bladder's health holistically and fails to quantitatively identify localized properties [45]. As such, there is a need to develop a system capable of accessing confined space in the human body and interrogating the tissue surface under question. The proposed system must also be capable of functioning in a clinical setting as opposed to a surgical environment.

1.4 Tissue Viscoelastic Models

During stress relaxation response, biological tissues exhibit hysteresis, which is why they must be modeled as viscoelastic materials [46]. Under constant stress and strain, a viscoelastic material exhibit both viscous and elastic-like behavior. A linear viscoelastic model consists of a linear spring

and linear dashpot in a certain combination. Combining the linear spring and linear dashpot either in series or parallel would result in the two simplest viscoelastic models, which are commonly

Table 1.1: Summary of existing technologies with limitations

Researcher	Application	Sensing Principle	Sensor Specifications	Limitations
Puangmali et al. [33]	Laparoscopic intervention	Optical	Size: $\phi 5mm$ Axial operating range: $\pm 3N$ Resolution: $20mN$	<ul style="list-style-type: none"> • Large overall size • Non comfortable • Prone to bending loss
Lee et al. [34]	Tactile sense	Capacitive	Size: $22mm$ square Axial operating range: $10mN$ Resolution: -	<ul style="list-style-type: none"> • Large overall size • Non comfortable • Limited operating range
Polygerinos et al. [35]	Cardiac catheterizing	Optical	Size: $\phi 4mm$ Axial operating range $\ll 1N$ Resolution: $4mN$	<ul style="list-style-type: none"> • Large overall size • Limited operating range with no factor of safety
Tanimoto et al. [36]	Intravascular neurosurgery	Piezo resistive	Size: $\phi 1.6mm$ Axial operating range: $29mN$ Resolution: $< 0.5mN$	<ul style="list-style-type: none"> • Limited operating range
Yip et al. [41]	Mitral valve annuloplasty	Optical	Size: $\phi 5.5mm$ Axial operating range: $4N$ Resolution: $130mN$	<ul style="list-style-type: none"> • Large overall size • Limited force capability ($< 130mN$)
Alekya et al. [42]	Tracheal stiffness characterization	Piezo resistive	Size: $3.5mm$ square Axial Operating range: $250mN$ Resolution: -	<ul style="list-style-type: none"> • Limited operating range

Table 1.1: Summary of existing technologies with limitations

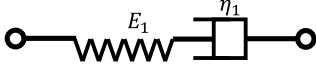
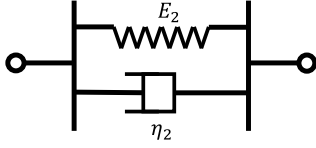
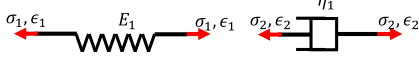
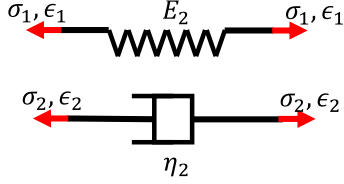
Researcher	Application	Sensing Principle	Sensor Specifications	Limitations
Li et al. [39]	Artrial fibrillation	FBG	Size: $\phi 4mm$ Axial Operating range: $0.8N$ Resolution: $2.7mN$	<ul style="list-style-type: none"> ● Large overall size ● Prone to bending loss
Tang et al. [43]	Minimally invasive surgical palpation	FBG	Size: $\phi 10mm$ Axial Operating range: $5N$ Resolution: $2.61mN$	<ul style="list-style-type: none"> ● Large overall size ● Prone to bending loss

recognized as Maxwell and Kelvin-Voigt models respectively.

Figure 1.2 represents Maxwell and Kelvin-Voigt models. The governing differential equations as derived in Fung for both the models are represented as well [47]. Creep compliance is the behavior of the model by holding the stress constant and investigating the strain response as a function of time. Strain-time response during creep compliance shows a sudden rise by a factor of σ_0/E at the beginning of the constant stress, after which the strain increase linearly with a rate of σ_0/η for the Maxwell model. An initial elastic response could be achieved for the Maxwell model however, time dependent strain is not recoverable and can increase constantly. Strain-time response during creep compliance behavior exponentially increases and settles down to a constant strain for the Kelvin-Voigt model. Kelvin-Voigt model on the other hand does not model an initial elastic response but yields a bounded time dependent strain that is also recoverable.

Stress relaxation is the behavior of the viscoelastic model by applying a constant strain and studying the stress response as a function of time. An exponential decay is expected for the stress-time graph during stress relaxation for the Maxwell model. Kelvin-Voigt model on the other hand does not demonstrates a stress relaxation behavior.

Table 1.2: Viscoelastic models with mathematical representation along with their governing equation, creep compliance and relaxation modulus [47]

	Maxwell model	Kelvin-Voigt model
Model representation		
Free body diagram		
Constraints	$\sigma = \sigma_1 = \sigma_2$ $\epsilon = \epsilon_1 + \epsilon_2$	$\sigma = \sigma_1 + \sigma_2$ $\epsilon = \epsilon_1 = \epsilon_2$
Governing equation	$\eta_1 \dot{\epsilon} = \sigma + \left(\frac{\eta_1}{E_1} \right) \dot{\sigma}$	$\sigma = E_2 \epsilon + \eta_2 \dot{\epsilon}$
Creep compliance	$J(t) = \frac{\epsilon(t)}{\sigma_0}$ $= \left(\frac{1}{\eta_1} t + \frac{1}{E_1} \right)$	$J(t) = \frac{\epsilon(t)}{\sigma_0}$ $= \frac{1}{E_2} \left(1 - \exp \left(-\frac{E_2}{\eta_2} t \right) \right)$
Relaxation modulus	$E_r(t) = \frac{\sigma(t)}{\epsilon_0}$ $= E_1 \left(\exp \left(-\frac{E_1}{\eta_1} t \right) \right)$	$E_r(t) = \frac{\sigma(t)}{\epsilon_0} = N/A$

Limitations abound when implementing the Maxwell model which lacks to characterize the strain creep behavior and the Kelvin-Voigt model which is incapable of describing stress relaxation behavior during soft tissue characterization. A study conducted by Wang et al. reported a comparative modeling study to achieve a balance between the simplicity of mathematical modeling and the accuracy of the experimental fit when modeling viscoelastic materials [48]. They specifically discuss the Maxwell, Kelvin-Voigt, and Standard Linear Solid models (SLS). It was reported that the SLS model, maintains a good balance between mathematical simplicity and model generality, and is the most widely used model in the field of biomechanical modeling of soft tis-

sues. Following that, in this research, a three-element standard linear solid model (three element Maxwell-Wiechert) will be used to evaluate and characterize the viscoelastic properties of the measured tissue response. There will be an extensive discussion about this model in section 4.2.

1.5 Significance and Contribution of Research

The significance of this research lies in its potential to make a substantial contribution in obtaining tissue relaxation responses due to controlled indentation in confined spaces in the human body. Current technology presents a gap to measure localized tissue relaxation forces in vivo. This issue has been source of concern for medical practitioners. This research endeavors to address several critical challenges as they relate to providing information to characterize and evaluate the performance of a custom design micro-force sensor for obtaining force relaxation data to evaluate localized tissue viscoelasticity. Measuring such force relaxation response as a time history could provide useful information to evaluate changes in the tissue viscoelasticity as a function of elapsed time. These changes could be an indicator of tissue disease or disease progression. Subsequently the results obtained through this research will aid to advance our understanding to characterize viscoelastic properties of soft tissue in vivo due to indentation methodology by proposing the following:

1. A sensing system design methodology to satisfy the desired design specifications by following an exhaustive search algorithm while considering factors like design for manufacturing and available resources.
2. A design of an uniaxial micro-force sensor intended to palpate interior bladder wall tissue for localized characterization of the viscoelastic properties aiming to significantly improving

the quality of medical diagnostic intervention.

3. A methodology for the fabrication, assembly, characterization and evaluating the performance of the micro-force sensor, followed by necessary design modification strategy.
4. A methodology to collect the force relaxation response of soft tissue using the micro-force sensor and characterizing the viscoelastic response using a standard linear solid model.

The significance of this research is grounded in its potential to drive progress and innovation, address existing challenges.

1.6 Dissertation Overview

The dissertation is organized in the following manner. Chapter 1 presents and introduces the topic. It discusses the need for a diagnostic system that would measure localized tissue relaxation forces in vivo and in confined spaces in the human anatomy. Furthermore, motivation and current technologies are presented demonstrating a gap in existing technologies. An introduction to commonly used viscoelastic models are presented as well. In chapter 2 design specification matrix is generated for intended application to palpate interior wall of human bladder. A sensing system methodology is developed, with initial design concepts. Design optimization problem is formulated and exhaustive search algorithm using finite element (FE) analysis is generated to evaluate optimal design for the sensing element. Manufacturing methods employed to fabricate a functional prototype of the micro-force sensor is presented. Chapter 3 presents a setup developed to characterize the micro-force sensor. Performance characterization of the micro-force sensor as it relates to resolution, sensitivity, accuracy, precision, repeatability, and hysteresis will be discussed. A summary

of the desired and characterized sensor performance matrix will be presented. Chapter 4 of this dissertation will focus on the development of a tissue characterization test bed. Tissue characterization experiments will be conducted on the forearm of 30+ human subject participants, by following the guideline through an approved Institutional Review Board protocol (IRB protocol number: 2023 – 0306). Effects of process parameters like the indentation depth and strain rate will be explored. Effects of age, race, gender, and arm strength exercise will be investigated. Finally the dissertation will conclude with chapter 5 which discusses the importance of this research as a component of a diagnostic system for in vivo characterization of soft tissue and presents with key conclusions and future research direction.

CHAPTER 2

MICRO-FORCE SENSOR DESIGN AND FABRICATION

2.1 Introduction to Sensor Design Methodology

Manipulators composed of rigid links face constraints when it comes to effectively reaching the entirety of the interior bladder wall for contact palpation. To address this limitation, a compliant manipulator with 6 degrees of freedom (DOF) distributed across 10 joints was proposed [49]. This compliant design aims to extend the reach of the manipulator, with a desired position and orientation specifically targeting the ‘difficult-to-reach’ areas within the bladder, including the trigone. Adejokun et al. presented a compliant robotic manipulator for conducting localized contact palpation at the interior bladder wall tissue accessed through the urethra with an overall diameter of $4mm$ [50, 49, 51].

The sensor presented in this research is envisioned to be attached at the tip of the compliant manipulator proposed by Adejokun et al. [51]. The combined system, consisting of the manipulator and the attached sensor, has the potential to access the bladder and perform localized palpation and investigation of any area of the bladder interior wall. This can be accomplished by ensuring an appropriate load capacity and provide the ability to record the tissue response due to applied forces and use the information to evaluate tissue relaxation characteristics. The micro-force sensor proposed in this research could be employed for diagnostic applications such as transurethral palpation or palpation during minimally invasive surgical interventions [52, 39, 33, 53, 41]. An objective of this research is to contribute towards the development of a micro-force sensor. This

chapter is structured to present the characteristics of generalized force sensor design methodology, followed by the development of the desired design specification matrix. A conceptual design of the micro-force sensor and its working principle is presented along with preliminary analysis which will be used for prototyping and characterization. An investigation is performed to select optimal design parameters that will improve the sensitivity of the sensor while safely withstand the desired loading condition. The design optimization formulation is presented and a parametric discrete variables FE-based approach is utilized to obtain the cost of the objective function for the feasible designs which were used as a guidance for optimal design selection. Fabrication methodologies and the challenges to overcome are discussed.

2.1.1 Force Sensor Characteristics

The intended application of the micro-force sensor is to palpate the internal organ tissue, as such it should be capable of measuring reaction force. Mechanical inputs like weight, compression, pressure could be transformed as an output electrical signal, and the values of this electrical signal could be calibrated to obtain the equivalent value of the experienced force. The desired parameters of the sensing system could be identified by establishing the intended application and enumerating the required operational characteristics and are presented in figure 2.1.

These characteristics can be classified into five subcategories, performance specifications, intended application space, operating environment condition, expected loading scheme, and sensing principle. The conceptual design development of the micro-force sensor must emerge by considering at least one parameter from every category. The performance matrix of the sensor must be evaluated as it relates to the overall dimensions, load bearing capacity, sensitivity, accuracy, res-



Figure 2.1: Characteristics to be considered for the development of a force sensor for medical diagnostics purposes

olution, precision, repeatability, and hysteresis. Moreover, the desired performance specification matrix will provide guidelines for the development and identification of the data acquisition system. The intended application of the sensor is used to define information as it relates to the size of the sensor and the necessary precautions that must be taken to conduct the measurements safely. For instance, if the target tissue is inside the human body, it is imperative to consider the access point and the dimensions of the device to reach the desired organ within the human body. Investigating the operating environment of the sensor can be used to define the encapsulation needed to protect the electro-mechanical subsystem in the sensor from its surrounding. For instance, if the sensor is envisioned to be operated inside of a human body, the sensor must be encapsulated with a bio-compatible protective sheath that will prevent the interaction of the bodily fluids with the force sensor components. In this research, the conceptual design of the micro-force sensor will consider the intended application for in vivo testing in a moist/bodily fluid environment. The structural design of the force sensor must consider the expected loading scheme the sensor will experience. For instance, if the intended use of the sensor is to investigate the tissue interaction forces while performing minimally invasive surgery, designing a force sensor that will be able to sense multiaxial loads will be beneficial [54, 55]. The sensor developed through this research is intended to interrogate the tissue to characterize its viscoelastic properties through normal-to-surface indentation or palpation; as such a uniaxial loading scheme will suffice this need. Selection of the sensing principle will assist in designing the deformable structure as well as defining operational and geometric constraints for the sensor development. The sensing principle will drive the selection and requirement for additional instrumentation needed to capture the data from the sensor. The micro-force sensor is proposed to measure uniaxial loads using a metal foil strain gauge. Further discussion on the conceptual design of the sensor is provided in section 2.3.

2.1.2 Design Methodology

The micro-force sensor must meet the desired specifications based on its intended application. As discussed in Chapter 1, a part of this dissertation was to develop a sensing system that could collect the internal organ in vivo tissue relaxation forces when palpated. As discussed in the motivation section 1.2, the human bladder is the target organ for using this sensor. As such, the design specifications as they relate to the overall dimensions, expected force range, desired accuracy and resolution to effectively characterize the viscoelastic properties of the soft tissue are operational characteristics to be defined.

Design and development of a reliable and accurate force sensor is contingent upon a well structured design methodology, which will not only guide the design process but also ensure that the resulting device meets the desired specifications and performance criteria. This section describes key strategies, materials and methods considered and investigated in the pursuit of engineering a micro-force sensor intended to address unique challenges as they relate to measuring tissue reaction forces in vivo in confined spaces. This methodology starts by performing a literature review to identify if there are any existing sensing systems that meets the desired specifications. If none of the existing sensors meet the desired specifications, then the procedure, as presented in figure 2.2, is followed to develop a novel sensing system.

In this methodology, initial steps encompass the identification of a need and its subsequent translation into desired design specifications. These specifications are then used to establish essential sensor characteristics and the desired performance matrix. Followed by performing a literature review to collect prospective sensing systems aligned with the identified need. If a suitable sensing system is identified, it is implemented for the in vivo viscoelastic characterization of soft tissue.

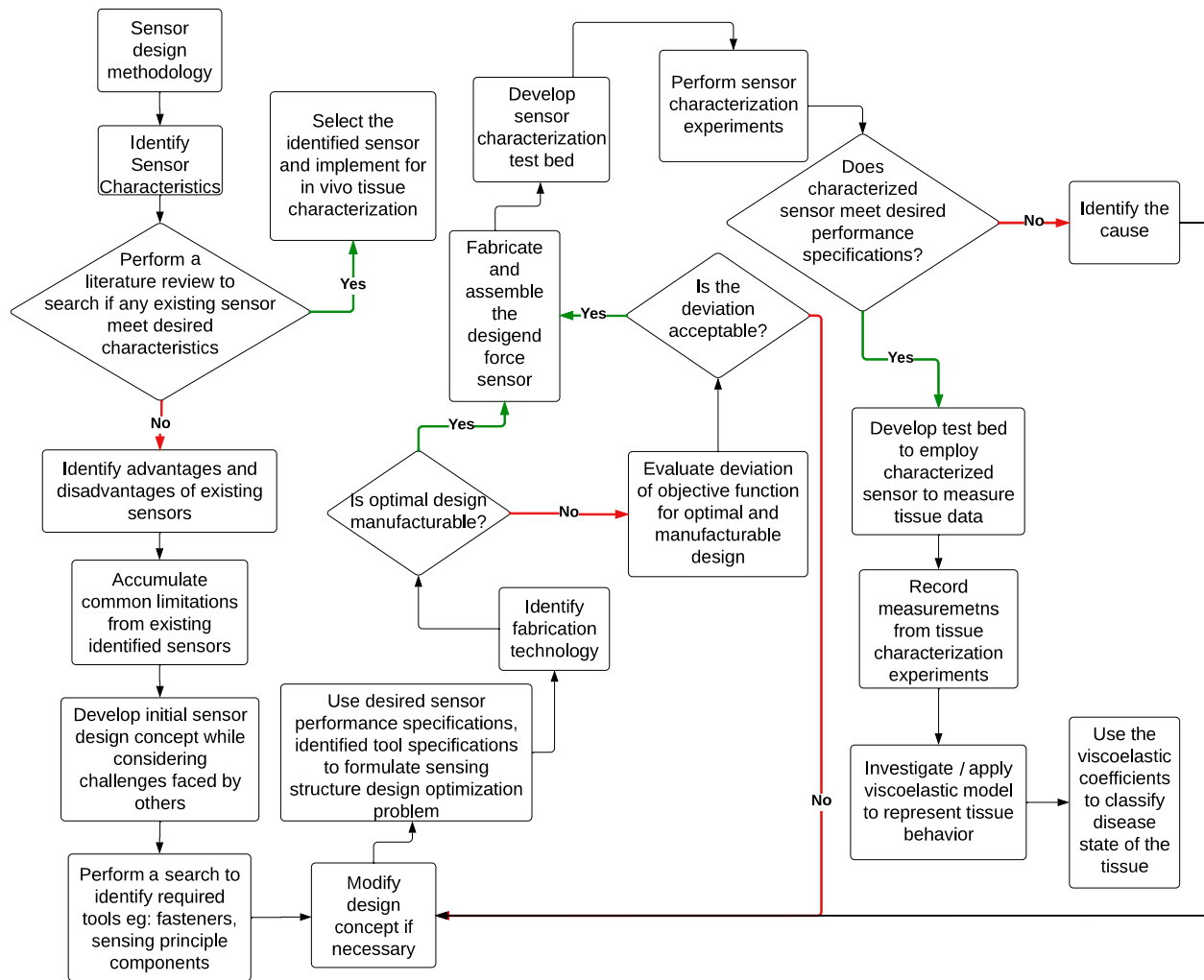


Figure 2.2: Sensing system methodology for biomedical applications

On the other hand, if non of the existing sensing systems are suitable for intended application an overview of potential limitations inherent in existing systems are identified. This list of limitations serve as a foundational guide for developing a sensing system for the intended application. Subsequent to this, a conceptual design of the sensing system is generated followed by performing a review of available resources and the required technology necessary for the development of the desired concept. This encompasses availability of sensing principle (fiber optics, strain gauge etc.), raw materials, manufacturing resources, and capability of developing necessary fixtures. The identification of this information is important and it will be considered during the iterative design

process.

After developing an initial conceptual design of the sensor based upon the limitations identified in the previous stage of the design methodology, the dominating design parameters of the sensor concept are identified. Parameters (material, geometric) that are anticipated to enhance the sensitivity as well as the load bearing capacity of the sensor are referred as dominant design parameters. Constraints on these dominant design parameters are identified as they relates to geometric and material properties and analysis is performed to evaluate the sensitivity as well as load bearing capacity. Thereupon, initial concept is iterated and modified for further analysis. The dominant parameters of the design as well as spatial and material constraints are defined for the modified concept. Subsequently, a design optimization problem is formulated and analyzed to define optimal geometric parameters of the design. Available manufacturing processes for prototyping the optimal design is evaluated. Investigation is performed if the optimal design is manufacturable. If the optimal design cannot be prototyped using available technology and resources, the optimal design parameters are modified considering the available resources and the deviation in the cost of the objective function is evaluated. If the cost of the objective function obtained through modified (manufacturable) design parameters lack to meet desired performance specifications then the concept or available resources like the manufacturing methods, raw material must be modified until design with acceptable deviation is obtained.

The next phase of the sensing system methodology describes the prototyping and assembly of the micro-force sensor. Subsequently, the performance characteristics of the prototyped device is evaluated. A checkpoint is added to evaluate if all the desired performance specifications of the prototyped micro-force sensor are met. The final phase of the methodology discusses use of the characterized micro-force sensor in measuring and characterizing tissue relaxation forces.

Followed by developing experiments to recorded tissue response data due to controlled indentation, to characterize and obtain equivalent viscoelastic coefficients.

2.2 Desired Design Specifications

The desired sensor performance specifications could be obtained using a literature survey or from a subject matter expert. The desired specifications will be used to identify the optimal values for the critical parameters of the sensor. The micro-force sensor reported in this research must consider the size as it relates to the ease of access to the designated confined space site, the range of normal force to be applied at the tip of the sensor, the minimum required resolution, and the operational environment conditions.

A literature review was conducted to determine the dimensional constraints of the sensor sub-system for the intended confined space location which is the inside wall of the human bladder. The dimensions of diagnostic devices need to be defined considering reported anatomical measurements. The average diameter with a maximum stretch of the external urethral meatus was reported to be within the range of 6.00 to 10.33mm [56, 57, 58]. The outside diameter of a commonly used flexible endoscope is between 5.00 to 8.3mm [59]. Hudson et al. performed a study involving 115 patients (60 male and 55 female) to examine the impact of Flexible Ureteroscope (FU) diameter on the ease of passage [59]. The researchers found that when they decreased the diameter of the FU from 9.0 to 7.4Fr (3.00 to 2.47mm), there was a significant decrease (dropping from 37% to just 0.9%) in the percentage of failed attempts to insert the instrument. Miernik et al., reported on a study conducted on 153 patients (114 male and 39 female) to investigate the occurrence of urethral wall injuries in association with the size of the instruments used during ureteroscopy

[60]. The results revealed that using instruments of varying diameter from 14.0 to 16.0Fr (4.67 to 5.33mm), superficial lesions on the walls of the urethra were observed in approximately 39.9% of the patients, deeper lesions were present in approximately 17.6%, and circumferential perforation was found in approximately 47.7% of the individuals. Furthermore, according to Lildal et al., a study involving 180 patients (110 male and 70 female) indicated that the incidence of lesions and complications associated with post-ureteroscopic surgery decreased significantly when smaller diameter ureteroscopy instruments were used, specifically those ranging from 10.0 to 12.0Fr (3.33 to 4.00mm) in size [61]. These findings strongly support the notion that using reduced-diameter transurethral instruments are directly correlated with minimizing and reducing patient trauma.

The organs proximal to the pelvic region undergo substantial deformations within the range of 5mm to 8mm due to small applied forces (0.5N to 0.8N) [30, 37, 38, 39, 40]. To achieve a conservative sensor design, it was postulated that the sensor should be able to sustain an equivalent load of 1N with a factor of safety acceptable within the medical device industry.

Table 2.1: Micro-force sensor design specifications

Characteristic	Specification
Diameter	$\leq 3.5mm$ (sensor housing)
Force Range	$\leq 1.0N$ (normal force)
Resolution	20mN
Accuracy	$\pm 30mN$
Safety Factor	≥ 3.5
Operating Environment	Wet/Moist
Other	Biocompatibility

A finer resolution will make it possible to capture tissue reaction response due to smaller applied forces. The micro-force sensor designed by Li et al. and Gao et al. for in vivo tissue characterization with a resolution of 23mN was adequate to capture tissue relaxation forces and then characterize the tissue viscoelastic properties [62, 63]. The desired specifications for the micro-

force sensor considering the work by Kumat & Shiakolas [40], Li et al.[62] and Deng et al. [55] are presented in table 2.1.

2.3 Conceptual Design

The uniaxial micro-force sensor consists of three major components; sensor head, sensor base and a sensing element. The sensor base component is intended to be attached at the tip of the compliant manipulator discussed in section 2.1. The sensor head will interact with the host tissue as the manipulator palpates and transfers the load to the sensing element/beam which will aid to sense/measuring the reaction forces. The sensing element will function as a strain-measuring structure.

As discussed in chapter 1, existing sensing technology has been analyzed and each of these technologies have drawbacks as it applies to interrogating the confined space environment in the human bladder. Investigating the benefits and drawbacks of fiber optics [55, 35, 64], piezo-resistive [54, 65] and capacitive [34] based strain measurement technologies it was identified that these sensing technologies could not be used because they do not meet at least one of the desirable specifications, relating to either size, accessibility to confined space environment and/or accessibility in the sensing structure itself. For example, dexterous manipulations are necessary to access and orient the manipulator in a confined space environment. Fiber optic-based sensing technology cannot operate reliably in confined spaces requiring a small bending radius with large bend angles which causes chirping losses and poor repeatability of measurements [66]. Yip et al. concluded that the sensitivity of their sensor and the bending of the optical fiber were directly correlated and attempting to measure reaction loads with a bend radius less than a few centimeters lead to erro-

neous measurements [41]. In addition to performance limitations due to bend radius constraints, Kumar et al. called attention to the requirement of an amplification mechanism to improve the sensitivity, and challenges in implementing, routing, and moving the optical fiber through confined spaces in the human body [67]. Piezo-resistive sensors by Wang et al. and Hu et al. have large overall sensor dimensions ($4 \times 4mm^2$ and $9 \times 9mm^2$) and operational range limitations ($1mN$ and $30mN$) [54, 65]. Strain gauge based sensing technology has been in use for many decades and they are reliable strain measuring devices. A survey was conducted to identify “miniature” metal foil strain gauges. A miniature strain gauge must meet the desired spatial and operation constraints. It is desirable to consider positioning of the strain gauge in a location where the change in strain remains within its linear operating range.

Since the overall diameter of the sensor is desired to be $\leq 3.5mm$, the size of the bounding box (refer figure 2.3b) of the sensor base; a feature which will encompass the sensing element is defined to be $2.7mm \times 1.55mm \times 5mm$ (length \times width \times height). Further increasing the length and/or width of the bounding box will require increasing the overall diameter of the micro-force sensor housing. As such the desired dimensions of the strain gauge must be less than the bounding box dimensions of $2.7mm \times 1.55mm \times 5mm$ (length \times width \times height) of the sensor housing.

A miniature metal foil strain gauge with planar dimensions $1.9mm \times 1.4mm$ (*N2K – 06 – S5024G – 50C/DG/E5*, MicroMeasurements Inc., Wendell, North Carolina, US) was identified to meet the dimensional constraints. Its schematic is presented in figure 2.3a [68]. The characteristic dimensions of the strain gauge provided by the manufacturer are shown in figure 2.3a where $d_1 = 1.99mm$ is the total length of the gauge packing, $d_2 = 0.48mm$ is the gauge active length, $d_3 = 0.66mm$ is the distance of the center of the active length of the gauge from the top, and $d_4 = 1.4mm$ is the total width of the gauge packing. The linear operating range of the identified

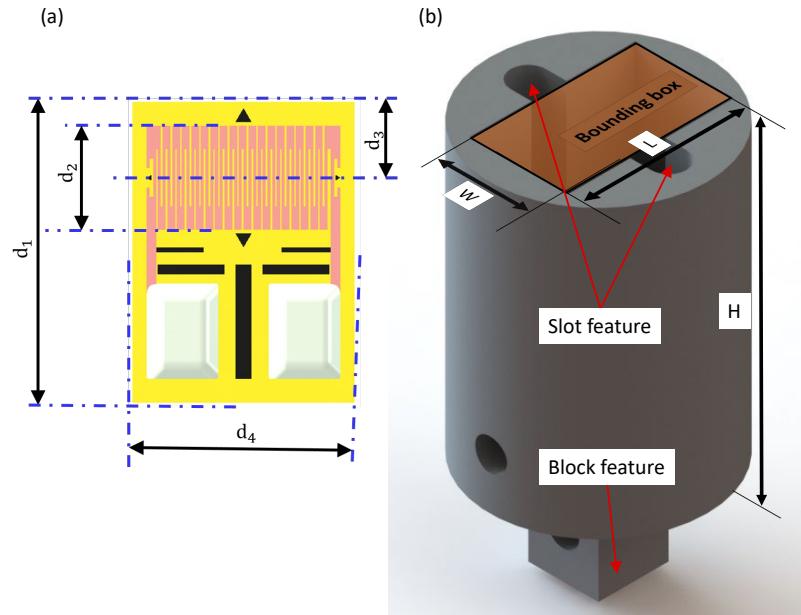


Figure 2.3: Schematic models of (a) metal foil strain gauge with total dimensions and active grid dimensions (b) sensor base component with a bounding box feature provided to encapsulate sensing element, slot feature as a guide-way, and block feature for its assembly with a micro-robot

strain gauge is $\pm 3000\mu\epsilon$. The identified strain gauge met the desired dimensional constraints but further investigation must be performed to analyze if it met the desired operational performance requirements.

The sensing element serves as the mounting structure for a miniature metal foil strain gauge that will be used to measure the strain experienced by the sensing element during operation. Consequently, the strain experienced by the sensing element must be analyzed. The dimensions and linear operating range of the strain gauge impose additional constraints to the geometric parameters of the sensing element. Simplest structures acting as a sensing element can either be a cantilever beam or a column. One of the factors governing the design of geometric parameters of the sensing structure was the length of the strain gauge backing. Designing for the strain gauge attached cantilever beam imposed challenges to encompass the sensing structure inside the sensor housing. As such initial analysis for a column experiencing compressive load was performed to evaluate

the strain due to applied load. Considering the overall dimension of the strain gauge the sensing element/column must be at least $1.99mm \times 1.4mm$. However, the sensing element will need to have features enabling it to attach to the sensor base component. Accordingly, an additional $2mm$ height will be needed to account for the mounting hole feature on the sensing element.

A column can be classified into two categories; either as an intermediate-short column or a long column, according to its slenderness ratio (SR) [69]. Although commonly utilized materials for in vivo diagnostic interventions in medical care include stainless steel (grade 316L) and titanium alloy (Ti6Al4V), in this research, aluminum (6061-T6) is also considered and analyzed as a candidate material for the sensing element since the sensor unit will be covered with a biocompatible sheath [70]. The sheath will also protect the device in the operating environment, prevent contamination. Aluminum is easily available and easy to work with and as such it can be used to develop prototype after identifying the concept as well as the optimal geometric parameters of the design concept. Moreover, the Young's modulus of aluminum is the lowest compared to stainless steel (grade 316L) and titanium alloy (Ti6Al4V), and the strain to be experienced is inversely proportional to the Young's modulus of the material. An added benefit of selecting aluminum is an improvement to the sensor sensitivity. As such, for an aluminum alloy, the column is classified as an intermediate-short column if $SR \leq 66$ or else it is classified as long one [69]. Accordingly, the thickness, t , of a column can be evaluated for a given slenderness ratio, SR , and effective column height, H_{eff} , by rearranging equation 2.1. Maximum stress experienced by a column structure prior to permanent deformation is called as allowable stress. The allowable stress for aluminum intermediate-short and long columns can be evaluated using equations 2.2 and 2.3 respectively where, the Young's Modulus is E , allowable stress is σ_{all} , slenderness ratio is SR , and the factor of safety is N_f [69]. The factor of safety in this research is defined to be 3.5 for all design considerations (similar to

research by [55]).

$$SR = \frac{H_{eff}}{\sqrt{\frac{t^2}{12}}} \quad (2.1)$$

$$\sigma_{all} = \frac{230 - 0.868 * SR}{N_f} \quad SR \leq 66 \quad (2.2)$$

$$\sigma_{all} = \frac{\pi^2 E}{N_f * SR^2} \quad SR > 66 \quad (2.3)$$

Considering the dimensions of the miniature strain gauge, the minimum height of the sensing element must be $H = 1.99mm$. The effective height of the fixed-free condition column will be twice the minimum height ($H_{eff} = 2H = 3.98mm$) [71]. The corresponding thickness for a slenderness ratio $SR = 66$ is evaluated to be $t = 0.209mm$ according to equation 2.1. If the thickness $t \geq 0.209mm$, then the column will be classified as a short-intermediate column whereas if $t < 0.209mm$, the column will be classified as a long column. The allowable stresses that the sensing element could undergo for off-the-shelf thicknesses of $0.25mm$ and $0.15mm$ (aluminum columns with $E = 70$ GPa) were evaluated using equations 2.2 and 2.3 and found to be $52.04MPa$ and $23.36MPa$ respectively.

The evaluated allowable stress can be used to analyze the force according to $F = \sigma_{all} \cdot A$, where σ_{all} is the allowable stress, $A = t \cdot w$ is the cross-sectional area and investigate if the column structure will be capable of withstanding the expected desired load of $1.0N$ (along the height of the column). Subsequently, a short column with design dimensions of height $H = 1.99mm$, thickness $t = 0.25mm$, and width $w = 1.5mm$ (based on the overall width of the miniature strain gauge of $1.4mm$) can withstand an axial load up to $19.5N$. A long column with design dimensions of height $H = 1.99mm$, thickness $t = 0.15mm$, and width $w = 1.5mm$ can withstand an axial load along the height of the column up to $5.2N$. Consequently, both short and long columns could

withstand the expected desired load of $1.0N$. The next step in the design process is to identify if the short/long columns will generate measurable strains when the desired maximum load of $1.0N$ will be applied.

When an axial load of $1.0N$ is applied on the short column, equivalent stress and strain of $2.67MPa$ and $38.10\mu\epsilon$ are experienced near the fixed support of the column structure. When an axial load of $1.0N$ is applied on an aluminum long column it will result in equivalent stress and strain of $4.44MPa$ and $63.49\mu\epsilon$. These strains fall within the linear operating range of the identified metal foil strain gauge of $\pm 3000\mu\epsilon$. However, to sense a desired change in load of $\Delta F = 20mN$ (refer table 2.1), an equivalent change in strain of $\Delta\gamma = 1.27\mu\epsilon$ is evaluated according to equation 2.4, which yields an equivalent change in resistance of $\Delta R = 0.010\Omega$ according to equation 2.5 where A is the cross section area of the column, E is the Young's Modulus, $k = 2.03$ is the gauge factor provided by the manufacturer, and $R_{sg} = 4956.58\Omega$ is the nominal strain gauge resistance.

$$\Delta\gamma = \frac{\Delta F}{A \cdot E} \quad (2.4)$$

$$\Delta R = \Delta\gamma \cdot k \cdot R_{sg} \quad (2.5)$$

Data acquisition devices (DAQ), are employed to acquire signals from analog sensors (strain gauge) into a computer system for further processing. The resolution of DAQ devices is based on the number of bits used for discretizing the analog sensor signal. A 16-bit and 24-bit data acquisition devices are capable of sensing a change in resistance of 0.305Ω and 0.001Ω respectively, with a $10K\Omega$ range (further discussion about the range is provided in section 3.2.1). Therefore, a 16-bit data acquisition device will not be capable of measuring a desired change in load of $20mN$. Although a 24-bit data acquisition device will be capable of sensing a desired change in load of

$20mN$, positioning the central axis of the active length of the strain gauge at the desired location was not suitable due to spatial constraints. Further reducing the thickness or increasing the height will increase the sensitivity but will also cause the sensing element to fail due to buckling loads. As such, it was necessary to modify the conceptual design of the sensing element to employ eccentric load in order to increase the sensitivity while maintaining the structural integrity and devising necessary modifications for strain gauge attachment.

The modified conceptual design of the sensing element is presented in figure 2.4a. A schematic of the sensing element and its interaction with the sensor head, along with the important dimensional parameters are presented in figure 2.4b. The hemispherical surface of the sensor head will interact with the tissue¹, whereas the bottom surface of the hemisphere will transfer the load to the sensing element at location D (please refer to figure 2.4b). The sensing element, which is rigidly attached at site A (please refer to figure 2.4b), will experience strain due to the load transmitted from the sensor head. Consequently, the sensing element must be designed to meet the desired design specifications while taking into consideration the dimensions, linear operating range of the strain gauge to be mounted on the sensing element as well as the geometric constraints due to the desired size of the sensor housing. The sensing element must have certain characteristics such as, the geometric features to enable mounting of the strain gauge, the capacity to sustain an applied load without undergoing plastic deformation (remaining in the elastic region), and sensitivity to be able to sense a minimum desired change in load of $20mN$. The design parameters of the sensing element must be defined and analyzed to maximize the absolute strain at the desired strain gauge attachment location to improve the sensitivity of the sensor.

¹The sensor head is not intended to directly interact with the tissue, instead a biocompatible sheath will cover the sensor during operation. However, for ease of illustration and discussion purposes, the biocompatible covering is not shown in figure 2.4

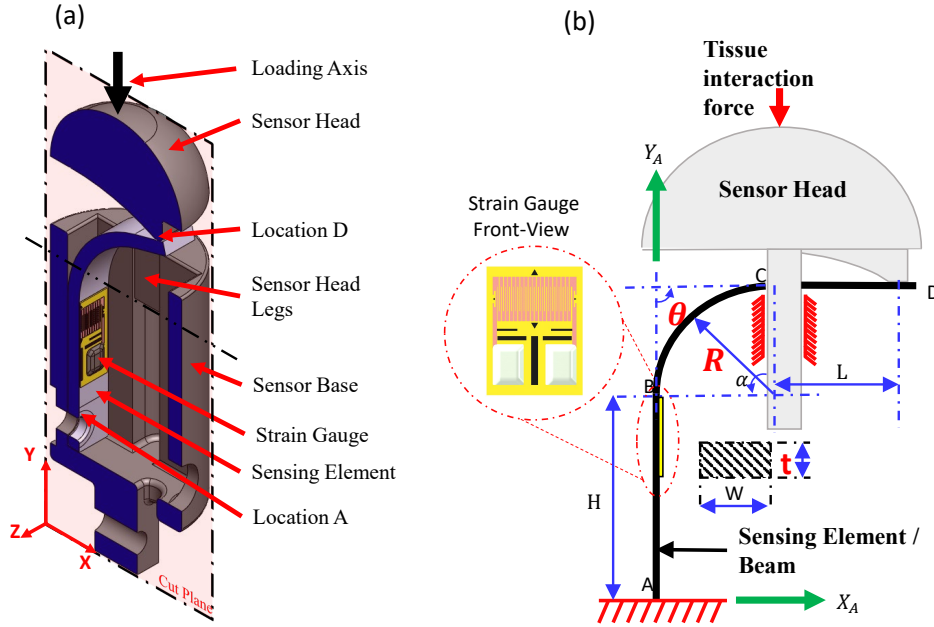


Figure 2.4: Solid model of the developed sensor design concept #1, (a) Section view of the micro-force sensor subsystem, (b) Schematic of the micro-force sensor with key design parameters as bend radius R , bend angle θ , and thickness t , as well as an inset with tentative strain gauge attachment location

2.4 Design Optimization

The primary design parameters of the sensing element are bend radius R , bend angle relative to the vertical beam member θ , and beam thickness t as shown in figure 2.4b. These parameters will be varied and the corresponding stress and strain will be evaluated. It is important to note that the sensitivity of the sensor is directly related to the strain and as such maximizing the strain will improve its sensitivity.

The cost of the objective function will be to maximize the absolute value of the strain sensed at the desired location of the sensing element. The optimization problem is formulated and presented in equation 2.6, where $\gamma_b(R, \theta, t)$ is the normal (Y-axis) strain evaluated at the desired location, γ_{sg} is the linear operating limit of the strain gauge, σ_{max} is the maximum stress experienced by the sensing element, $N_f = 3.5$ is the factor of safety, and S_y is the yield strength of the sensing

element material.

$$\begin{aligned}
 & \text{Max: } |\gamma_b(R, \theta, t)| \quad [\mu\epsilon] \\
 & \text{Such that: } \left\{ \begin{array}{l} \sigma_{max} \times N_f \leq S_y \quad [MPa] \\ R(1 + \cos(\theta)) + L\sin(\theta) + \frac{t}{2} \leq 2.5 \quad [mm] \\ H + R\sin(\theta) - L\cos(\theta) \leq 6.5 \quad [mm] \\ \gamma_{sg} - |\gamma_b(R, \theta, t)| \geq 0 \quad [\mu\epsilon] \end{array} \right. \quad (2.6) \\
 & \text{Limits: } \left\{ \begin{array}{l} 0.2 \leq t \leq 0.35 \quad [mm] \\ 0.2 \leq R \leq 3.7 \quad [mm] \\ 90 \leq \theta \leq 130 \quad [deg] \end{array} \right.
 \end{aligned}$$

The characteristics dimensions of the identified strain gauge are used to define the candidate attachment location for its central axis at $0.48mm$ from B towards A (figure 2.4). The optimization formulation includes inequality constraints for the allowable stress while geometric constraints are imposed on the overall dimensions of the sensing element. An inequality constraint is added to ensure that the estimated strain on the sensing element (γ_b) does not exceed the operating limit of the strain gauge (γ_{sg}). The upper and lower bounds of the design parameters are defined considering different criteria including geometric limitations, machinability, manufacturability, ease of assembly, improved sensitivity, and off-the-shelf component availability.

The interface between the sensor head and the sensing element exhibits a sliding motion. The interface distance, L, along the moment arm changes dynamically depending on the magnitude of the applied force. This causes the behavior of the bent member (part of the sensing element) to be a nonlinear function of the displacement applied at the tip of the sensor head. When the top of the

sensor head is displaced, it causes an equivalent reaction force at the interaction location D. The nonlinear behavior between the applied displacement on the sensor head and the sensing element is analyzed using FE analysis techniques. The optimization of the defined design parameters is performed using an exhaustive search approach over all discretized sets for each design parameter. A design point is defined as a unique combination of discrete values of bend radius, bend angle, and thickness of the sensing element.

The thickness $t \in [0.20, 0.35]mm$ is defined in increments of $0.05mm$ for 4 values. The minimum thickness of the sensing element was evaluated as a function of critical load P_{cr} , safety factor N_f , effective height H_{eff} , Young's modulus E , and width W of the sensing element according to Euler's formulation for slender columns under buckling as presented in equation 2.7 [71].

$$t = \sqrt[3]{\frac{12N_f P_{cr} H_{eff}^2}{\pi^2 E W}} \quad (2.7)$$

The height of the sensing element was set as a constant at $H = 1.99mm$ (see discussion in section 2.3) which yields an effective height $H_{eff} = 2H = 3.98mm$ [71]. The width W was set to a constant value of $1.5mm$ since the overall width of the strain gauge was specified as $1.4mm$. A safety factor $N_f = 3.5$ was desired for the maximum load ($P_{cr} = 1N$) that the sensing element will experience. The Young's modulus for the aluminum sheet was found to be $70GPa$ from the material data specification sheet [71]. The limit for the thickness to prevent buckling was evaluated to be $0.09mm$ by substituting the respective values of the parameters in equation 2.7. As such an off-the-shelf aluminum sheet with thickness $0.1mm$ was evaluated for further investigation. However since the design concept considers a curved member, the height of the sensing element will be $> 1.99mm$ (depending upon the angle of curvature) therefore thickness should also be greater than $0.1mm$. The lower and upper limits of thickness were chosen to be $0.2mm$ and

0.35mm respectively with the option to expand the range depending on the optimization analysis results.

The bend radius $R \in [0.2, 3.7]mm$ is defined in increments of 0.5mm for 8 values. The minimum bend radius R for an aluminum sheet can be obtained by using its thickness t , and the tensile reduction area A_{tr} according to equation 2.8 [72].

$$R = t \left(\frac{50}{A_{tr}} - 1 \right) \quad (2.8)$$

For an established minimum thickness of 0.2mm and considering the tensile reduction area of aluminum to be 26% (according to material data specification [73]), the minimum bend radius obtained is 0.18mm. Crack formation was observed when a 0.3mm thick aluminum sheet was bent with a bend radius of 0.1mm as shown in figure 2.5. However, no crack formation was observed when a 0.3mm thick aluminum sheet was bent with a radius of 0.2mm. The upper limit of the bend radius was set to 3.5mm considering the horizontal spatial constraint of 2.5mm in equation 2.6.

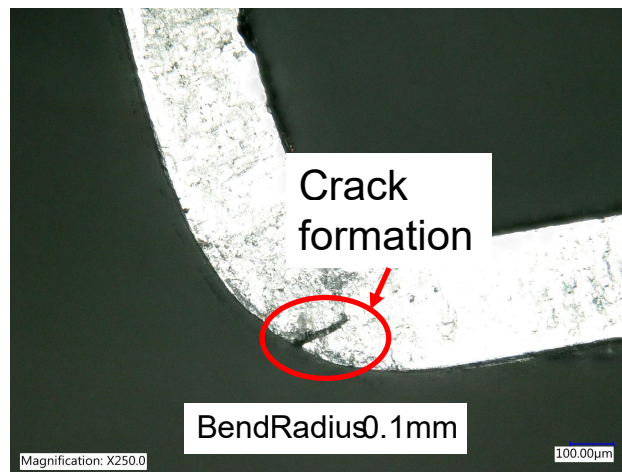


Figure 2.5: Aluminum sheet with thickness 0.3mm bent at a 90° angle with a bend radius 0.1mm developed a crack on the outer surface

The bend angle $\theta \in [90^\circ, 130^\circ]$ is defined in increments of 10° for 5 values. Setting a bend

angle lower than 90° will create an obstruction for the displacement of the sensor head during loading. For a predefined set of bend radius, the highest bend angle that could be achieved without violating vertical geometric constraint of $6.0mm$ in equation 2.6 is 130° .

The discretization of the design parameters with 4 thicknesses, 8 bend radii, and 5 bend angles yields a total of 160 unique design points. Each combination of the discretized design parameters was evaluated on whether it violated any of the geometric constraints ($2.5mm$ and $6.0mm$) in equation 2.6 in addition to the constraint that the length $L \geq 0$. Out of the 160 discrete design points, 31 were discarded since they did not meet the desired geometric constraints (see equation 2.6 and figure 2.3). The remaining 129 design points, called feasible design points, were analyzed using parametric FE analysis.

2.4.1 Exhaustive Search Algorithm

The goal of this section is to analyze the previously (refer section 2.4) defined design parameters and develop a methodology to obtain an optimal set. The design of the sensing element must consider the energy lost due to the sliding motion between the sensor head and sensing element. The frictional loss can be modeled using a FE-based approach by defining the frictional contact regions. To achieve an optimized design for the sensing element an exhaustive search across all feasible discrete sets was performed. The algorithm to obtain the optimal design within the discrete design points is presented in figure 2.6. According to the flow chart represented in figure 2.6, the initial step consists of identifying desired design specifications and generating a design concept. A design optimization problem is formulated with an objective function defined to maximize the strain at the desired strain gauge attachment location. During this step, the dominant

design parameters (bend radius R , bend angle θ , and thickness t) are defined and their bounds are identified (refer section 2.4). Using permutations and combinations of the design parameters a set of discrete design points is generated. A single discrete design point is chosen for analysis, where first the selected combination of (bend radius R , bend angle θ , and thickness t) is evaluated in the constraint equations. If the design point meets the constraint equations criteria, then it can be used for further analysis, if not then the current design point is discarded. This procedure is applied to all discrete design points. After selecting the design point that meets the geometric constraint equations criteria, a FE-based analysis is performed and the cost of the objective function and the von Mises stress at the desired location are evaluated. The results from the FE-based analysis are postprocessed to verify if they meet the desired design specifications such as the factor of safety criterion. If the design point meets the desired specification condition (refer figure 2.6), then the design point number along with the values for the design parameters are stored as a feasible design point. If the design point does not meet the desired specification, then the design point is discarded. This iterative process continues until all the design points meeting geometric constraints are analyzed using FE. The design points meeting the geometric constraints and specification condition form the set of feasible design points. The results are then postprocessed to identify the optimal design.

2.4.2 Parametric Finite Element Simulation

This section provides a discussion on setting up the parametric model for FE analysis. The design variables of the feasible design points were parameterized in SolidWorks™ (Dassault Systemes, Waltham, Massachusetts, US) CAD modeling software. The feature of the sensor head interacting

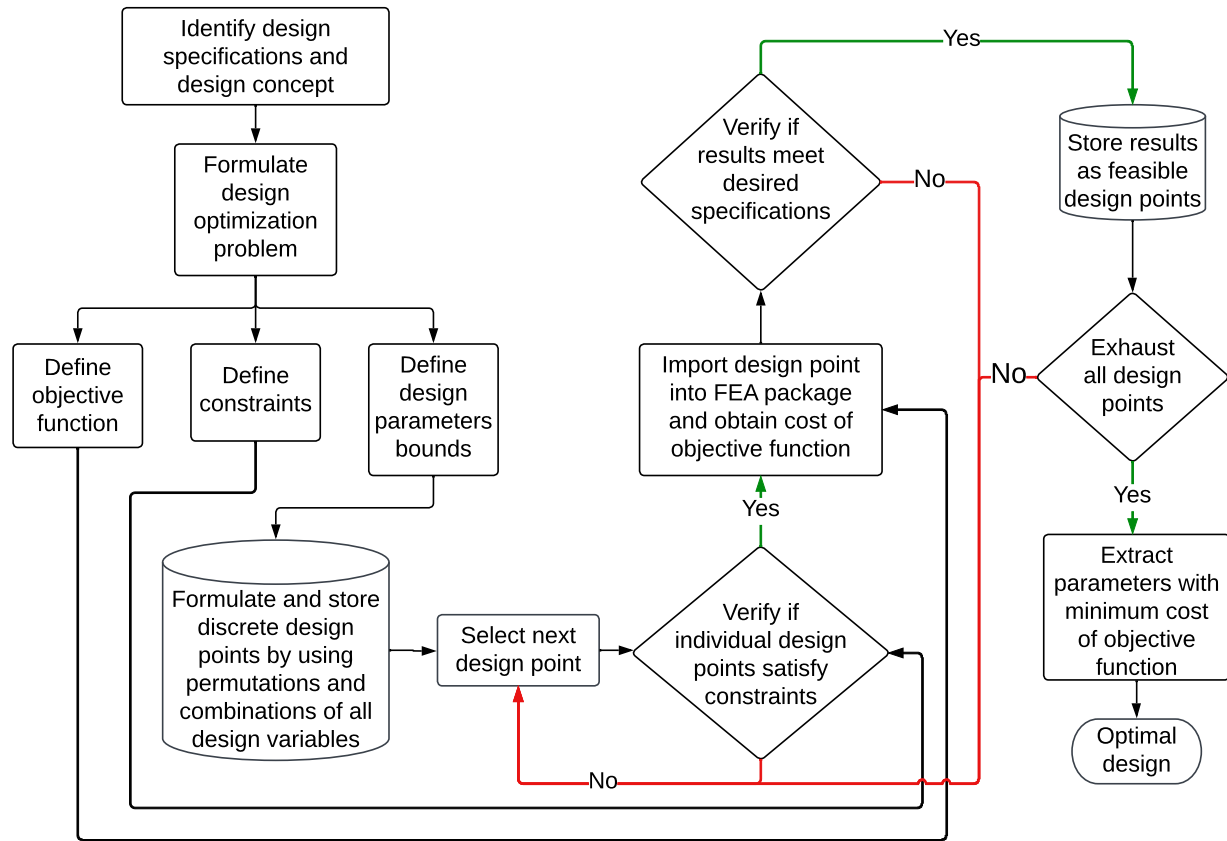


Figure 2.6: Process flow diagram to obtain optimal design from the discrete design points using exhaustive search criteria

with the sensing element was modeled to automatically align at the desired interaction location (location D in figure 2.4a) on the sensing element through the geometric constraints presented in equation 2.6. The solid model was imported into the finite element program ANSYS™ Workbench R21.1 (Canonsburg, Pennsylvania, US). The imported CAD model was further processed to automate the exhaustive search discrete optimization algorithm by defining the design parameters in Ansys™ DesignModeler R21.1.

The complex features of the sensor head and sensor base component indicated fabrication using an additive manufacturing process (further discussion on fabrication is provided in section 2.5). The material properties of Formlabs™ Grey resin were assigned to the sensor head and sensor

base components for finite element simulation [74]. The material properties of Aluminum were assigned to the sensing element [73].

The sensing element was split into three independent bodies during the preprocessing stage. The slicing feature in the FE package creates sweepable bodies to generate hexahedron meshing during preprocessing and separates the selected feature from the remainder body. Scoping a body in the FEA model aids to evaluate the results at the localized edge, surface, or body of interest. It was advantageous to estimate stress on the scoped body using the sliced body feature of the beam element which made it possible to expedite the convergence process. A symmetry boundary condition was advantageously employed (refer figure 2.7a) to reduce model complexity and improve computation time. The finite element model of the sensing element was preprocessed to obtain targeted and localized strain and improve computational time. The sensor base component was modified to retain the slot feature only which further aided in the reduction of the total number of nodes thus improving computation time. The interaction between the slots of the sensor base and the legs of the sensor head was also modeled to capture the physics of the system by defining a frictional contact between them with a coefficient of friction defined as 0.3 evaluated using controlled experimentation. The analysis was performed by setting the boundary conditions for the developed model as presented in figure 2.7b.

The mesh for the micro-force sensor was auto-generated using two different types of elements; 10–node tetrahedron and 20–node hexahedron. These elements were selected to improve the convergence rate since they offer robust adaptivity during mesh refinement and obtain higher solution accuracy due to their ability to handle complex geometric features for a computationally efficient solution [75]. The total number of nodes depends on each discrete design point due to mesh refinement. The adaptive mesh control process automatically refines the mesh density based on the

underlying geometry instead of initial coarse mesh for elements experiencing stresses greater than the desired convergence criterion during subsequent iterations. This refinement process iterates until either the defined convergence criterion of 1% or the maximum number of refinement loops are met. A representative mesh with 77065 nodes is shown in figure 2.7c.

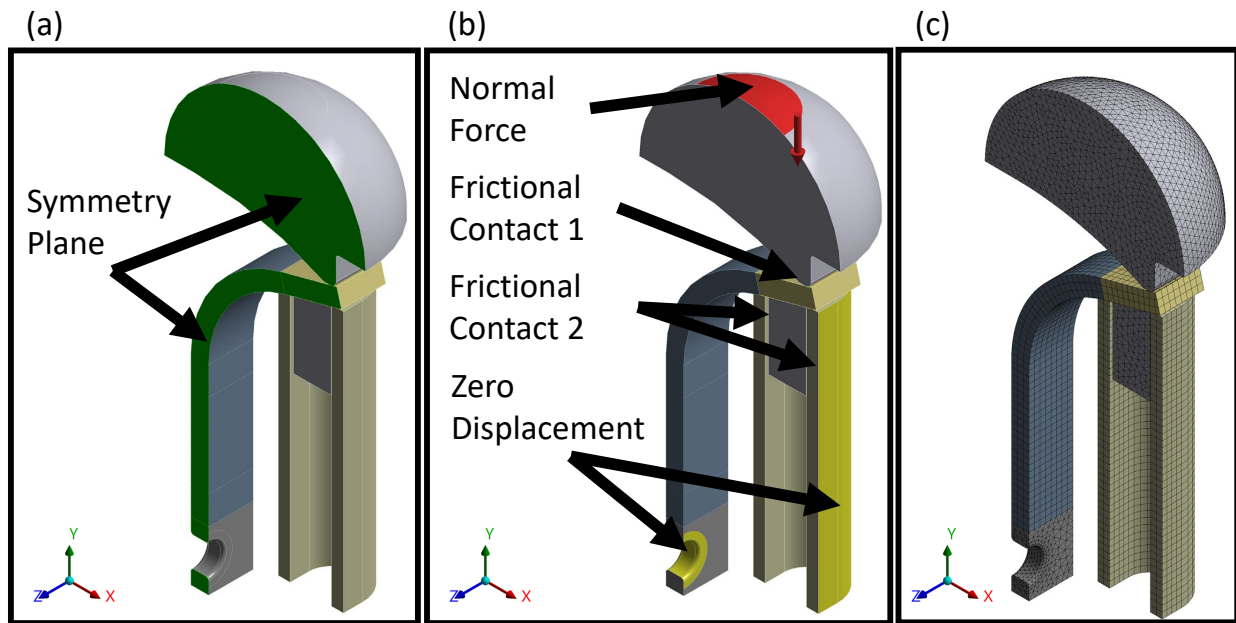


Figure 2.7: FE-based model with (a) half model cut at the plane of symmetry (b) Boundary conditions (c) an overview of the generated mesh

It was required that the sensing element withstand the maximum load of $1N$ as well as being capable of sensing a change in load of at least $20mN$ according to the desired specifications (refer 2.1). Reducing the desired minimum load from $20mN$ to $10mN$ will not only help in improving the sensitivity, but will also aid in establishing initial contact with the surface normal to sensor head axis. Following that, two equivalent loading conditions of $10mN$ (1.01 gram) and $1N$ (101.97 grams) were applied. Since symmetry was imposed as one of the boundary conditions, the actual loads applied on the top surface of the sensing head were $5mN$ and $0.5N$. The normal strain along the Y-axis was evaluated at the desired location of $0.48mm$ below the starting point of the

bend which is indicated as ‘Top strain probe’ in figure 2.8a. This location was selected considering the central axis of the active length of the identified strain gauge with respect to the strain gauge backing as presented in figure 2.3a.

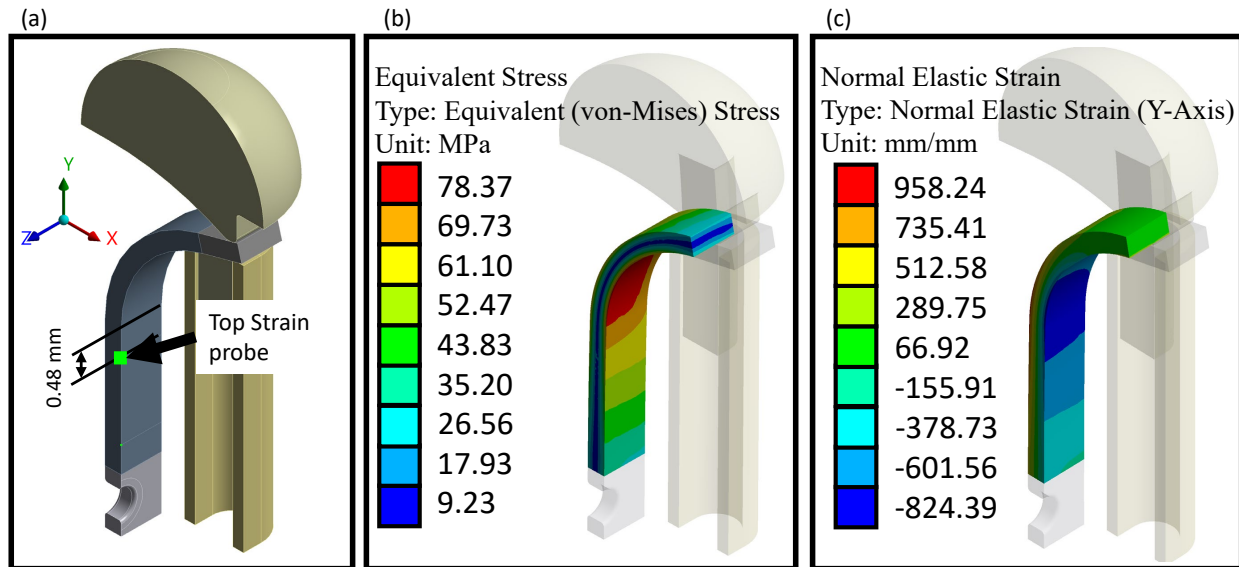


Figure 2.8: FE-based model with (a) location at which strain will be evaluated, (b) von Mises stress for the beam element with manufactured design variables, (c) Normal elastic strain distribution along the global Y-axis, due to an applied load of $0.5N$

The von Mises stress (distortion-energy approach) distribution is evaluated for all design points along the scoped body of the sensing element. Figure 2.8b shows the results of the von Mises stress distribution due to the maximum loading condition for a single discrete design point with design parameters $R = 2.2mm$, $\theta = 110^\circ$, and $t = 0.3mm$. A maximum value of von Mises stress was evaluated at the start of the bend radius (location B, refer figure 2.4). Stress contour similar to the one represented in figure 2.8b were obtained for other design points. The maximum von Mises (σ_{max}) stress for each design point (due to applied load of $0.5N$) was compared with the compressive yield strength (S_y) of the material to evaluate the safety factor (N_f) according to equation 2.9 [71]. For example, a safety factor $N_f = 3.6$ is achieved for the results presented in figure 2.8b, where the maximum von Mises stress was evaluated as $\sigma_{all} = 78.37MPa$ for

aluminum (6061 – T6) with yield strength $S_y = 280MPa$.

$$N_f = \frac{S_y}{\sigma_{max}} \quad (2.9)$$

Figure 2.8c presents the strain distribution for the same design point ($R = 2.2mm$, $\theta = 110^\circ$, and $t = 0.3mm$) due to the maximum applied load of $0.5N$. The strain distribution contour aids in identifying the location along which the central axis of the active length of the strain gauge must be aligned. Furthermore, it can be deduced from figure 2.8c that the maximum compressive strain was found near the top strain probe, indicating that the active surface of the strain gauge must be positioned near the top strain probe to obtain improved sensitivity. The strain evaluated at the top strain probe and the von Mises stress due to maximum loading conditions are set as output parameters. The results from the parametric analysis are postprocessed to identify the optimal design parameters of the sensing element.

2.4.3 Optimal Design

The goal of this step in the design process was to identify the geometric parameters and maximize the cost of the objective function (absolute value strain at the top strain probe). The evaluated cost of the objective function for 129 feasible discrete design points is plotted in figure 2.9. The cross (\times) represents the cost of the objective function for all the feasible discrete design points. The circle (\circ) represents the design points exhibiting a factor of safety greater than 3.50. The diamond (\diamond) represents the design points with a beam thickness of $0.3mm$.

The optimal discrete design point (point 73) has a bend radius of $1.7mm$, a bend angle of 110° and a thickness of $0.3mm$ yielding an objective function cost and factor of safety of $894.98\mu\epsilon$ and 3.54 respectively. All designs with beam thickness $t \leq 0.25mm$ exhibited a factor of safety less

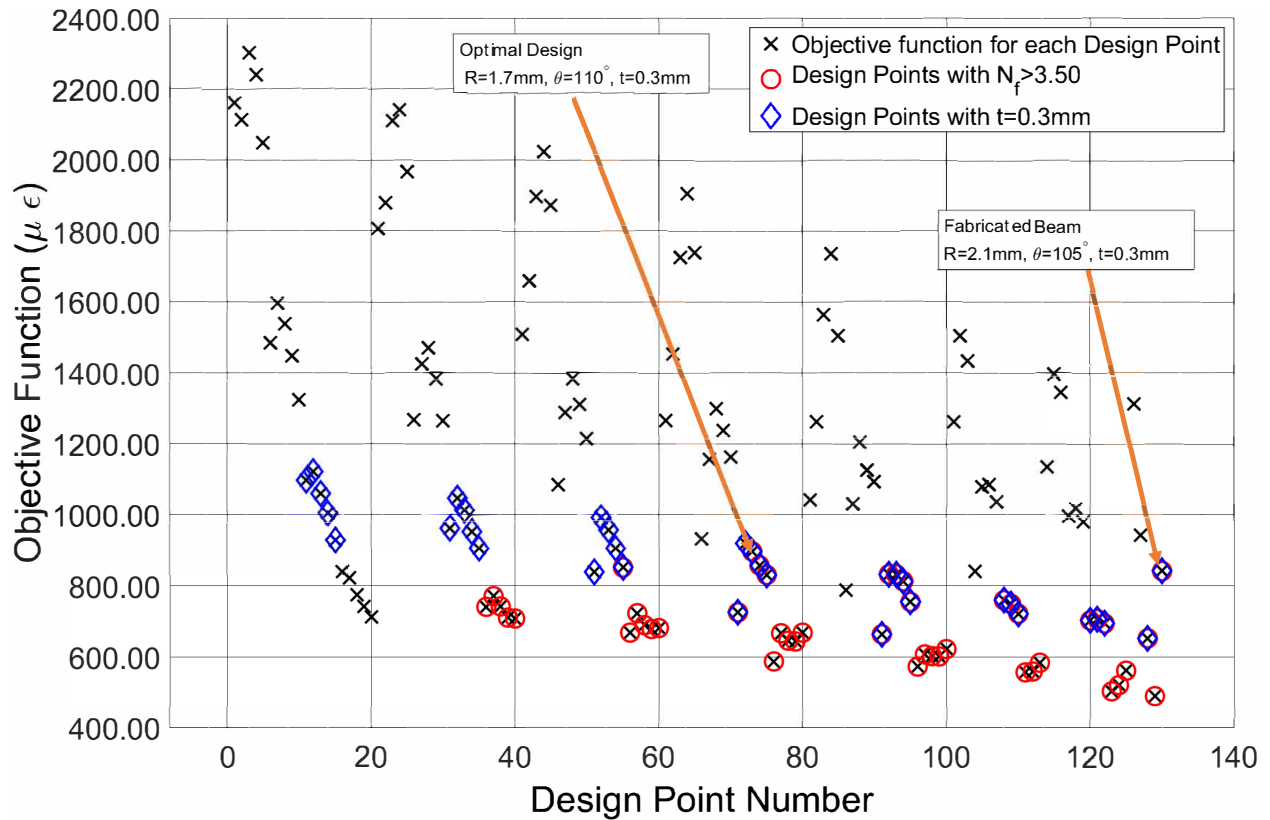


Figure 2.9: Cost of the objective function evaluated for 129 design points, along with the one for the manufactured sensing element, where the overlaying circle represents the design yielding a factor of safety greater than 3.50

than 3.5 and they were not considered for further analysis. Design point number 130 (see figure 2.9) presents the cost of the objective function evaluated using the measured dimensions of the fabricated sensing element (further discussion on fabrication provided in section 2.5). The cost of the objective function for the manufactured sensing element was evaluated to be $840.55\mu\epsilon$ with a factor of safety of 3.74.

Figure 2.10 presents the effect of bend radius and bend angle on the objective function when the beam thickness is set to $0.3mm$ which yields 32 feasible design points. The cross (\times), solid-circle (\bullet), square (\square), diamond (\blacklozenge), triangle-up (\blacktriangleup), triangle-right (\blacktriangleright), triangle-left (\blacktriangleleft), and star (\star) represent the design points with bend radii of 0.2, 0.7, 1.2, 1.7, 2.2, 2.7, 3.2, and $3.7mm$ respectively. Data points marked with an overlaying circle (\circ) represent design points with a factor

of safety ≥ 3.5 . The results of the finite element analysis using the fabricated beam dimensions for the sensing element are shown with the plus symbol (+) in figure 2.10.

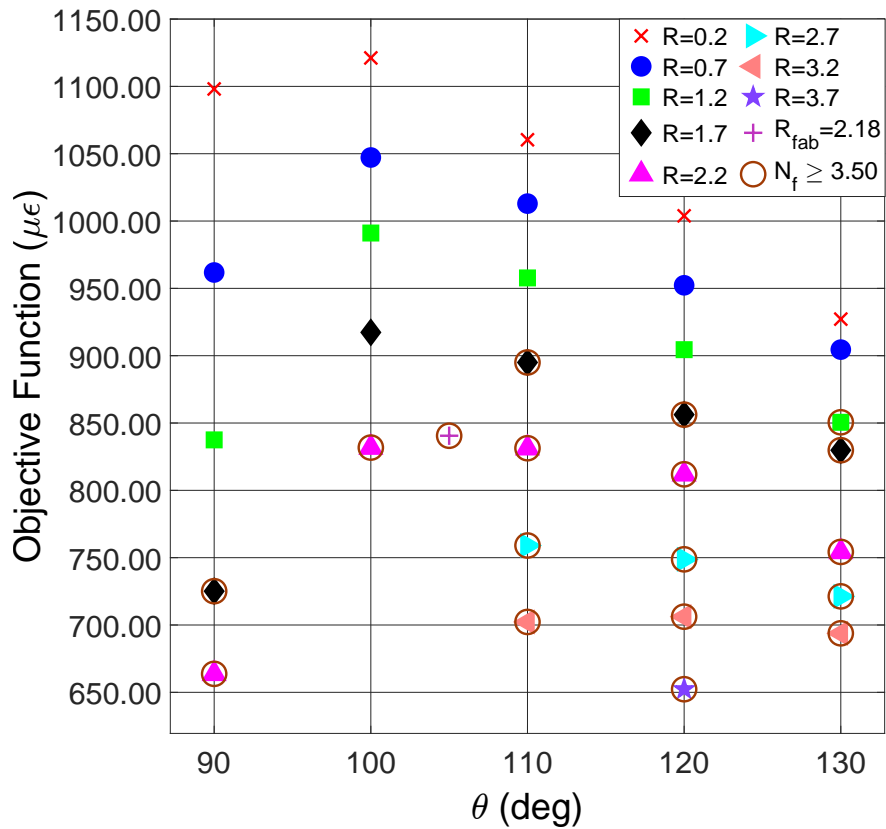


Figure 2.10: Effect of bend radius and bend angle on the cost of the objective function for feasible design points and fabricated beam ($Beam_{fab}$) with $0.3mm$ thick sensing element

As the bend angle increases from 90° to 100° the cost of the objective function increases for all bend radii. However, further increasing the bend angle reduces the cost of the objective function. The optimal discrete design point meeting all design specifications and constraints is shown in figure 2.10 having a radius $R = 1.7mm$ (\blacklozenge), a bend angle $\theta = 110^\circ$ and cost function $\gamma_b = 894.98\mu\epsilon$.

Not all design points with $1.7mm$ bend radius yield a safe design (safety factor greater than 3.5). However, it is observed that if the bend radius increases to $2.2mm$ or higher, then all feasible design points yield safe designs. This observation could prove useful during prototyping of the

sensing element considering manufacturing constraints. The important dimensions of the sensing element were evaluated to be bend radius $R = 1.7mm$, bend angle $\theta = 110^\circ$ and thickness $t = 0.3mm$. The modified conceptual design significantly improved the sensitivity of the sensor, and would be investigated further to derive the performance matrix by developing a working prototype.

2.5 Micro-Force Sensor Fabrication Methodologies

2.5.1 Manufacturing of Sensor Housing Components

Due to the geometric characteristics, sizes, and intricate features of the sensor base and sensor head components, additive manufacturing served as a rapid prototyping platform without the need of developing special fixtures and molds otherwise required during conventional machining procedures. Low force inverted vat photopolymerization, an additive manufacturing technology, was investigated for prototyping purposes and especially rapid prototyping of sensor components during design modifications. Although, desired feature sizes of the sensor housing components were well within the fabrication specifications of a Form3 printer, initial printing attempts were not successful [76]. These unsuccessful print attempts were overcome by controlled experimentation and placing the components in various orientations with respect to the print bed [40]. Figure 2.11a shows cured sensor head components fabricated in three different orientations with respect to the print bed. Based on the defects identified in the functioning features of the sensor head component, figure 2.11 classifies the sensor head component as having a good orientation or a bad orientation print.

A cured sensor base component fabricated in two distinct orientations is shown in figure 2.11b. The cylindrical surface for one of the builds was facing the print bed and for the other was facing

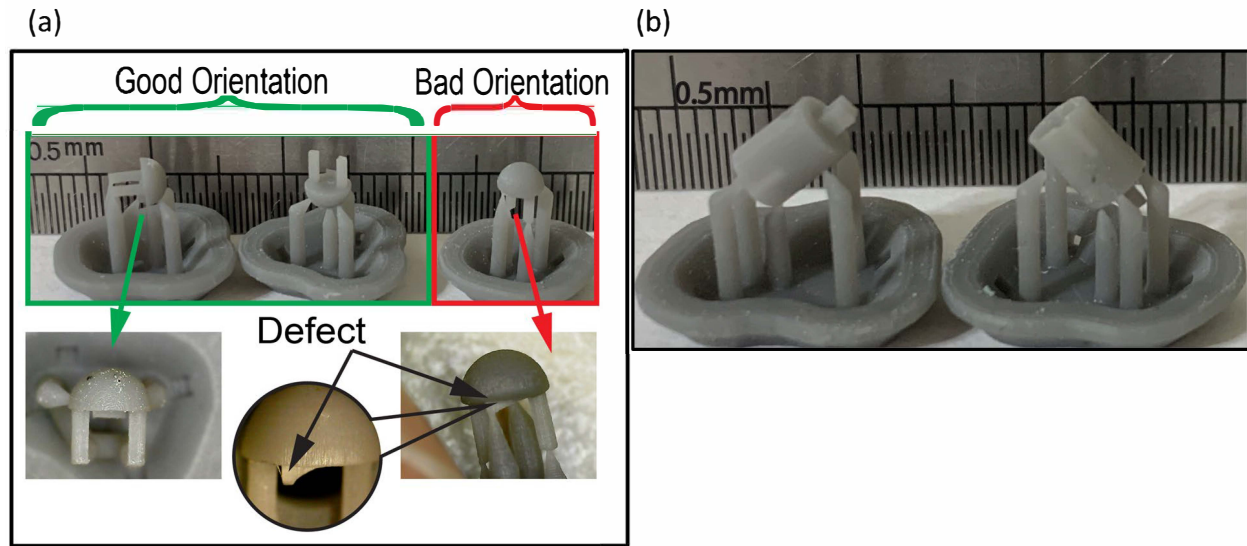


Figure 2.11: Actual scale cured (a) sensor head component fabricated in different orientations to highlight good and bad orientations and defects (b) sensor base component fabricated in different orientations [40]

away from it. Both build orientations were set to 65° with respect to the print bed. In order to fabricate the embedded features of the sensor base component it was important to ensure that no resin got clogged within the hollow part of the component during prototyping. Both build orientations for the sensor base component proved to be acceptable. The components printed in the good orientation were not only defect free but also had good dimensional accuracy. A dimensional comparison of as-designed and as-fabricated components is presented in table 2.2. A maximum deviation of $183\mu m$ between as-designed and as-fabricated dimensions was observed for the sensor head diameter.

2.5.2 Manufacturing of Sensing Element

The sensing element was prototyped using a $0.3mm$ thick aluminum sheet. A $0.5mm$ through hole was drilled at $0.8mm$ away from the base. Additionally, a marking was made at $3.3mm$ from the base to represent the start of the bend radius. An off-the-shelf dowel pin with ($\phi 4.00mm$)

Table 2.2: Comparison of as-designed and as-fabricated dimensions of the 3D printed components of the sensor

Feature name	Designed dimension (mm)	Fabricated* dimension (mm)	Absolute difference (μm)
Sensor base diameter	3.400	3.301	99
Sensor base height	4.650	4.784	134
Length of rectangular slot on sensor base	2.600	2.726	126
Sensor head diameter	3.400	3.217	183
Load transmitter thickness on sensor head	0.200	0.221	21

* measured using a Supereyes microscope system.

was used to generate a bend radius of $2.15mm$ at the neutral axis for a $0.3mm$ thick aluminum sheet. According to finite element analysis, a bend radius of $2.15mm$ ensures a safe design with an objective function of $833.40\mu\epsilon$ when the bend angle was 100° . A 3–point bend press with an off-the-shelf 90° die was used to bend the aluminum sheet which will experience spring back after bending. These specifications and conditions, even though not the optimal ones, were selected for the fabrication of the sensing element due to the availability of fabrication resources. The spring back affects the final bend radius R_f which can be calculated according to equation 2.10 as a function of the initial bend radius R_i , thickness t , material yield strength S_y , and modulus of elasticity E of the sheet metal [72].

$$R_f = \left(\frac{1}{4 \left(\frac{R_i S_y}{Et} \right)^3 - 3 \left(\frac{R_i S_y}{Et} \right) + 1} \right) \cdot R_i \quad (2.10)$$

The length of the neutral axis of a curved member, L_b , also called bend allowance, is a function of the inner bend angle α , the bend radius R , the thickness of the sheet metal t , and the spring back factor k ($k = 0.5$ for $R > 2t$) as presented in equation 2.11 [72]. According to classical machine design theory, the length of the neutral axis remains the same before and after bending [71]. This property is employed to develop an expression for the final inner bend angle α_f as function of the

initial inner bend angle α_i as shown in equation 2.12. The inner bend angle α is shown in figure 2.4b.

$$L_b = (R_i + kt) \cdot \alpha_i = (R_f + kt) \cdot \alpha_f \quad (2.11)$$

$$\alpha_f = \frac{R_i + kt}{R_f + kt} \cdot \alpha_i \quad (2.12)$$

An expression for the final bend angle θ_f is obtained by combining equations 2.11 and 2.12 to yield equation 2.13.

$$\theta_f = \pi - \alpha_f = \pi - \left(\frac{R_i + kt}{\frac{R_i}{4\left(\frac{R_i S_y}{Et}\right)^3 - 3\left(\frac{R_i S_y}{Et}\right) + 1} + kt} \right) \cdot \alpha_i \quad (2.13)$$

Using equations 2.10 and 2.13, the final bend angle of the sensing element due to spring back is calculated to be $\theta_f = 97^\circ$ when the initial inner bend angle $\alpha_i = 90^\circ$ and the initial bend radius $R_i = 2.15mm$ for aluminum with yield strength $S_y = 280MPa$, modulus of elasticity $E = 70GPa$, spring back factor $k = 0.5$, and thickness $t = 0.3mm$.

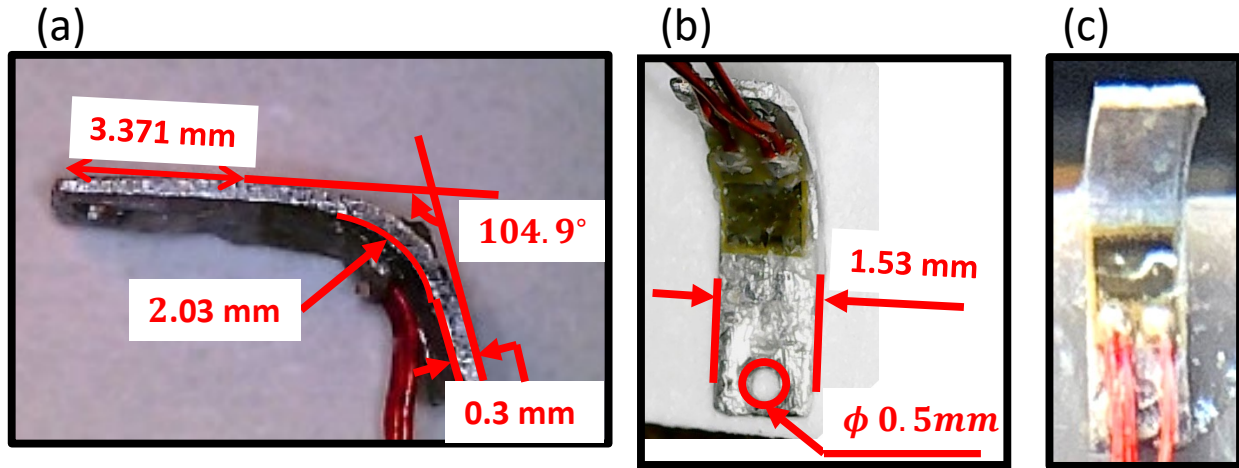


Figure 2.12: Sensing element with attached strain gauge; (a) side view orientation showing beam length, bend angle, and radius of curvature, (b) front view orientation showing dimensions of width and mounting hole of the beam (c) front view of the sensing element with the strain gauge attached in an orientation that caused wire harnessing issues

The dimensions of the fabricated sensing element were measured using Supereyes® Microscope (Shenzhen, Guangdong, China) and are shown in figure 2.12. The measurements yielded an

inner radius $R_{f-fab} = 2.03mm$, a neutral axis bend radius $R_{neutral-fab} = 2.18mm$, a bend angle $\theta_{f-fab} = 104.9^\circ$, and thickness $t_{fab} = 0.3mm$. The fabricated measured parameters were used to perform a finite element analysis with a load of $0.5N$ (using the symmetric model). The cost of the objective function and factor of safety were evaluated to be $\gamma_b(R_{f-fab}, \theta_{f-fab}, t_{fab}) = 840.55\mu\epsilon$ and $N_f = 3.74(> 3.5)$ respectively.

2.5.3 Micro-Force Sensor Assembly

After fabricating the sensing element, the identified metal foil micro strain gauge was positioned on the vertical surface of the beam. Initially, the strain gauge was positioned as depicted in figure 2.12c, resulting in an issue concerning wire harnessing. The lead-wires of the strain gauge obstructed the mounting hole feature of the beam. To address this challenge and continue with the sensor assembly and sensor characterization, the strain gauge was reoriented in an upside-down orientation as illustrated in figure 2.12b while ensuring that the active length of the strain gauge remains on the flat vertical surface of the sensing element. Figure 2.13 provides an exploded view of the fabricated prototype. The assembled micro-force sensor will be used to characterize its performance.

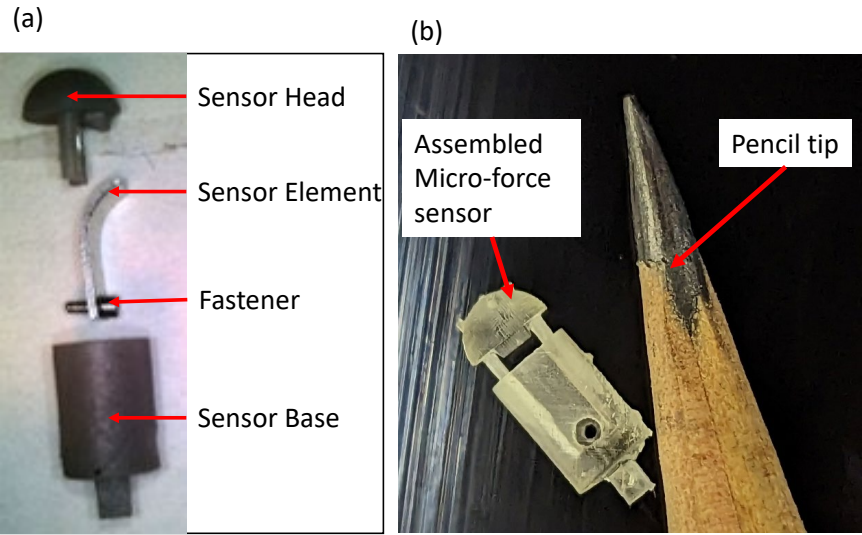


Figure 2.13: Fabricated micro-force components (a) Exploded view of manufactured components that will be used to develop the performance matrix of the micro-force sensor, (b) assembled micro-force sensor without sensor element with a pencil tip alongside for size comparison

CHAPTER 3

MICRO-FORCE SENSOR CHARACTERIZATION

3.1 Introduction

This chapter presents the discussion for characterizing the prototyped micro-force sensor as a next step according to the sensor design methodology presented in figure 2.2. The chapter is distributed into two major sections, identified as characterization setup-I and characterization setup-II. The micro-force sensor was prototyped, assembled, tested and calibrated at the MARS research laboratory. The schematic of the micro-force sensor is presented in figure 2.4, while an assembly of the prototyped micro-force sensor is presented in the inset of figure 3.1. The performance of the sensor was characterized by evaluating its sensitivity, repeatability, calibration equation, accuracy, precision, and hysteresis. Evaluating these characteristics will enable the generation of the performance matrix of the assembled force sensor to determine if the experimentally obtained characteristics meet the desired performance specifications.

Initial attempts to build the sensor characterization test-bed are presented and the data obtained from these experimentation were postprocessed and analyzed to obtain the performance metric as they relate to resolution, sensitivity, accuracy, and precision. Limitations from the characterization setup-I were identified relating to the ability to collect sensor responses to analyze its repeatability and hysteresis. Subsequently, the characterization setup-I was modified to provide the means to collect data to allow for the evaluation of the repeatability and hysteresis performance. The modified (motorized) characterization setup was called as characterization setup-II. The results obtained

from both characterization setups are presented in this chapter. The chapter will conclude with a summary of the performance matrix as it relates to the desired performance specifications.

3.2 Characterization Setup-I

The objective of building this setup was to determine the sensitivity, linearity, accuracy, and precision of the micro-force sensor. These parameters are fundamental to evaluating the performance and ensuring the suitability of the micro-force sensor for its intended application to measure tissue relaxation forces *in vivo*. Figure 3.1 presents the platform developed to perform sensor calibration experiments.

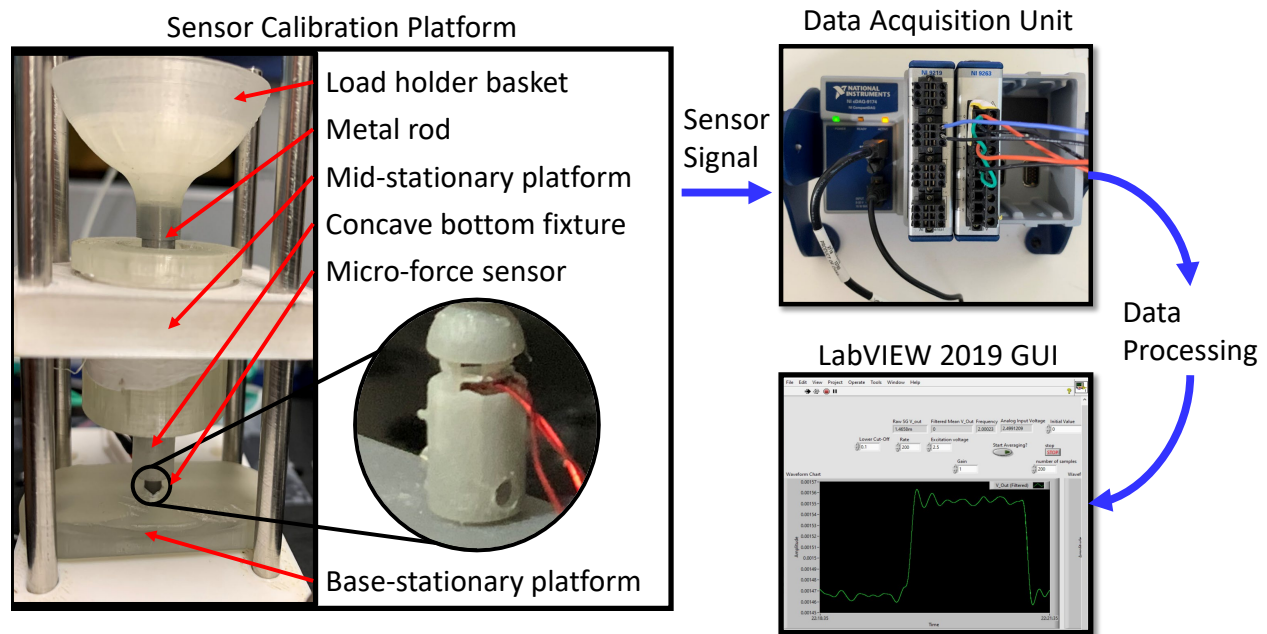


Figure 3.1: Sensor calibration platform with micro-force sensor encompassed in a fixture along with National Instruments based data acquisition system and a sample graphical output generated using National Instruments LabVIEW™ interface when loaded with a dead weight

The block feature (refer figure 2.3) of sensor base component was securely mounted on the base-stationary platform. A mid-stationary platform was used and adjusted to maintain a desired distance from the base-stationary platform such that the concave bottom fixture will make contact

with the sensor head component. A linear bearing was press-fit at the central location of the mid-stationary plate which served as a guide for the metal rod. A metal rod was guided from the central location to interact with the sensor head using a concave bottom fixture attached at the distal end, while the upper part of the metal rod was attached to a load holder basket component. The load holder basket was used to place the dead weights. The concave bottom fixture that interacted with the sensor head component transferred the load of dead weights to the top of the sensor head component, and thus to the sensing element component as discussed in the design section 2.3. The dead weights used to characterize the micro-force sensor were validated using high resolution (0.0001 grams) digital weighing scale (Model: RC 250S, Sartorius™, Goettingen, Germany). The dead weights measured in grams were then evaluated and presented in newtons for consistency throughout this dissertation considering an acceleration of gravity of $9.81m/s^2$.

The signal generated by the micro-force sensor is acquired by a 24-bit (Model: NI-9219, National Instruments™, Austin, TX) data acquisition (DAQ) module mounted on a NI-9174 chassis connected to a computer running NI LabVIEW™ via USB connection. NI LabVIEW™ was programmed to read the resistance from the strain gauge using a four-wire resistance measurement technique. The sampling rate of the data acquisition device was set to $1kHz$. The experimental procedure involved loading the sensor and recording the reaction from the sensor for 45 seconds, followed by unloading the sensor and recording the response for another 45 seconds. These controlled randomized experiments were carried out four times. The characterization procedures were performed with the loading and unloading of the dead weights in randomized order with a single factor (applied load) at 15 distinct levels ranging from $0.09N$ to $1.07N$. The weight of the metal rod, load holder basket and the concave bottom fixture (refer figure 3.1) summed up to be $0.09N$ (9.1743 grams). The maximum load ($1.07N$) was defined based on the weight of the metal rod, load holder

basket, the concave bottom fixture, and the dead weight labeled as 100*grams*. The distinct loads applied on the sensor were 0.09*N*, 0.15*N*, 0.20*N*, 0.29*N*, 0.37*N*, 0.41*N*, 0.48*N*, 0.57*N*, 0.62*N*, 0.68*N*, 0.75*N*, 0.79*N*, 0.87*N*, 0.94*N* and 1.07*N* (9.1743, 15.2905, 20.3874, 29.5617, 37.7166, 41.7941, 48.9297, 58.0104, 63.1008, 69.3170, 76.4526, 80.5301, 88.6850, 95.8206, 109.0724 grams).

3.2.1 Resolution-I

The resolution of the micro-force sensor is its ability to detect the smallest measurable change in the resistance of the strain gauge due to a corresponding desired smallest change in applied load. Since a strain gauge is an analog component, the resolution of the measurement will depend on the data acquisition system. This dependency assumes the sensing element material and the strain gauge operate in their respective elastic limit and linear range. A four-wire resistance measurement approach with a 24-bit data acquisition equipment was utilized to measure the resistance of the strain gauge without the need to develop a Wheatstone bridge circuit. The nominal resistance of the strain gauge attached on the beam was recorded as 4956.68Ω. The NI-9219 DAQ is factory programmed to automatically select the range based upon the nominal resistance under test, accordingly a 10*k*Ω range was selected to measure the resistance of the strain gauge. A 24-bit DAQ is capable of measuring resistance in 1.19*m*Ω discrete steps, for a selected range of 10*k*Ω according to $10,000/2^{23(=24-1)}$ [77]. The equivalent strain, γ_b , due to change in resistance, ΔR_{sg} , nominal resistance, R_{sg} , and gauge factor, K , is evaluated according to equation 3.1 [78].

$$\gamma_b = \frac{1}{K} \frac{\Delta R_{sg}}{R_{sg}} \quad (3.1)$$

The smallest measurable strain was computed to be 0.117μ*ε* according to equation 3.1 when

the gauge factor, a manufacturer provided specification, $K = 2.03$, smallest measurable change in resistance $\Delta R_{sg} = 1.19 \times 10^{-3} \Omega$, and the nominal resistance of the strain gauge $R_{sg} = 4956.58 \Omega$.

3.2.2 Sensitivity-I

Sensitivity is the ability of the sensor to capture the change in output variable (resistance) for a given change in the input condition (applied weight). Since the strain gauge was attached on the inner surface of the curved member, the value of resistance decreased as the applied load increased, indicating that the strain gauge experienced compression. The signal generated from the micro-force sensor is recorded as a time-series graph in NI LabVIEW™. The time-series data obtained from the sensor was recorded and stored for postprocessing towards characterizing the micro-force sensor. Figure 3.2 presents representative postprocessed recorded data from a single experiment illustrating the randomized loading and unloading stages during sensor characterization experiments.

The equivalent strain due to applied loading condition was evaluated using equation 3.1. The equivalent strain obtained from all four characterization experiments is plotted in figure 3.3. Average strain for each loading case was evaluated and plotted as Exp_{mean} in figure 3.3. A curve fit equation (also called as the calibration equation) was evaluated based upon this average strain and is presented in figure 3.3 as well. The calibration equation can be rearranged in the form presented in equation 3.2 to calculate the sensed load from strain measurements for the evaluation of the tissue properties. Note that the experimentally evaluated calibration factor $C_0 = 738.64 \mu\epsilon/N$.

$$F = \frac{1}{C_0} \cdot \gamma_b = \frac{1}{738.64} \cdot \gamma_b \quad (3.2)$$

A few outliers were observed due to applied loads of 0.38, 0.62, 0.68, and 0.94N. This devia-

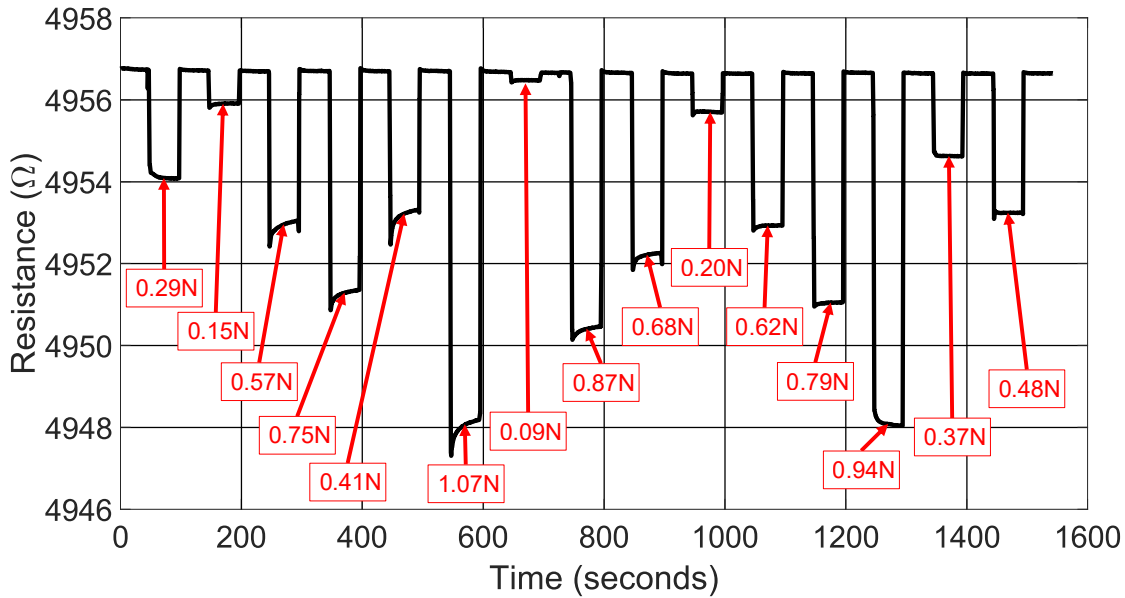


Figure 3.2: Micro-force sensor response for characterization experiments for 15 different loading and unloading stages

tion could be attributed to the load generation process and its placement procedure. For example, an applied load of 0.94N (95.8206 grams) was generated by stacking three dead weights (50, 30, and 10 grams) and placing them on the load holder basket assembly which weighed 9.6 grams. A low degree of variation from the sensor response was observed during the loading stages for 0.09N , 0.20N , 0.29N , 0.41N , 0.57N , 0.75N , 0.79N , 0.87N , and 1.07N . This low variation was due to the use of a single dead weight in generating the desired load. The characterization tests demonstrated an excellent linear behavior between the response obtained from the strain gauge and the applied load based on the coefficient of determination ($R^2 = 0.990$). A (MATLAB™, Natick, Massachusetts) script developed to postprocess and generate the micro-force sensor characterization graphs is provided in Appendix A.

A graph was generated using the characterization experiments and strain evaluated using the FE-based analysis and is presented in figure 3.4. The difference between the simulation and exper-

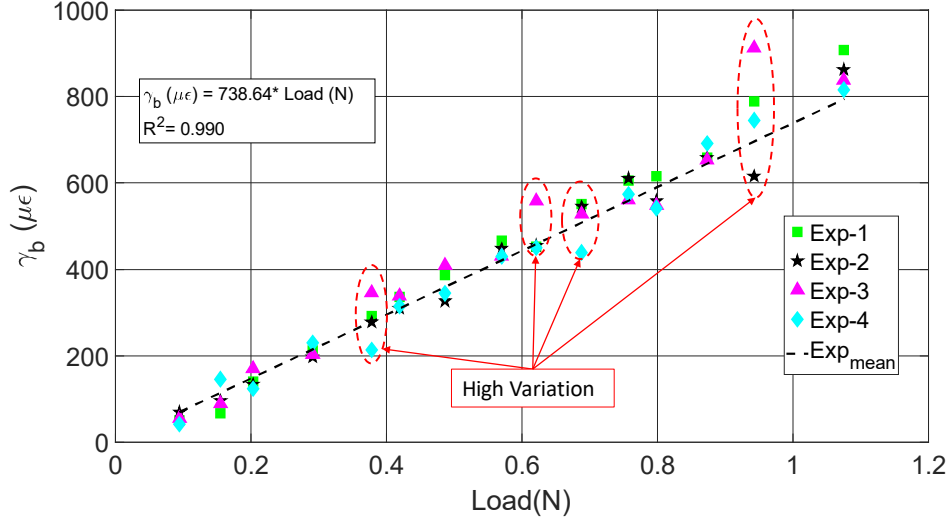


Figure 3.3: Micro-force sensor sensitivity plot with applied load ranging from 0.09 to 1.07 N (9.63 to 109.68 grams). A large variation 132.2, 108.3, 89.4 and 296.1 $\mu\epsilon$ was recorded at loading conditions 0.37, 0.62, 0.68, and 0.94N respectively

imental data is large for smaller applied loads. This difference is attributed to the frictional losses that the legs of the sensor head must overcome before the applied load is completely transferred to the sensing element. However, both experimental and simulated data follow a linear trend with slopes of 738.6 $\mu\epsilon/N$ and 790.79 $\mu\epsilon/N$ respectively. The error between experimental and simulated sensitivity (slopes) is evaluated to be 6.59% with respect to the simulated sensitivity.

3.2.3 Accuracy-I

Accuracy of the sensor is the deviation of measured output quantity from the true quantity [79]. An additional characterization experiment was conducted with an “unknown” dead weight placed on the load holder basket. The equivalent load, F , sensed by the micro-force sensor was evaluated by combining equations 3.1 and 3.2 yielding equation 3.3. Note that C_0 is the experimentally evaluated calibration factor equal to 738.64 $\mu\epsilon/N$.

$$F = \frac{1}{C_0} \frac{1}{K_{sg}} \frac{\Delta R_{sg}}{R_{sg}} \quad (3.3)$$

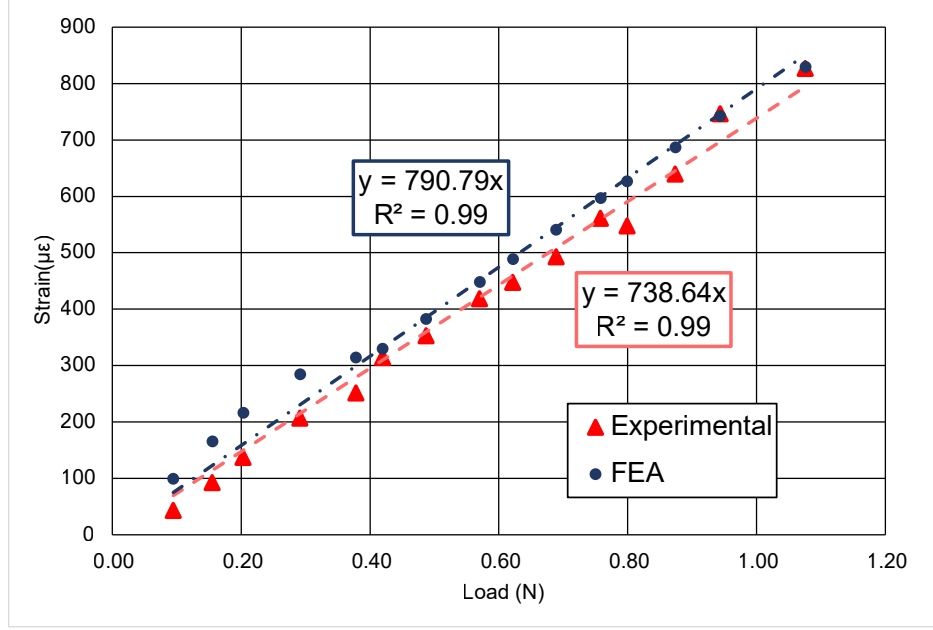


Figure 3.4: Sensitivity response for the FE-based simulation and the experimental data over full scale range of the micro-force sensor

The resulting force calculated using the calibration equation was then compared with the force due to the dead weights. The force root mean square error, F_{RMSE} , of the micro-force sensor was calculated according to equation 3.4, where, F_{mfs} is the predicted load from the micro-force sensor obtained using the calibration equation, F_{DW} is the actual load due to dead weights, i is the experiment run number, and n is the total number of experiments performed [39].

$$F_{RMSE} = \pm \sqrt{\frac{1}{n} \left(\sum_{i=1}^n (F_{mfs,i} - F_{DW,i})^2 \right)} \quad (3.4)$$

After performing a validation experiment using the same 15 sets of dead weights, a force root mean squared error was evaluated to be $F_{RMSE} = \pm 31.74mN$ (3.2grams). The root mean square error evaluated through the validation experiment demonstrates that the micro-force sensor did not provide the desired accuracy of $\pm 30mN$. The primary cause for this deviation is attributed to the effects of load placement procedure on the load holder.

3.2.4 Precision-I

Precision refers to how closely individual measurements are in agreement with the rest of the characterization experiments over any particular loading condition and is evaluated according to equation 3.5 [79].

$$Precision = \left(1 - \left| \frac{\gamma_{ms} - Avg(\gamma_{ms})}{Avg(\gamma_{ms})} \right| \right) \times 100 \quad (3.5)$$

where, the mean strain obtained over a particular loaded state of the sensor for an individual experiment is γ_{ms} and the average measurement throughout the four sets of data for similar loading conditions is $Avg(\gamma_{ms})$. The micro-force sensor data were postprocessed to obtain equivalent strain due to applied load and were sorted in increasing loading order as presented in figure 3.5. The strain reported in figure 3.5 evaluated using equation 3.1 as a function of measured change in resistance, nominal resistance, and gauge factor. A zero strain in figure 3.5 demonstrates that after each unloading instance the sensor head component rebound to its original no load state.

Figure 3.6 is a sample graph obtained by zooming in graph 3.5 at loading stage 4. The abscissa represents the timed response while the ordinate represents the strain experienced by the strain gauge. As presented in the graph, γ_{ms} was evaluated by taking an average sensor response over 20s of data for single experiment, while $Avg(\gamma_{ms})$ was evaluated by taking the average from all experiments for a loading stage over a period of 20s as well. The reason for choosing a period of 20s before unloading of the sensor head was to allow enough time for the sensor to obtain steady state response. As shown in the graph 3.6, a maximum change in strain $\approx 20\mu\epsilon$ was recorded across all four experiments during this loading condition. A $20\mu\epsilon$ change of strain corresponds to an equivalent $20mN$ change in load experienced, according to calibration equation 3.2. Using equation 3.5, a minimum precision for this particular loading condition was evaluated as 96.16%. A

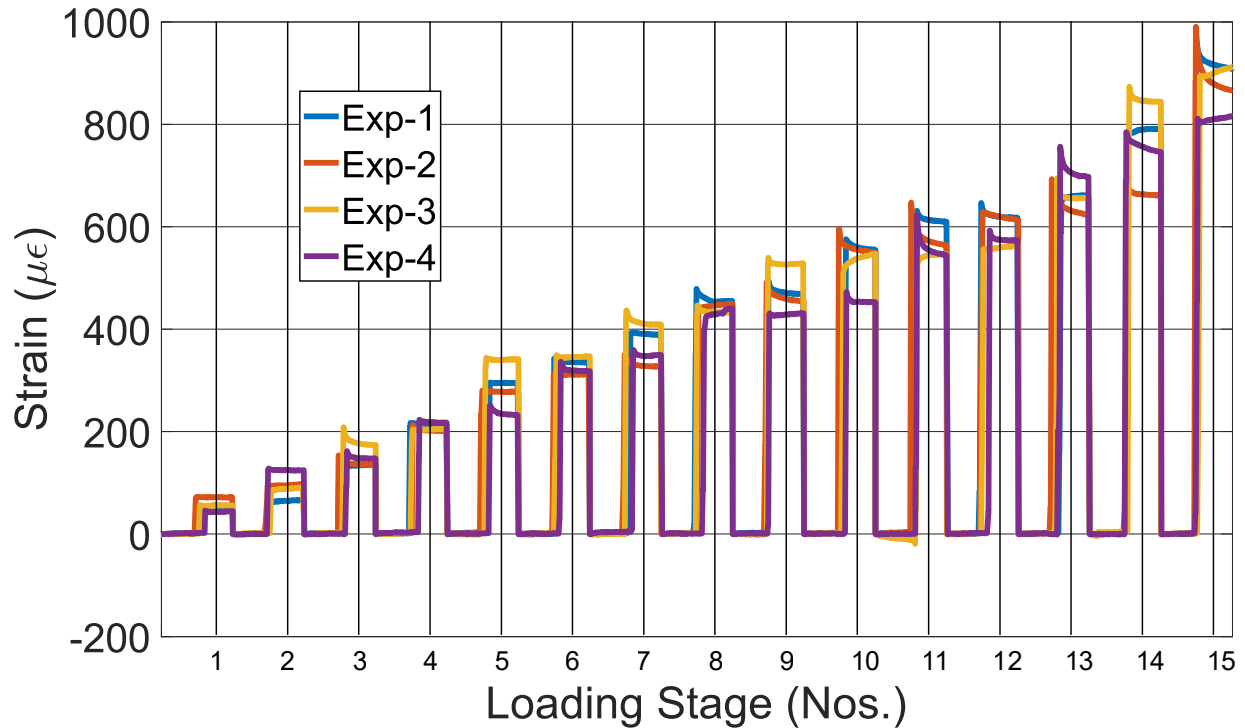


Figure 3.5: Micro-force sensor response for all four experiments sorted in ascending loading order with loading stage 1–15 corresponding to an applied load of $0.09N$, $0.15N$, $0.20N$, $0.29N$, $0.37N$, $0.41N$, $0.48N$, $0.57N$, $0.62N$, $0.68N$, $0.75N$, $0.79N$, $0.87N$, $0.94N$ and $1.07N$ respectively

similar analysis was conducted to record a precision matrix of the sensor for all loading conditions.

Table 3.1 presents the precision matrix evaluated using equation 3.5. Precision ($\geq 87\%$) with some outliers (at the loading stage with applied loads $0.155N$, $0.378N$, and $0.944N$) were obtained when the sensor experienced a load higher than $0.155N$ according to table 3.1. A low precision of the sensor was observed for several loading instances, this low precision could be attributed to the factors like placement of the dead weights on the load holder bucket while conducting the experiments and the frictional losses due to the interaction between the sensor head and the sensor base component.

Losses due to the hysteresis could not be evaluated for the fabricated micro-force sensor using characterization setup-I. The current characterization setup had limited capabilities and was not

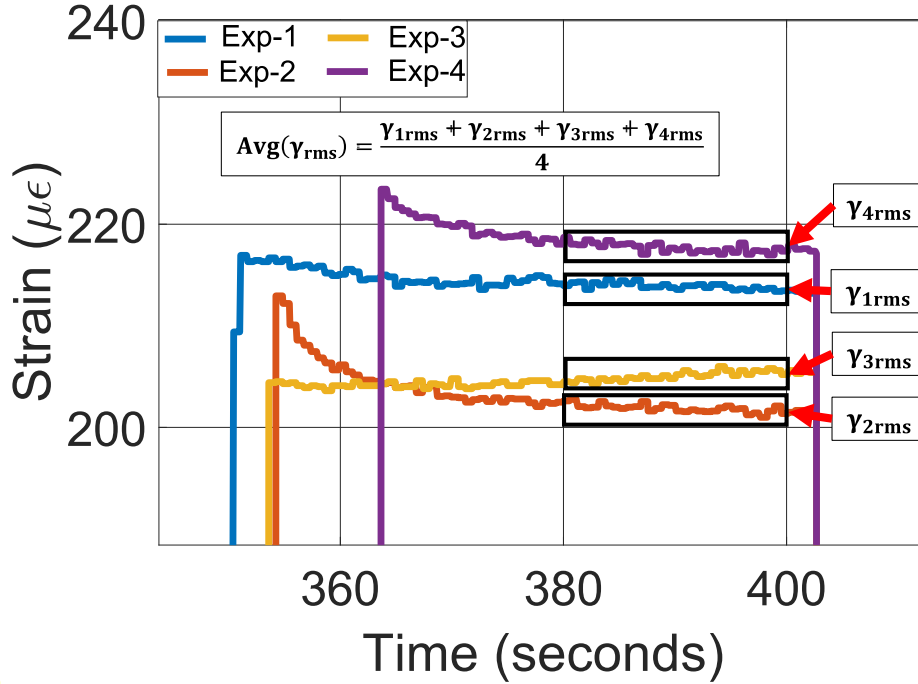


Figure 3.6: Micro-force sensor response as a time series graph for $0.29N$ obtained from all four characterization experiments

developed to record sensor data in increasing and decreasing loading order. Accordingly, the characterization setup was modified to address the limitations to achieve repeatable input conditions like applying load, at the desired location, with repeatable loading values and in increasing and decreasing order.

3.3 Characterization Setup-II

The limitations identified due to the calibration procedure using dead weights were overcome by developing and employing an automated calibration system. Initially, a high resolution ($3.1\mu m$ without microstep setting) linear actuator (Model: $28M47-2.1$, Hydeon Kerk[®] Motion Solutions, Waterbury, CT) was employed to develop the characterization test bed. A SMT series (4501017/B, MTS[®], Eden Prairie, MN, US) load cell was calibrated using dead weights and then used to mea-

Table 3.1: Precision matrix of the sensor evaluated using results obtained from characterization setup-I experiments

Load (N)	Precision (%)			
	<i>Exp₁</i>	<i>Exp₂</i>	<i>Exp₃</i>	<i>Exp₄</i>
0.094	95.89	72.89	99.23	77.76
0.155	69.87	97.49	95.44	67.82
0.203	90.76	91.77	82.04	99.51
0.291	97.97	96.31	97.82	96.16
0.378	97.18	96.89	81.14	81.43
0.420	97.76	95.02	94.44	97.17
0.487	94.29	88.83	88.96	94.42
0.570	97.25	98.75	98.01	97.99
0.622	99.74	97.04	88.01	91.23
0.689	94.08	94.95	97.09	86.13
0.758	92.51	99.97	95.82	96.71
0.799	95.63	95.79	94.59	96.82
0.874	99.76	95.03	99.13	93.92
0.944	96.39	86.87	89.18	98.71
1.076	95.64	99.90	96.86	92.60

sure the reaction load from the sensor during controlled displacement loading. The translating component of the motor was retrofitted with a load cell in series. An interaction feature was developed and attached to the distal portion of the load cell. A precision XY-stage was rigidly mounted to the base plate. A fixture holding the sensor was 3D printed, which was then attached to the precision XY-stage. The micro-force sensor was positioned using the XY-stage such that the interaction feature from the load cell would lie right above the tip of the sensor head. Figure 3.7 shows the assembled calibration setup to perform automated sensor calibration experiments. Figure 3.8 presents the front panel virtual interface developed to control the position and velocity of the 28M47 – 2.1 stepper motor where the user can define a range of parameters relating to the motor hardware and desired motion characteristics.

A safety logic is implemented to the actuation algorithm to protect the sensor from accidental overload; if the absolute value of the load cell reading is greater than 1N, then the linear actuator

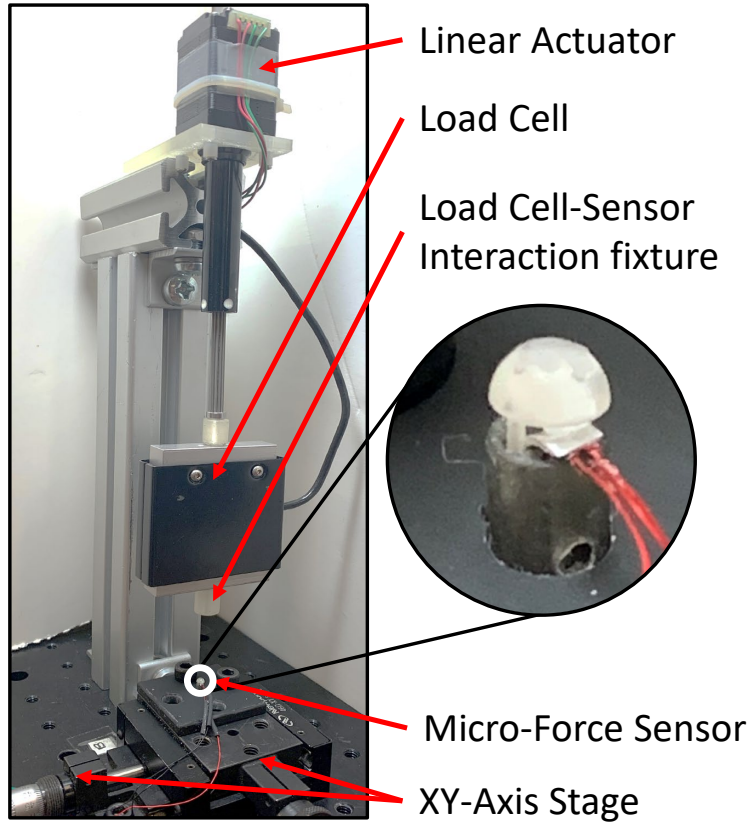


Figure 3.7: Modified calibration platform with micro-force sensor encompassed in a fixture

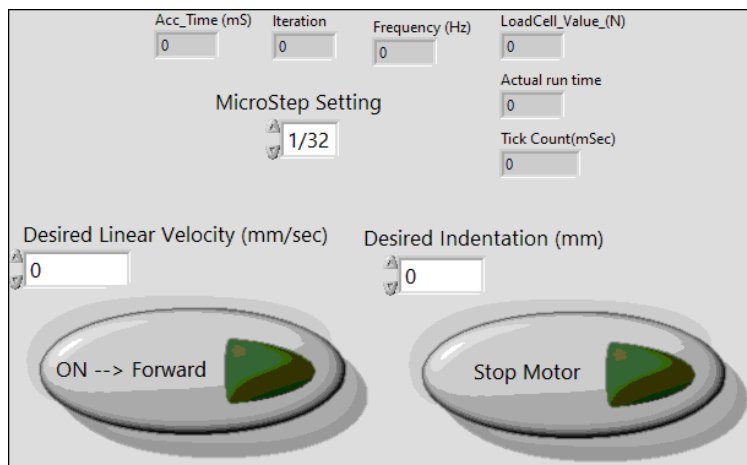


Figure 3.8: Front panel screen capture for position and velocity control of the stepper motor

will halt. Initial characterization experiments were conducted using the setup presented in figure 3.7. However, these initial experiments demonstrated that although the stepper motor was high resolution ($3.1\mu m$), the backlash generated from the lead screw contributed to poor repeatability

in position with an error as high as $\pm 20\mu m$. In light of the challenges encountered with the initial automated characterization setup (using the 28M47 – 2.1 stepper motor), it was imperative to transition to a more precise and reliable alternative. A servo motor, (Model: *MM4M – EX*, National Aperture, Inc., Salem, NH) equipped with an encoder (resolution $0.3595\mu m/count$) was investigated as an alternative actuator. The *MM4M – EX* servo motor with the encoder feedback system proved to be highly effective in maintaining position with exceptional accuracy, limiting the positioning error to $\pm 2\mu m$, and slider backlash error of $1\mu m$ according to manufacturer specifications. This transition to use a high-precision linear actuator using servo controlled motor not only mitigates the issues associated with backlash but also demonstrates promising capabilities to conduct the characterization experiments with relatively higher repeatability.

Figure 3.9 presents the modified calibration platform developed to perform the sensor calibration experiments. The block feature (refer figure 2.3) of the sensor base component was press fit to the movable plate fixture. A SMT series (Model: 4501017/B, MTS[®]) load cell was calibrated using dead weights. A spacer block was positioned between the sensor head and the calibrated load cell. The load cell was calibrated to an initial no load state considering the weight of the spacer block. A custom control algorithm and data acquisition program was generated in NI LabVIEW[™] to control the DC servo motor using a NI myRIO microcontroller.

Initially the motor was actuated by providing displacement in increments of $5\mu m$ to determine a maximum displacement needed to be applied at the tip of the sensor head in order to obtain a maximum desired load of $\sim 1N$. When a displacement of $315\mu m$ at the tip of the sensor head was applied an equivalent reaction of $0.87N$ (at steady state) was generated at the load cell. Therefore a displacement of $315\mu m$ was set as a maximum displacement to be applied. The characterization experiments were conducted using 15 controlled displacements, from zero to maximum

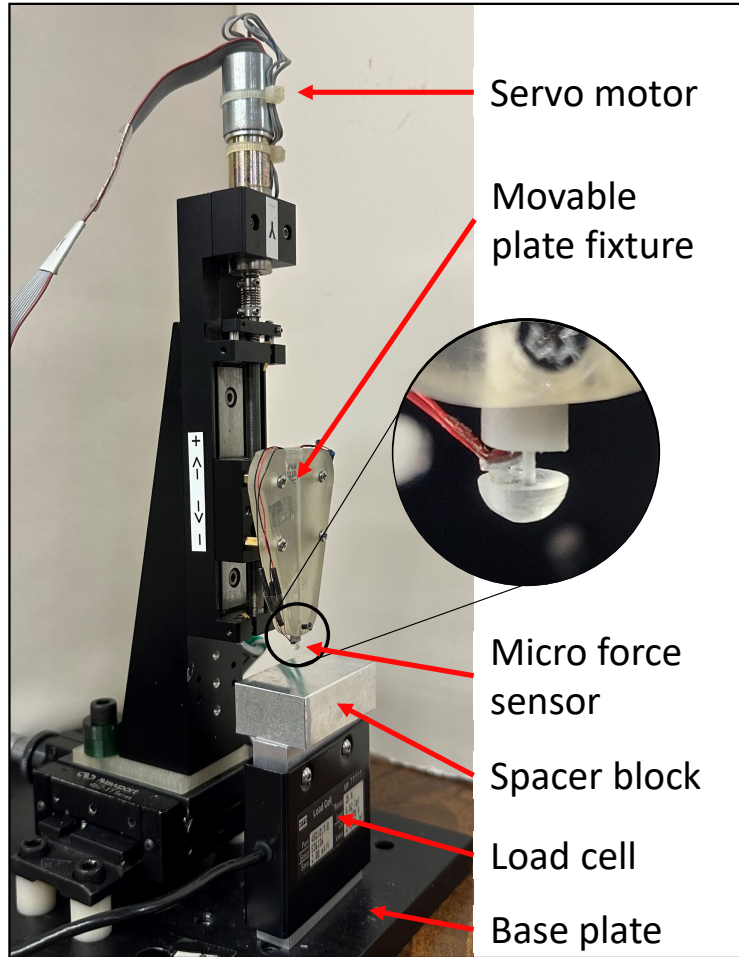


Figure 3.9: DC servo motor controlled calibration platform with micro-force sensor encompassed within the movable plate fixture and a load cell attached at the base

displacement ($315\mu m$). One characterization experiment consisted of applying the 15 controlled displacements in a randomized manner. Figure 3.10 presents the process flow diagram of the characterization setup. The control algorithm is programmed in NI LabVIEW™ to apply a step input with the amplitude being the desired displacement in microns. The period of the step input was set to 60s, as such when loaded the response of the sensor head will be recorded for 30s, and when unloaded the sensor head will retract back to its original no load state and the measurements will be recorded for another 30s.

The experiments were performed in triplicates. The applied displacements were up to $315\mu m$

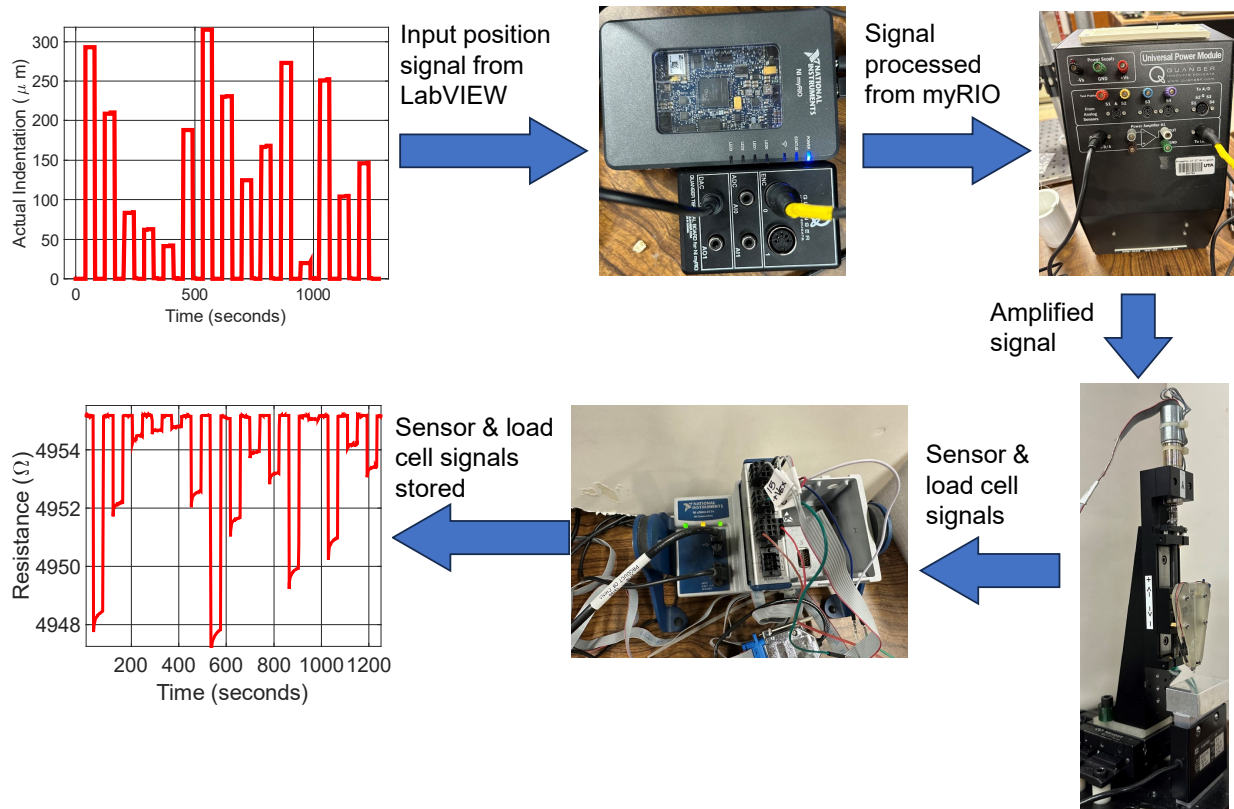


Figure 3.10: Process flow diagram of the characterization setup, with input signal generated through NI LabVIEW™ and sent to NI myRIO microcontroller, which is then amplified and fed to the linear servo actuator, the data from the load cell and the micro force sensor is recorded and stored for postprocessing

with an increments of $21\mu m$ in randomized order. The results were then postprocessed to evaluate the sensitivity, accuracy, precision, repeatability, and hysteresis of the micro-force sensor.

3.3.1 Sensitivity-II

As discussed previously in section 3.2.2 the sensitivity is the ability to measure an output due to the smallest change in the input. The interface between sensor head and the sensing element exhibits a sliding motion, leading to non-linearity between controlled displacement and sensed force as discussed in section 2.4.1.

Figure 3.11 represents the micro-force sensor response due to applied controlled displacement.

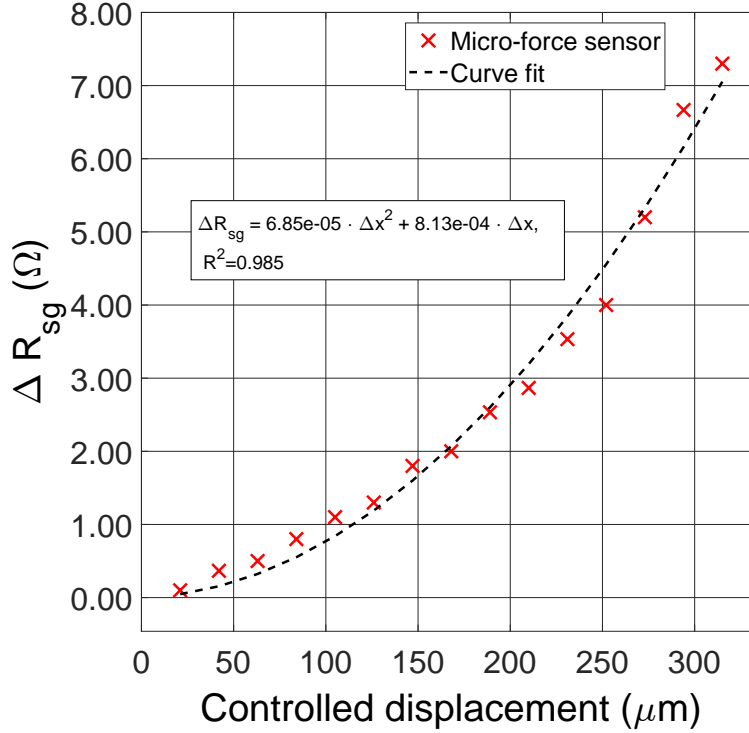


Figure 3.11: Average response data from the micro-force sensor as a function of the linear actuator displacement

A non-linear behavior between the input displacement and output change in resistance (micro-force sensor) is observed. The experimentally obtained relation of the controlled displacement $\Delta x(\mu\text{m})$ as function of the change in resistance $\Delta R_{sg}(\Omega)$ is presented in equation 3.6 with a coefficient of determination $R^2 = 0.98$.

$$\Delta R_{sg} = 68.51 \times 10^{-6} \Delta x^2 + 812.5 \times 10^{-6} \Delta x \quad (3.6)$$

Figure 3.12 presents the postprocessed experimental and FE-based sensitivity graphs. The circles (\circ) represent the strains evaluated from measured sensor signal using equation 3.1, while the squares (\square) represent the strains obtained from FE analyses.

During the characterization experiments, the change in load from the calibrated load cell and the change in resistance from the strain gauge attached micro-force sensor were recorded. The calibration equation of the micro-force sensor is shown in equation 3.7, where ΔR_{sg} is the measured

change in resistance from the micro-force sensor, C_0 is the experimentally evaluated calibration factor, $K_{sg} = 2.03$ is the strain gauge factor provided by the manufacturer, $R_{sg} = 4955.04\Omega$ is the measured no load nominal resistance of the sensor strain gauge attached on the sensing element, and ΔF is the force experienced by the micro-force sensor which is measured by the load cell.

$$\gamma_{sg} = \frac{1}{K_{sg}} \frac{\Delta R_{sg}}{R_{sg}} = C_0 \cdot \Delta F \quad (3.7)$$

$$\therefore C_0 = \frac{1}{\Delta F} \cdot \frac{1}{K_{sg}} \frac{\Delta R_{sg}}{R_{sg}}$$

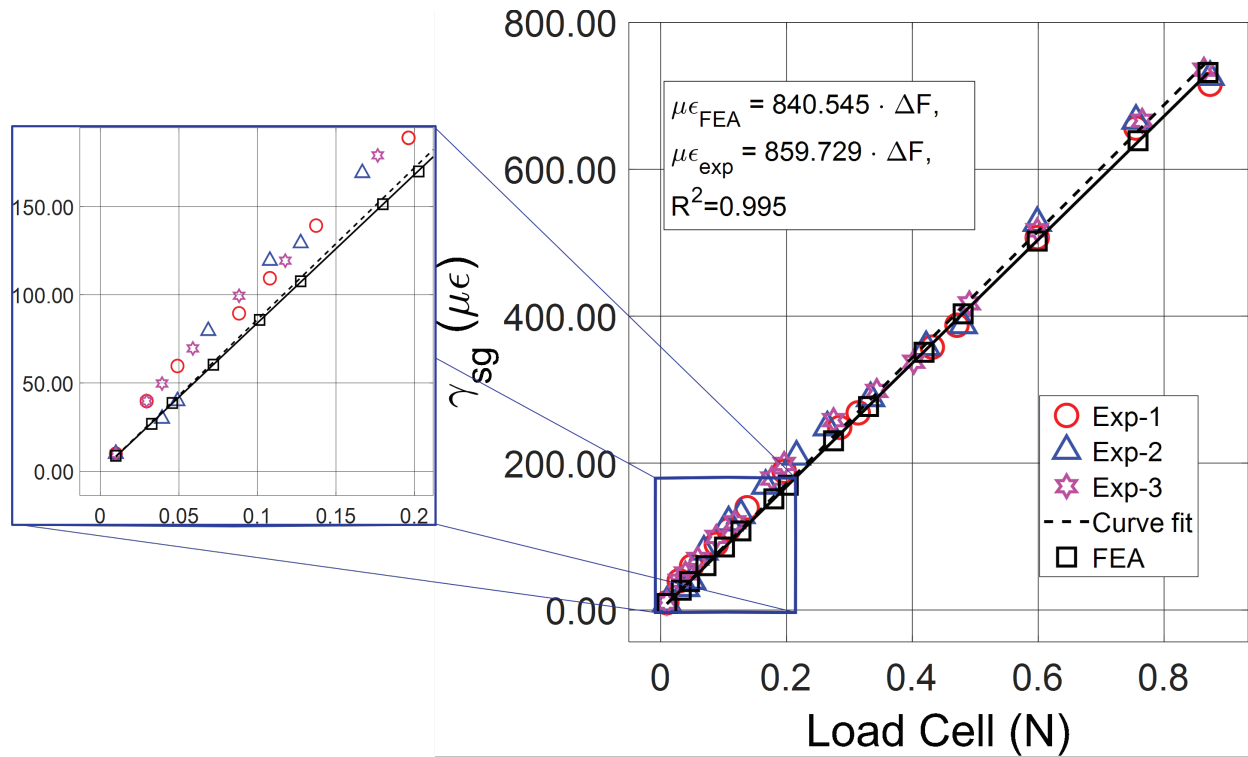


Figure 3.12: Sensitivity responses for the FE-based simulation and experimental data as a function of force experienced by the load cell

The experimental and FE-based simulated sensor calibration factor were found to be $C_{0-exp} = 859.7\mu\epsilon/N$ and $C_{0-FE} = 840.55\mu\epsilon/N$ respectively with the sensitivity plot presented in figure 3.12. The calibration analysis indicates an excellent linear behavior with a coefficient of determination of $R^2 = 0.99$ between the strain gauge sensor and the load experienced by the load cell

which further indicates that the force experienced on the sensor head can be accurately monitored and measured.

It was found that the sensitivity of the sensor exhibited variations between the two characterization setups. The increase in the sensitivity in characterization setup-II can be attributed to two primary factors: the geometric design modification of the sensor head legs feature and the material used to 3D print the component. The thickness of the sensor head legs was intentionally reduced, allowing for smoother movement within the slot feature, thereby reducing the frictional losses experienced in the prior experiments. Consequently, the FE-based analysis was reevaluated and presented in figure 3.12 by adjusting the coefficient of friction between the sensor head legs and the sensor base slot feature.

3.3.2 Resolution-II

The data acquisition module to record the sensor, and load cell response data was not modified. Subsequently, as established in section 3.2.1, the resolution of the data acquisition system allows for the measurement of a change in resistance of the strain gauge by $1.19m\Omega$ which corresponds to a change in equivalent load of $0.13mN$ by modifying the calibration equation 3.7 and solving for change in load ΔF . However, since a load cell was used to calibrate the micro-force sensor, the resolution of the load cell must be considered in evaluating the performance of the micro-force sensor¹. According to the manufacturer specifications, the MTS series load cell is capable of sensing loads with $1.00gram$ increments. Accordingly, the micro-force sensor will be characterized considering $\pm 1.00gram$ resolution.

¹The resolution of the micro-force sensor in this case is dependent on the resolution of the load cell. If a higher resolution load cell is used to characterize the micro-force sensor, then that value could be used to validate the resolution of the micro-force sensor

3.3.3 Accuracy-II

Three sets of characterization experiments were conducted to evaluate the accuracy of the sensor. Equation 3.3 can be utilized to evaluate the force F , sensed by the micro-force sensor where, the calibration coefficient is $C_0 = 859.72\mu\epsilon/N$, the strain gauge factor is $K_{sg} = 2.03$, the nominal resistance of the strain gauge is $R_{sg} = 4955.04\Omega$, and the change in resistance due to applied load is ΔR_{sg} . Figure 3.13 represents the raw data collected from the load cell and the postprocessed data from the strain gauge attached micro-force sensor for a single experiment with similar behavior observed for the other two experiments.

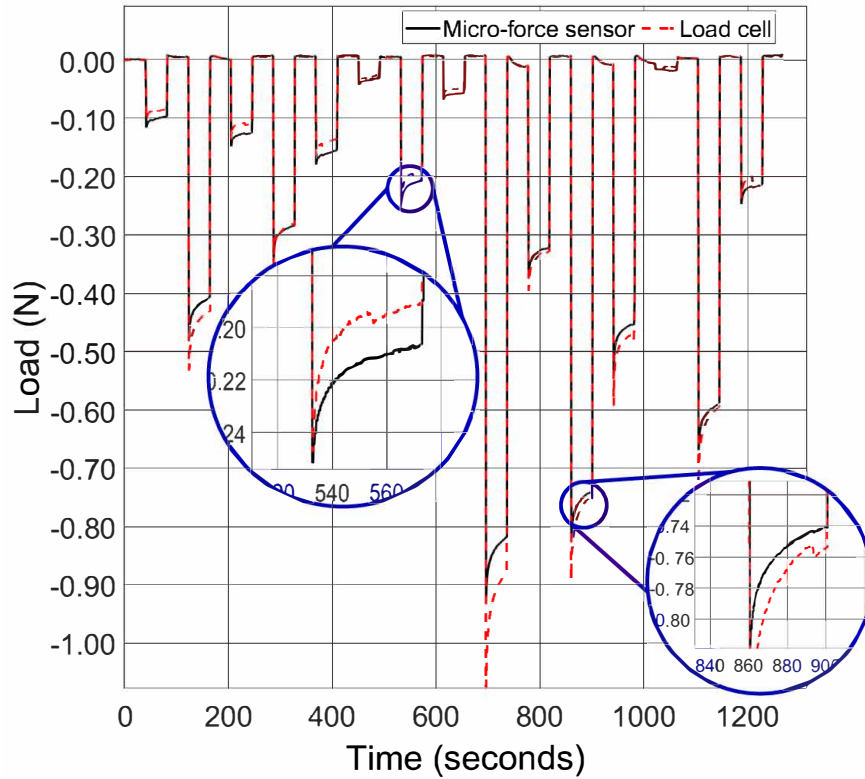


Figure 3.13: Load raw data collected from the load cell and postprocessed micro-force sensor as a time series plot (negative values indicate compressive loads)

The force root mean square error, F_{RMSE} , of the micro-force sensor was calculated by modifying the variables of equation 3.4, and rewriting it as shown in equation 3.8 where, F_{mfs} is the

predicted load from the micro-force sensor obtained using the calibration equation, F_{LC} is the load measured by the load cell, i is the experiment run number, and n is the total number of experiments performed [39]. A maximum $F_{RMSE} = 28.6mN$ ($2.9grams$) was evaluated using the three experiments which is less than the desired accuracy of $\pm 30mN$.

$$F_{RMSE} = \pm \sqrt{\frac{1}{n} \left(\sum_{i=1}^n (F_{mfs,i} - F_{LC,i})^2 \right)} \quad (3.8)$$

3.3.4 Precision-II

As discussed earlier in section 3.2.4 precision matrix aids in identifying how closely are the individual data in agreement with the corresponding loading condition obtained from other experiments. Equation 3.9 presents a modified version of equation 3.5, where, the average force evaluated over a particular input displacement for an individual experiment is represented by F_i , while the average force for all three sets of experiments for a similar input displacement is represented by F_μ .

$$Precision = \left(1 - \left| \frac{F_i - F_\mu}{F_\mu} \right| \right) \times 100 \quad (3.9)$$

Figure 3.14 shows the sensor data for the three experiments with an applied displacement of $21\mu m$ which corresponds to a load of $10mN$.

Precision values for all the controlled displacement experiments (21 to $315\mu m$) were determined using equation 3.9 and presented in table 3.2. The strain gauge-based micro-force sensor consistently demonstrated a high precision ($\geq 87.22\%$) for all displacements except the first two (21 and $42\mu m$). The low precision for these smaller displacements could be attributed to frictional energy losses between the sensor head legs and sensor base slot feature. These results are reported for completeness but they are not considered in establishing any metrics on the performance of the prototyped sensor. Moreover, the precision matrix obtained using the modified characterization

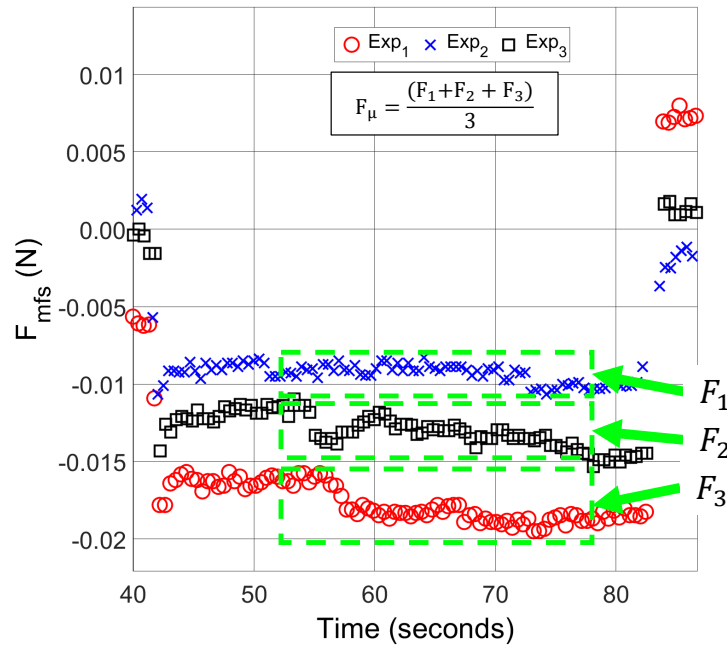


Figure 3.14: Sensor precision calculation based on evaluated force from measured ΔR_{SG} as a function of applied displacement for each of the three experiments

setup-II demonstrated relatively higher precision when compared with corresponding loading condition using characterization setup I.

3.3.5 Repeatability-II

Repeatability pertains to the level of consistency exhibited for multiple measurements obtained from a sensor or measurement system when subjected to identical input conditions [80, 55]. The repeatability of the sensor is evaluated using equation 3.10, where ΔF is the maximum deviation across all sets of experiments and F_z is the range of force measurement [55]. Figure 3.15 presents the deviation in loads evaluated from measured strain gauge-based sensor data obtained between the three experiments. The circles (\circ), crosses (\times) and squares (\square) represent the load deviations in experiments 1 and 2, experiments 2 and 3 and experiments 1 and 3 respectively. The repeatability error of the sensor was evaluated to be $\pm 3.13\%$ or $0.025N$ which corresponds to a strain change

Table 3.2: Precision matrix of the strain gauge-based sensor evaluated using results obtained from the three calibration experiments using characterization setup-II

Mean Pos (μm)	Mean $\Delta R_{sg}(\Omega)$	Mean Load (N)	Precision (%)		
			<i>Exp</i> ₁	<i>Exp</i> ₂	<i>Exp</i> ₃
21	0.1	0.01	66.96	69.10	97.86
42	0.4	0.03	80.48	81.64	98.84
63	0.5	0.05	98.57	93.57	95.00
84	0.8	0.09	87.22	97.60	89.62
105	1.1	0.11	97.88	91.30	89.19
126	1.3	0.14	93.70	99.51	93.21
147	1.8	0.19	95.13	96.78	98.34
168	2.0	0.20	96.34	94.56	98.22
189	2.5	0.28	99.80	98.26	98.46
210	2.9	0.31	97.08	97.09	99.99
231	3.5	0.43	98.13	99.11	97.24
252	4.0	0.47	98.21	99.88	98.09
273	5.2	0.60	99.92	99.17	99.09
294	6.7	0.76	98.98	99.23	99.76
315	7.3	0.87	99.84	99.84	99.68

of $22.85\mu\epsilon$.

$$\rho = \pm \left(\frac{\Delta F}{F_z} \right) \times 100\% \quad (3.10)$$

3.3.6 Hysteresis-II

Hysteresis is the phenomenon where changes in the value of a physical attribute lag behind changes in the effect causing them [81]. The largest deviation between the loading and unloading of the micro-force sensor over its defined operational range is used to assess hysteresis as a performance metric. The hysteresis is evaluated according to equation 3.11 where $F_{upscale}$ and $F_{downscale}$ represent the calculated force during loading and unloading respectively [81].

$$\psi = Max|F_{upscale} - F_{downscale}| \quad (3.11)$$

Hysteresis losses were estimated by subjecting the sensor to incremental loading intervals and

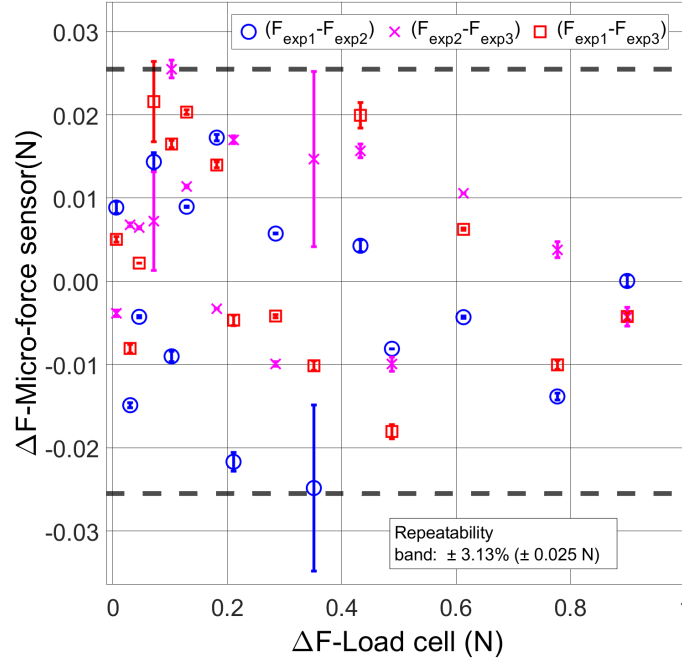


Figure 3.15: Sensor repeatability evaluated from measured resistance changes ΔR_{SG} as a function of applied displacement for the three experiments

allowing the sensor to reach a steady state with each incremental load until the desired maximum displacement was reached. Then, the unloading profile followed a decrement from the maximum displacement at predefined intervals while allowing the sensor to reach a steady state until the linear actuator reached the initial zero displacement. The equivalent load sensed by the sensor was evaluated using equation 3.3. Figure 3.16 presents the postprocessed hysteresis data from the micro-force sensor.

As the input displacement increases, the sensor response increases and provides a measurable output at the defined displacement. Using equation 3.11, a maximum hysteresis of $0.118N$ was calculated at a displacement of $273\mu m$. The hysteresis losses recorded from the sensor characterization experiments demonstrated that the assembled sensor release energy during the unloading phase. The hysteresis losses of the micro-force sensor could be attributed to multiple factors including the friction between the sensor head leg feature and the sensor base guide slots.

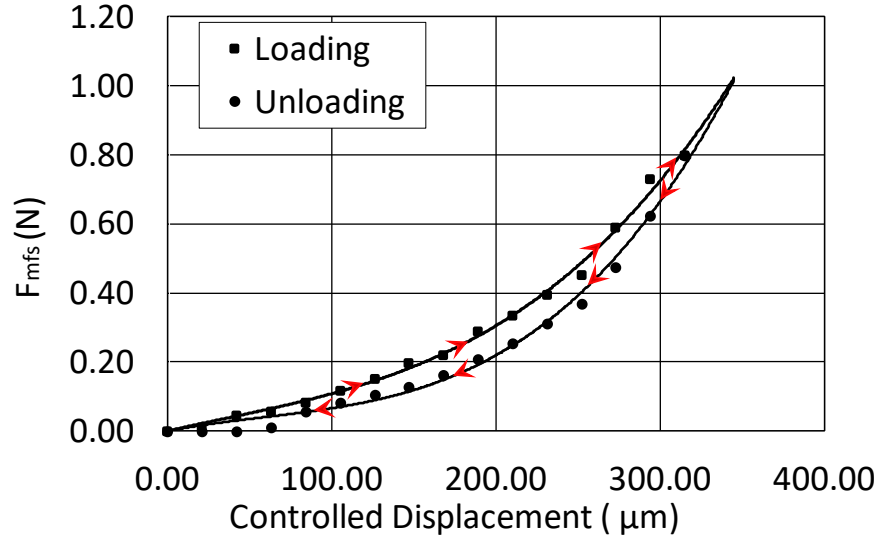


Figure 3.16: Postprocessed hysteresis response from the calibrated micro-force sensor

3.4 Performance Matrix Summary

The performance characteristics of the micro-force sensor based on experimentally obtained and processed measurements are summarized and presented in table 3.3. These results demonstrate the micro-force sensor met the desired design specifications discussed in table 2.1 for its intended use to collect tissue relaxation responses.

Table 3.3: Performance Matrix of the Prototyped Micro-Force Sensor

Characteristics	Desired Specifications	Characterization Setup I	Characterization Setup II
Dimension	$\phi \leq 3.5mm$	$\phi = 3.3mm$	$\phi = 3.3mm$
Force Range	$\leq 1.0N$	$1.07N$	$0.87N$
Sensitivity	–	$738.64\mu\epsilon/N$	$859.7\mu\epsilon/N$
Resolution	$20mN$	$0.13mN$	$0.13mN$
Accuracy	$\pm 30mN$	$\pm 31.74mN$	$\pm 28.6mN$
Precision	–	67.82%	87.22%
Repeatability error	–	–	$(\pm 0.025N) \pm 3.13\%$

The modified characterization setup demonstrated an improvement in the performance of the micro-force sensor especially for the sensitivity, accuracy and precision.

CHAPTER 4

TISSUE CHARACTERIZATION

4.1 Introduction

One of the fundamental aims of this dissertation is to demonstrate the ability of the in-house developed sensor to measure the data needed to evaluate tissue viscoelastic properties in vivo and in situ. In chapters 2 and 3, a micro-force sensor was designed, characterized and its performance matrix was developed; demonstrating that the force sensor could reliably be used to characterize soft tissue properties, for the intended application by palpating and collecting reaction force information from the interior wall of the human bladder. The human bladder, while the intended application, represents just one aspect of the potential utility of this sensor. However, in order to verify and validate the applicability of the micro-force sensor for tissue characterization, controlled testing was performed on the forearm soft tissues of human subjects. Moreover, while the initial design and the intended application of this micro-force sensor centered around the biomechanical assessment of human bladder soft tissue, the exploration into forearm tissue serves a fundamental step in broadening the micro-force sensor application for soft tissue characterization.

This chapter aims to establish a foundation for the acquisition of time-history force response information from the characterized micro-force sensor and discuss the subsequent postprocessing procedures to be employed to construct a viscoelastic model to obtain coefficients based on the experimentally collected data. Section 4.2 will introduce commonly used Standard Linear Solid (SLS) type of viscoelastic models to characterize soft tissue. In this section, a three ele-

ment Maxwell-Wiechert viscoelastic model will be presented and its solution to stress relaxation response will be evaluated. A postprocessing algorithm will be presented to obtain the elastic and viscous coefficients from the experimentally collected force response data. Section 4.3 will present the methods implemented to evaluate the viscoelastic properties of soft tissue, especially as they relate to forearm tissue. Factors affecting the viscoelastic characteristics of soft tissue will be identified. Section 4.4 will present the experimental test-bed developed for tissue characterization. Subsequently, section 4.4.1 will present the results from the initial tissue characterization test-bed. Section 4.5 will describe the test-bed used to perform the tissue characterization experiments on human subjects following the approved UTA-IRB protocol 2023 – 0306¹. Then, the results obtained from the modified tissue characterization setup will be presented and discussed. This chapter will conclude with remarks pertaining to viscoelastic properties of soft tissue as they relate to age, race, gender, and arm strength training.

4.2 Mathematical Formulation of Viscoelastic Model

According to Taylor et al., three-element viscoelastic models are the simplest ones to generate the creep and stress relaxation responses for soft tissue characterization [82]. This section will discuss the development of a three-element viscoelastic model using a mathematical analog composed of springs and a dashpot. Figure 4.1 presents a standard linear solid model, also called a three-element Maxwell-Wiechert model [83]. In figure 4.1, the linear spring constants are E_1 and E_3 respectively, while the linear dashpot constant is η_1 . The constitutive equations for the springs and dashpot are presented in equation 4.1

¹The testing procedures were approved prior to conducting the experiments by The University of Texas at Arlington IRB with protocol number 2023 – 0306

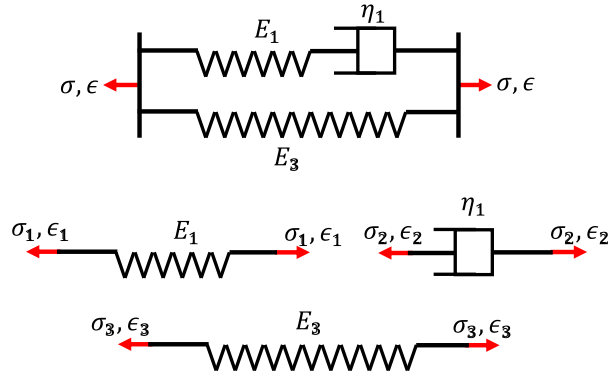


Figure 4.1: Three element Maxwell Wiechert model with free body diagram [47]

$$\sigma_1 = E_1 \epsilon_1$$

$$\sigma_2 = \eta_1 \dot{\epsilon}_2$$

$$\sigma_3 = E_3 \epsilon_3 \quad (4.1)$$

In equation 4.1, σ_1 and ϵ_1 , σ_2 and ϵ_2 , σ_3 and ϵ_3 are the stresses and strains experienced by spring element labeled E_1 , dashpot element labeled η_1 and spring element labeled E_3 respectively. The constraint equations for the entire model are presented in equation 4.2, while for the Maxwell arm is presented in equation 4.3.

$$\sigma = \sigma_1 + \sigma_3 = \sigma_2 + \sigma_3$$

$$\epsilon = \epsilon_1 + \epsilon_2 = \epsilon_3 \quad (4.2)$$

$$\sigma_M = \sigma_1 = \sigma_2$$

$$\epsilon_M = \epsilon_1 + \epsilon_2 \quad (4.3)$$

In equation 4.2, σ and ϵ are the stress and strain experienced by the overall model. In equation 4.3, σ_M and ϵ_M are the stress and strain experienced by the Maxwell arm of the model. The

governing equation of the three-element Maxwell-Wiechert model is presented in equation 4.4 [83].

$$\sigma(t) + \frac{\eta_1}{E_1} \dot{\sigma}(t) = E_3 \epsilon(t) + \frac{\eta_1(E_1 + E_3)}{E_1} \dot{\epsilon}(t) \quad (4.4)$$

The relaxation response can be obtained by applying and holding an instantaneous strain. As such, when the strain is held constant at ϵ_0 , the relaxation response $E_r(t)$ can be obtained as a function of stress history $\sigma(t)$ and holding strain as given in equation 4.5. Since the relaxation response is recorded when the indenter is held at the desired depth, the strain rate $\dot{\epsilon}(t)$ in equation 4.4 vanishes to zero. The solution to obtain the stress relaxation response (E_r) is presented in equation 4.5 where, the spring constant E_3 (refer figure 4.1) contributes to the long-term modulus, the spring constant E_1 (refer figure 4.1) contributes to the steady state modulus, and the ratio of damping coefficient to spring constant of the Maxwell-arm η_1/E_1 contributes to the relaxation modulus. The effect of long-term modulus, steady state modulus and relaxation time will be investigated as they relate to tissue viscoelastic properties.

$$\begin{aligned} E_r(t) &= \frac{\sigma(t)}{\epsilon_0} \\ &= E_1 \exp\left(-\frac{t}{\eta_1/E_1}\right) + E_3 \end{aligned} \quad (4.5)$$

Viscoelastic properties of soft tissue can be identified by employing a model that can accurately predict tissue response while simultaneously maintaining a degree of mathematical simplicity for its implementation as well as its ability to represent the experimentally obtained load-time response. A model will be defined as a good representation if it meets the following conditions: (a) the constitutive equations of the chosen model should not be complex, enabling its practical use based on experimentally obtained data and (b) the solutions obtained based on this model should exhibit high degree of conformity with the experimental data, for instance with a coefficient of

determination $R^2 > 0.95$ [48]. Higher order models such as a five-element Maxwell-Wiechert, could be employed to analyze the dynamics over frequency ranges during tissue palpation [84]. Equation 4.5 can be further expanded to obtain a stress relaxation response for a five-element Maxwell-Wiechert model as presented in equation 4.6. However, considering the effect of palpation frequency is out of the scope of this research and as such tissue characterization will be performed using the three-element Maxwell-Wiechert model.

$$E_r(t) = E_1 \exp\left(-\frac{t}{\eta_1/E_1}\right) + E_3 \exp\left(-\frac{t}{\eta_3/E_3}\right) + E_5 \quad (4.6)$$

The relaxation response of the three element Maxwell-Wiechert model is formulated and presented in equation 4.7, where the force history of the tissue is $F_{model}(t)$, the peak less the residual force is given by $C_1 = (F_{peak} - F_{residual})$, the time needed for the tissue to relax to the residual force is represented by $\tau = \eta_1/E_1$, and $C_2 = F_{residual}$ is the residual force [85, 86, 40].

$$\begin{aligned} F_{model}(t) &= (F_{peak} - F_{residual}) \exp^{-t/\tau} + F_{residual} \\ &= C_1 \exp^{-t/\tau} + C_2 \end{aligned} \quad (4.7)$$

A nonlinear least square optimization over the empirically obtained relaxation data from the tissue response could be used to evaluate the corresponding force model coefficients (C_1, C_2, τ) according to equation 4.8.

$$\min_{C_1, C_2, \tau} \sum_{t_0}^t [F_{exp}(t) - F_{model}(t)]^2 \quad (4.8)$$

Determining the viscoelastic properties of tissue could be possible using the parameters $(C_1, C_2$ and $\tau)$ obtained from equation 4.8. A lower bound limit is implemented to avoid infeasible solutions such as a negative time constant τ . A multistart function is implemented with 50 random initial conditions to avoid obtaining solutions with local minima. The MATLAB™ code developed

to evaluate the viscoelastic coefficients based on experimentally obtained is presented in Appendix B.

The relaxation time constant is the parameter that quantifies the stiffness of the tissue. A larger relaxation time constant signifies a compliant tissue, while a smaller time constant signifies a stiffer tissue. The coefficients obtained in their initial postprocessed format (presented in equation 4.7) do not produce a form to quantify viscoelastic coefficients (tissue modulus). Consequently, additional postprocessing is required to obtain useful results. The peak and residual forces could be further postprocessed to obtain the long-term and short-term shear modulus of the tissue. For incompressible materials, equation 4.9 provides the isotropic elastic Hertzian contact for a spherical indentation formulation [87, 88, 46, 89].

$$\begin{aligned}
 F(t) &= \frac{4\sqrt{\rho}}{3} \frac{E(t)}{(1-\nu^2)} h^{3/2} \\
 &= \frac{8\sqrt{\rho}}{3} [2G(t)] h^{3/2}
 \end{aligned}
 \tag{4.9}$$

In equation 4.9, the reaction force $F(t)$ experienced by an incompressible viscoelastic material with elastic modulus $E(t)$, shear modulus $G(t)$, and Poisson ratio ν indented by a rigid sphere with radius ρ to depth h , could be used to obtain a solution to identify the long-term and short-term moduli. In existing literature on ex vivo animal tissue studies, a Poisson ratio of 0.5 has been a widely used approximation for incompressible biological materials, as such a similar value for the Poisson ratio is used in this research as well [89, 90, 91]. When the tissue experiences a step load, the relaxation response can be expressed as equation 4.9, where the shear relaxation modulus $G(t)$, and the load-relaxation solution $F(t)$ are time dependent quantities. The load-relaxation force response $F(t)$ can be solved for a three element Maxwell-Wiechert model as presented in equation 4.7. Subsequently, the material relaxation function has the form presented in equation

4.10.

$$G(t) = B_1 + B_2 \exp(-t/\tau) \quad (4.10)$$

The material relaxation coefficient could be obtained by analogy of the creep solution, to relate the fitting parameters, C_j (refer equation 4.7) to the material parameters B_j as function of the experimental controllable parameters of the maximum indentation depth h_{max} and the indenter diameter ρ as shown in equation 4.11.

$$B_j = \frac{C_j}{h_{max}^{3/2} \left(\frac{8\sqrt{\rho}}{3}\right)} \quad j = 1, 2$$

$$B_{inst} = \sum_{j=1}^n B_j \quad n = 2 \quad (4.11)$$

The instantaneous shear modulus B_{inst} is evaluated as a summation of the coefficients of the shear modulus (B_j) and along with the relaxation time constant τ could be used to assess the viscoelastic properties of soft tissue.

4.3 Current Technologies: Tissue Characterization

Zeng and Arthur developed a handheld ultrasound indentation system to assess the responses of forearm soft tissues [92]. They performed the test on three normal subjects, and applied six different strain rates ranging from 0.75 to 7.5mm/s. They evaluated effective Young's modulus and found it to be consistent for different strain rates. Their tests consisted of two different states, when the muscle was contracted and when it was not. The tissues became stiffer when muscles contracted with Young's modulus increasing from 14kPa to 58.8kPa with an increase in thickness. The study assumed a Poisson's ratio of 0.45. Ohsugi et al. conducted a study to assess the elastic and viscous properties of human upper arm using the indentation method [93]. The upper arms of healthy male subjects were indented up to 14mm and the force response due to

indentation was collected. They investigated the indentation location dependency and found that muscle properties remained relatively constant in the upper arm area. Pailler-Mattei et al. conducted research to measure the mechanical properties of human skin in vivo using an indentation test [94]. Their investigation included indentation depths ranging from 0.8 to 4.4mm. The study used different mechanical models namely Bec/Tonck, Song/Parr, and Perriot/Barthel to assess the impact of subcutaneous layers on measurements and to extract the elastic properties of skin from overall mechanical response. Moreover, the study revealed that the variation in the measured Young's modulus at low indentation depths cannot be adequately described by conventional one layer mechanical models, and an average Young's modulus was evaluated to be in the range of 4.5 to 8.0kPa. Su et al. characterized the mechanical behavior of human forearm soft tissue using a combination of traditional indentation tests and MRI techniques [95]. One of the important steps in Su's research included investigating the viscoelastic response of the forearm through a series of indentations (3.21, 3.91, 4.80, and 5.46mm) at different loading rates (1, 3, and 6mm/s). The research emphasized the need to develop more accurate material parameters to capture the viscoelastic properties of soft tissue. Ahn et al. characterized the mechanical behavior of soft tissues ex vivo, specifically porcine livers, to develop a physical model for medical simulations [96]. They focused the research as it relates to the shape of the indenter tip (flat and hemisphere). The measurements included surface deformation and force responses obtained through a three-dimensional optical system and a force transducer. The study recognized the challenges in accurately characterizing soft tissues with large deformations due to the complexity of experimental setups and the use of optical systems to measure reaction forces. The research presented the need for further progress in soft tissue characterization, including the development of experimental protocols and devices to precisely measure indenter-tissue interactions, as well as the validation of reaction forces and

deformation predictions. Baroudi et al. collected and analyzed data from 117 patients with forearm soft tissue sarcomas to investigate the characteristics and oncologic outcomes of surgical treatment [97]. The results indicated favorable local control and survival outcomes, particularly for those patients with less aggressive tumor characteristics, such as grade 1–tumors and small tumor sizes ($\leq 5\text{cm}$). Eberhart et al. and Wang et al. reviewed the biomechanical properties of human vaginal wall particularly in the context of pelvic organ prolapse [98, 86]. Their work supports the notion of conducting non-invasive procedures to assess the biomechanical behavior of anterior vaginal wall as a means of disease prognosis. Wang et al. investigated the effect of indentation angle and indentation rate on anterior vaginal wall in 23 women (9 controlled and 14 diagnosed with pelvic organ prolapse). The results demonstrated that the properties of anterior vaginal wall tissue in prolapsed and non-prolapsed women can be quantitatively measured and characterized using a force sensor. Park et al. presented an indentation based device for measuring tissue mechanical properties designed using off-the-shelf and 3D-printed parts with an overall diameter 15mm [99]. They evaluated the viscoelastic properties of human forearm with one male and one female participants. The instantaneous shear modulus of male and female subjects ranged from 1.7 to 3.5kPa whereas the relaxation time ranged from 4.6 to 12.4s respectively. According to Park, the female skin generally exhibited higher instantaneous shear moduli and relaxation times compared to males. Park et al. also focused on assessing the effect of age on the biomechanical properties. The results indicated that aging brings about significant changes in the viscoelastic properties and the relaxation time of the skin. Park et al. conducted research focused on characterizing the mechanical properties of human melanoma tissue and compared them with normal tissue properties [99, 100, 101]. They found that melanoma tissue exhibited an elevated shear modulus and reduced tissue relaxation time compared to normal tissue. This research developed a strong foundation to

identify a link between tissue mechanics and disease progression.

These studies collectively emphasized the importance of considering multiple factors in evaluating soft tissue viscoelastic properties. These factors include indentation depth, strain rate, age, gender, race as well as underlying disease state of the tissue. Subsequently, to investigate the viscoelastic properties of forearm tissue, the recommended range of parameters include an indentation depth from 0.8 to 8mm and strain rates up to 4mm/s. In addition to the recommended parameters and identifying the effects due to indentation depth, strain rate, age, race and gender, this dissertation will also track if the participant were performing any strength exercise (especially forearm). Further discussion is provided in section 4.5.1.

4.4 Manual Characterization Setup- Results and Discussion

The results from initial sensor characterization experiments demonstrated desirable performance of the sensor as it relates to the accuracy, sensitivity, resolution, repeatability and precision. Figure 4.2 shows the sensor mounted on the in vivo test platform. The experimental setup developed and presented in figure 4.2 was used to indent the forearm tissue to a predefined indentation and obtain in vivo tissue relaxation data.

Figure 4.2 shows a stationary base on which the forearm is placed. The setup is developed to manually indent (resolution 0.254mm) the forearm with a desired indentation depth but not indentation rate and measure the tissue relaxation data. The total length of the forearm was measured and the location for indentation was set to 57% away from the distal region of the fist [102]. The reason for selecting this location is that it induces less discomfort for the volunteer undergoing the test. Additionally, the human forearm has minimal influence on the sensor response data due to

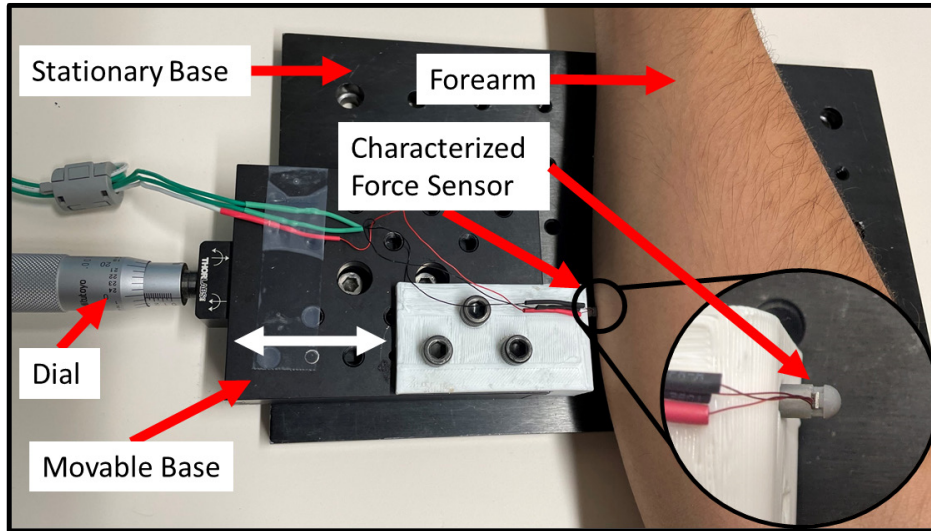


Figure 4.2: Testbed for evaluation of in vivo forearm tissue relaxation response

the body's numerous natural motions, thus making the data-capturing procedure relatively easier. When the forearm rests on the stationary base, the movable base was translated to just engage with the forearm tissue and this position was considered as the starting position for the indentation test. The sensor measurements were initiated at this stage and the movable base was translated to an indentation depth of 6.3mm using the micrometer dial. The forearm and sensor position were maintained stationary as the test progressed and the stress relaxation response was captured. During the tissue relaxation phase, the sensor recorded resistance (from the strain gauge attached and characterized micro-force sensor) to be used to quantitatively characterize the viscoelastic properties of the forearm tissue. The resistance data recorded from the sensor was postprocessed to analyze the viscoelastic properties using a three element Maxwell-Wiechert model. The sensor reaction force was estimated by rearranging the calibration equation established from figure 3.3 to obtain $F = \gamma_b/738.64$ (Please note: when this tissue characterization setup was being evaluated, the sensor yielding a calibration coefficient of $738.64\mu\epsilon/N$ was used. The calibration factor was updated each time a new sensor head was assembled). The existing setup does not provide means

to generate a constant strain rate (indentation rate) due to manual rotation the dial gauge. Consequently, the effects of constant strain rate on the viscoelastic coefficients could not be investigated. The existing setup was modified to allow for the generation of a constant strain rate. The tissue relaxation data obtained from in vivo measurements further build confidence in the development of an automated testing platform and its application to evaluate the soft tissue biomechanical properties.

4.4.1 Results and Discussion

This section will present the outcomes of the investigation to characterize the viscoelastic properties of soft tissue on the human forearm. Figure 4.3 presents a representative sample sensor response due to controlled indentation on the forearm using the manual test-bed. After manually positioning the sensor to a depth of 6.3mm the position of the forearm and the sensor were held fixed to allow the tissue to relax. The tissue reaction force experienced by the micro-force sensor was recorded by measuring and processing the strain gauge resistance in real time. The peak force was found to be 0.76N . The inset in figure 4.3 presents the tissue relaxation response, where the peak force experienced by the tissue was selected as the initial condition and the time was reset to 0s . The time series tissue force relaxation data was postprocessed to evaluate the coefficients of a three element Maxwell-Wiechert (refer equation 4.7 and 4.8). The analysis of the trimmed data estimated peak and residual forces of 0.76N and 0.61N respectively and a viscoelastic time constant $\tau = 12.4\text{s}$. The preliminary results from the manual characterization setup provided confidence to continue the investigation using automated control of the input parameters indentation depth and indentation rate.

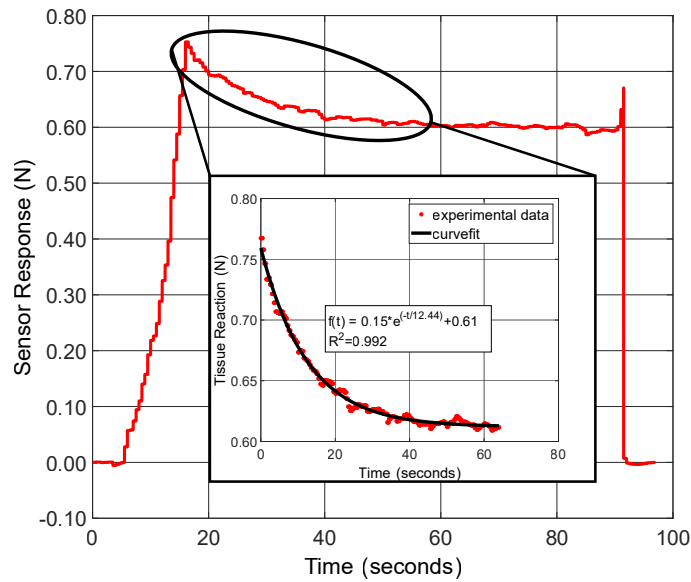


Figure 4.3: Representative sensor response due to indentation of forearm tissue with the inset showing the tissue relaxation response characterization equation

4.5 Automated Characterization Setup, Results and Discussion

The manual indentation experimental setup was modified because of its limitation relating to the ability to apply controlled strain rates. As such, a software-controlled motorized test-bed with a linear actuator was developed as shown in figure 4.4. This test-bed could also be used to perform repeatable tissue characterization experiments on a wide range of human participants. The tissue characterization test-bed uses a high accuracy ($\pm 2\mu m$) servo motor with encoder feedback driving a translational stage (Model: *MM4M – EX*, National Aperture, Inc., Salem, NH). The micro-force sensor was mounted on the translational stage using a 3D printed fixture. A base plate assembly was designed such that the mid ulnar region of the forearm of the participant aligns with the central axis of the micro-force sensor. A holt was provided for participant comfort and for obtaining repeatable data.

The tissue characterization experiments commenced with initially positioning the forearm to

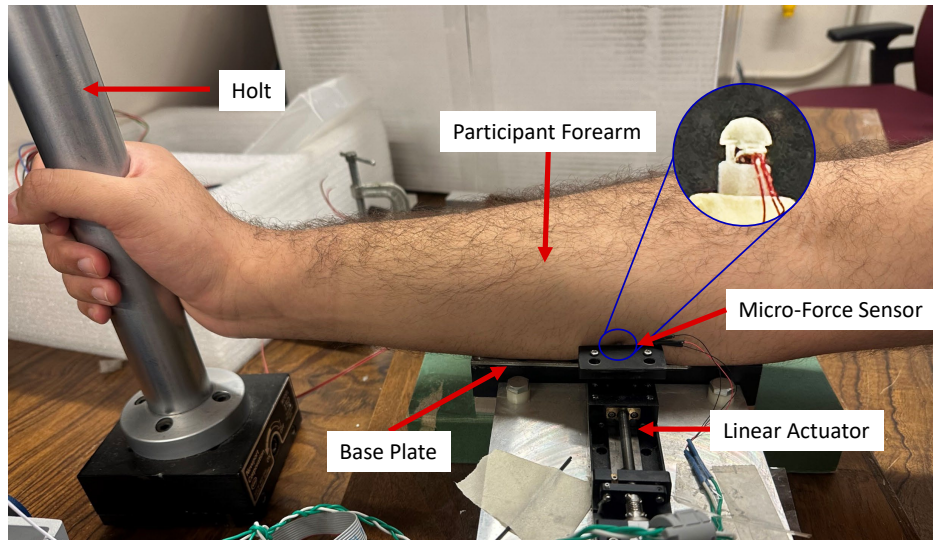


Figure 4.4: Testbed for in vivo human forearm tissue characterization with linear actuator

touch the sensor head such that the tissue experiences a pre-load up to $0.09N$ and the forearm was held at the same position throughout the indentation and relaxation experiment. The actuator initiated the indentation with the prescribed strain rate until reaching the desired indentation depth. While doing so, a number of quantities to be used for tissue characterization experiments were acquired through a data acquisition setup and saved on the computer running the control software NI LabVIEW™. A NI-9219 DAQ module was programmed to collect data at $100Hz$. The digital data collected and saved were the time step, position of linear actuator, resistance of the strain gauge attached micro-force sensor and the calibrated real-time force response.

A sample profile of the linear actuator motion characteristic is presented in figure 4.5. The slope of the graph represents the programmed strain rate, the height of the graph represents the indentation depth whereas the length of the horizontal line represents the hold time at the desired indentation depth. The tissue relaxation response is monitored during the hold time. The algorithm developed and implemented in NI LabVIEW™ for the translation of the linear actuator with the desired velocity up to a desired indentation depth is provided in Appendix C.

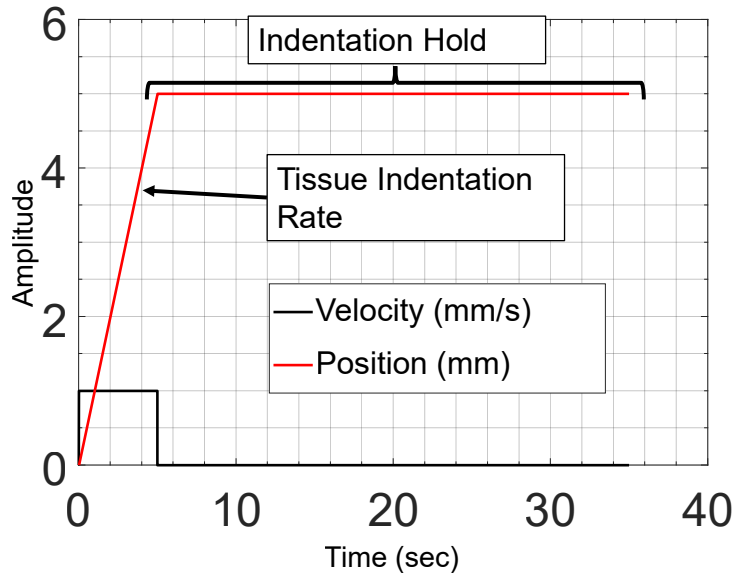


Figure 4.5: Representative actuator position and velocity profiles with a desired indentation rate of 1mm/s and indentation depth of 5mm

The relationship between strain rate and indentation depth with respect to time can be obtained using the approach suggested by Qian et al. [103]. The strain rate $\dot{\gamma}$ is expressed as given in equation 4.12.

$$\dot{\gamma} = \frac{2\kappa\delta}{\pi\rho t} \quad (4.12)$$

where, κ is a correction factor to account for the effect of tissue thickness and size of indenter radius, δ is the indentation depth, ρ is the indenter radius, and t is the indentation time. The correction factor κ can be evaluated for a spherical indenter geometry following the procedure described by Hayes et al. [104].

4.5.1 Process Parameters Effects on Viscoelastic Constants

This section will provide further insight over the process control parameters to be investigated to characterize the biomechanical properties of soft tissue. To comprehensively assess the viscoelastic

properties of soft tissue, it is imperative to consider a range of essential process parameters and understand their effects. These parameters encompass factors such as indentation depth, strain rate, and demographics (age, race, gender). Investigating the effects of these parameters will aid in understanding the fundamental time-dependent mechanical behavior of soft tissue under varying conditions. This section discusses the development of a framework to investigate tissue viscoelastic properties for different participant characteristics. A process flow diagram is developed for the characterization experiments and is presented in figure 4.6.

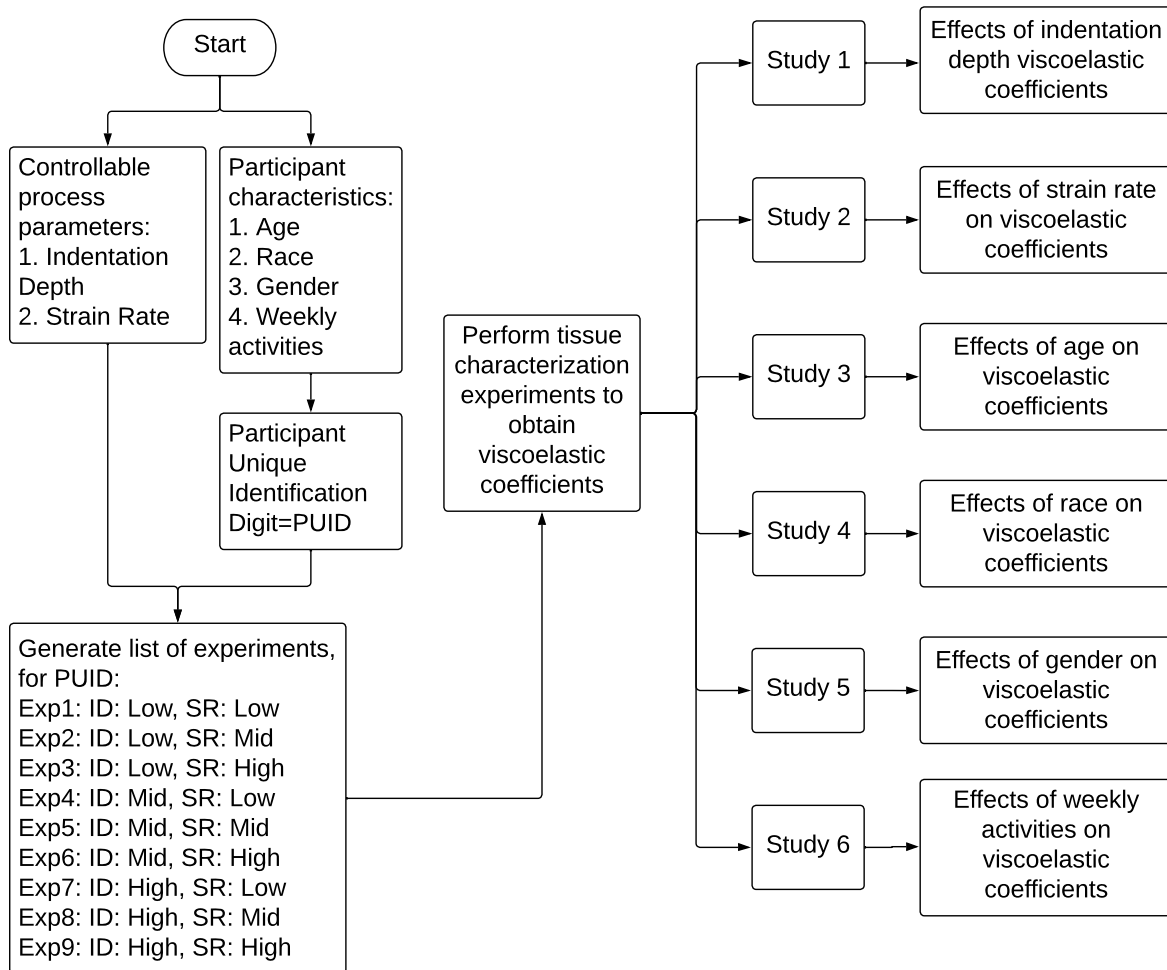


Figure 4.6: Process flow diagram to perform indentation experiments and proposed outcomes

The indentation depth is an important factor in characterizing viscoelastic properties and is

considered in this research [93, 94, 95, 96]. Varying levels of penetration into soft tissue reveal its response to mechanical deformation thus offering insight into the stiffness characteristics of the tissue [86, 94, 95, 96]. The strain rate is also an important parameter for assessing the viscoelastic response of soft tissue. Research conducted by Johnson et al. quantified the in vitro mechanical properties of the gallbladder, bladder and intestine tissues of human and porcine hosts by using a uniaxial testing machine [105]. They found a substantial dependence on the loading rate during the characterization studies. According to the research conducted by Qian et al., the viscoelastic properties of the tissue are directly dependent on the strain rate, and that very limited research exists to quantitatively characterize the viscoelastic properties of a tissue in vivo as they relate to the diameter of the indenter, depth of indentation and strain rate [103]. However, they were not able to characterize the effect of strain rate over the tissue properties using in vivo indentation due to the design of their sensing system [103]. The recommended actuator velocities for indentation tests on soft tissues are in the range of 0.75 to 4.0mm/s for forearm tissue [95, 106, 107, 108]. The other controllable process parameter is strain rate (please refer figure 4.6).

The demographics of an individual could introduce variations in soft tissue properties. The effect of demographics on the viscoelastic coefficients as they relate to an individual's age, race, gender could be investigated and as such they are recorded for recruited participant. Each participant was assigned a unique identification digit (PUID) which can be later retrieved for postprocessing. A set of nine experiments were conducted using permutations and combinations of three levels of indentation depth and strain rate for each participant. The three element Maxwell-Wiechert model was implemented to evaluate the coefficients of the viscoelastic model as representative soft tissue properties for an individual experiment using equation 4.10 under controlled indentation depth and rate. Subsequently, the effects of controllable process parameters and participant characteristics on

viscoelastic coefficients will be presented and discussed.

Figure 4.7 shows a representative postprocessing algorithm designed to evaluate viscoelastic properties from the experimentally acquired tissue response information. According to figure 4.7, experiment number 1 was conducted using indentation depth $4mm$ (low) and strain rate $1.5mm/s$ (low) on a 20 year old male Asian participant. The calibrated force sensor measured the resistance in real-time. The measured resistance-time history was then postprocessed to obtain an equivalent force relaxation-time history. The peak force from this individual experiment was manually selected and an overall response for $40s$ from the peak force time instance was analyzed. The analysis resulted in obtaining the coefficients C_i and B_{inst} , and time constant τ as presented in equation 4.8 and 4.11.

4.5.2 Results and Discussion of Viscoelastic Properties of Tissue

The results from the manual characterization provided confidence in continuing the investigation to build an automated characterization test-bed to conduct tissue characterization experiments on a larger subset of population to study the effects of process parameters and demographics. The tissue characterization experiments were conducted on 30+ participants using the automated test-bed shown in figure 4.4. Table 4.1 presents different levels for each process parameters (controllable process parameters and participants characteristics) as such the results for 30 participants will be presented using these levels. The controllable process parameters were chosen from the assigned range obtained from literature review, where the low, medium and high indentation depth was categorized as 4, 5, and $6mm$, while the low, medium and high strain rate was classified as 1.5, 2.5, and $3.5mm/s$ respectively. The age of the participants was classified in 10-year span. While

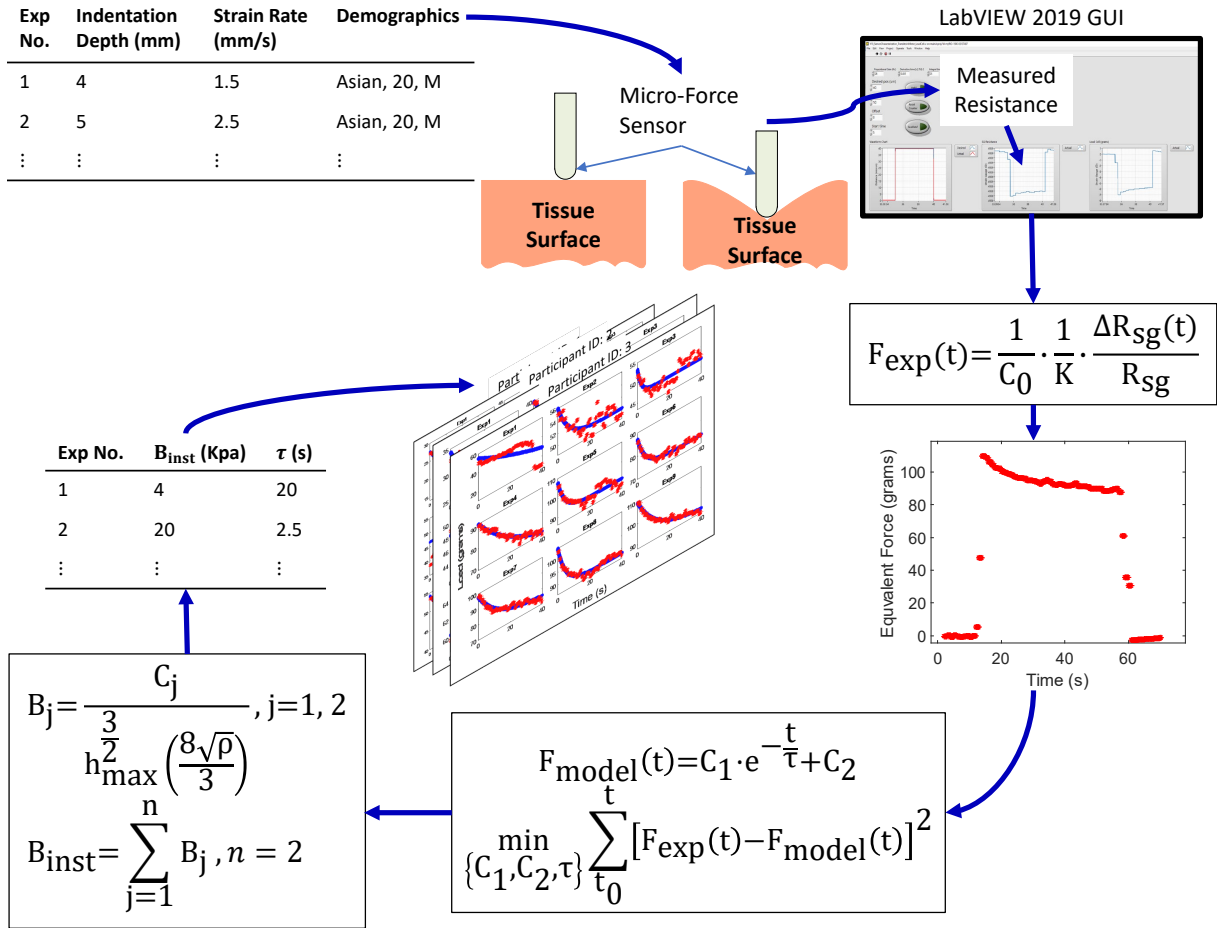


Figure 4.7: Representative process flow diagram, presenting tissue indentation performed on selected experiment followed by postprocessing to obtain viscoelastic properties of soft tissue of a participant

the race was categorized as Asian, Caucasian, and Others. The gender was classified as the birth gender of the participant as either male or female. If the participant was engaged in arm strength exercise, the factor was categorized as yes or no.

4.5.3 Effect of Indentation Depth

In this section the effect of indentation depth on the viscoelastic properties of soft tissue is presented by generating a box and whisker plot as shown in figure 4.8. The instantaneous shear modulus B_{inst} (summation of long-term shear modulus B_1 and short-term shear modulus B_2) is

Table 4.1: Factors and levels investigated for tissue characterization

Factors	Indentation depth (mm)	Strain rate (mm/s)	Age	Race	Gender	Arm strength training
Levels	4	1.5	20-29 [14]	Asian [13]	Male [19]	Yes [10]
	5	2.5	30-39 [4]	Caucasian [11]	Female [8]	No [17]
	6	3.5	40-49 [4]	Others [3]		
			50-59 [2]			
			60-69 [2]			
			70-79 [1]			

[XX]= Group Sample Size

discussed. The effect on the time constant τ is also discussed and presented in figure 4.8.

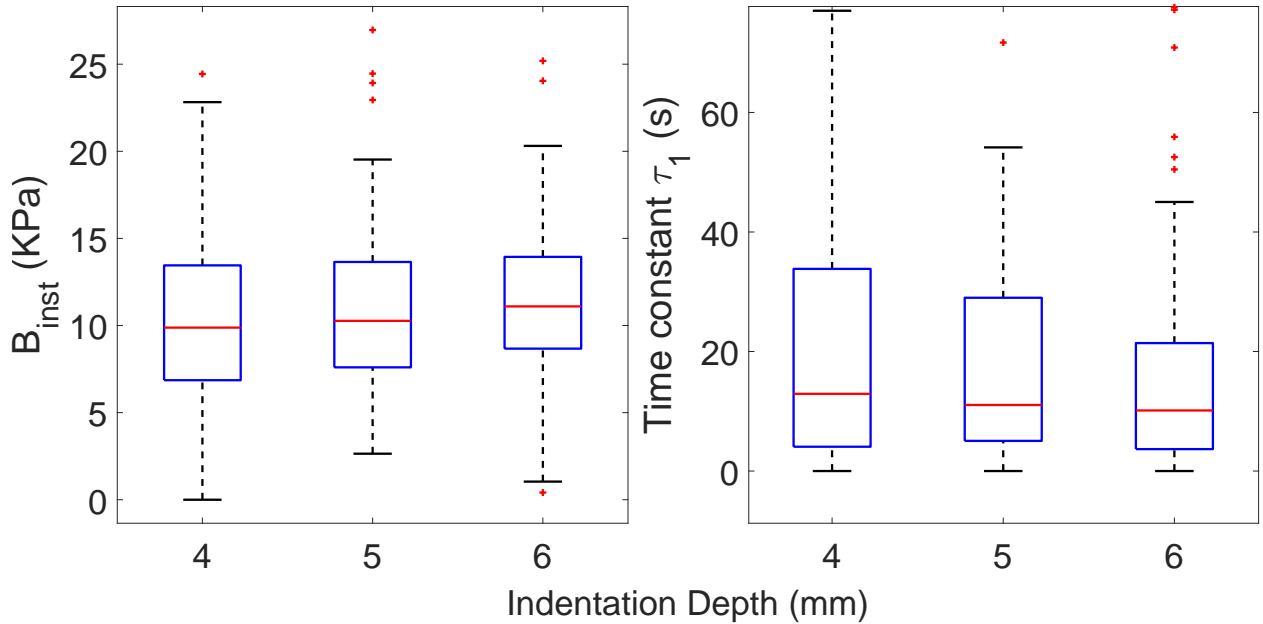


Figure 4.8: Instantaneous shear modulus and time constant as a function of indentation depth for all strain rates for the forearm for the 30 participants

The analysis of instantaneous shear modulus at different indentation depths revealed notable differences. For a $4mm$ indentation depth, the range of shear modulus values spanned from 0 to $22.8kPa$ with a median value at $9.8kPa$. When the indentation depth was increased to $5mm$, the instantaneous shear modulus range spanned from 2.6 to $19.5kPa$ with a median shear modulus at $10.2kPa$. For a $6mm$ indentation depth, the range extended from 0 to $20.3kPa$ with a median

value at $11kPa$. These results indicate that as the indentation depth increased, the median shear modulus increased too. A shear modulus representing $0kPa$ indicates that the material behaves entirely like a fluid, displaying no tendency to return to its original shape when applied forces are released. This implies that the participant disengaged their forearm from the characterization setup.

The analysis of time constant parameter also demonstrated noteworthy trends. At a $4mm$ indentation depth, the time constant exhibited a range of 0 to $77s$ with a median at $13s$. For a $5mm$ indentation depth, the range was 0 to $54s$ with a median at $11s$. When the indentation depth increased to $6mm$, the range span further decreased from 0 to $45s$ with a median at $10s$. As the indentation depth increased, the maximum value of time constant reduced, indicating less variability in the tissue relaxation behavior, indicating a relatively faster relaxation time and thus a stiffer tissue.

4.5.4 Effect of Strain Rate

In this section the effect of strain rate on the viscoelastic properties of soft tissue is presented. To investigate the effects of strain rate on the viscoelastic properties across the 27 volunteers, a box and whisker plot is generated as presented in figure 4.9. The analysis of instantaneous shear modulus at varying strain rates demonstrates notable differences. For a strain rate of $1.5mm/s$ the range of instantaneous shear modulus spanned from 0 to $22kPa$ with a median at $9.8kPa$. When the strain rate increases to $2.5mm/s$ the range extends from 0 to $20.9kPa$ with a median at $10.3kPa$. When the strain rate was further increased to $3.5mm/s$, the range varied from 1.6 to $20.3kPa$ with a median at $10.5kPa$. It is concluded that the range for instantaneous shear modulus

reduces as the strain rate increased while the median itself increased as the strain rate increased.

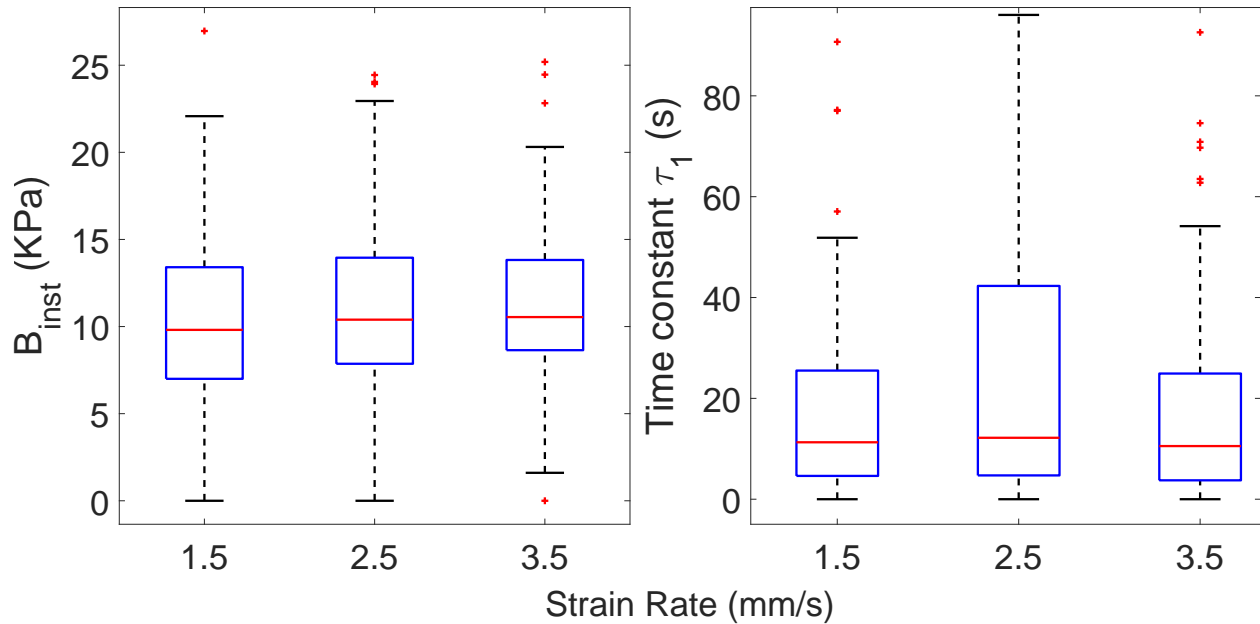


Figure 4.9: Instantaneous shear modulus and time constant for different strain rates for all depths applied on the forearm tissue for the 30 participants

The analysis of the time constant parameter also revealed significant trends. At a strain rate of 1.5mm/s , the time constant exhibits a range of 0 to 51s with a median at 11s . For a strain rate of 2.5mm/s , the time constant extends from 0 to 96s with a median time constant at 12s . Further increasing the strain rate to 3.5mm/s caused the span to drop from 0 to 54s with a median at 10s . Relatively low variations in instantaneous shear modulus and time constant were observed for the fastest strain rate.

4.5.5 High-Indentation Depth and Strain Rate

Since low variation in instantaneous shear modulus and relaxation time was observed due to high indentation depth and strain rate the responses from all nine experiments were investigated for each participants. Figure 4.10 presents a grid of sample raw data collected for nine experiments for a single volunteer with three indentation depths and three strain rates. As the indentation depth

increased the tissue reaction force increased as well. However no discernible effects were observed due to changes in strain rate. It is evident from figure 4.10 that experiments labeled as 3, 4, 5 did not exhibit stress relaxation behavior, instead the tissue reaction force increased with time. A similar pattern of increased force over time during the hold period was observed for other participants for experiments labeled 1, 2, 3, 4, 5.

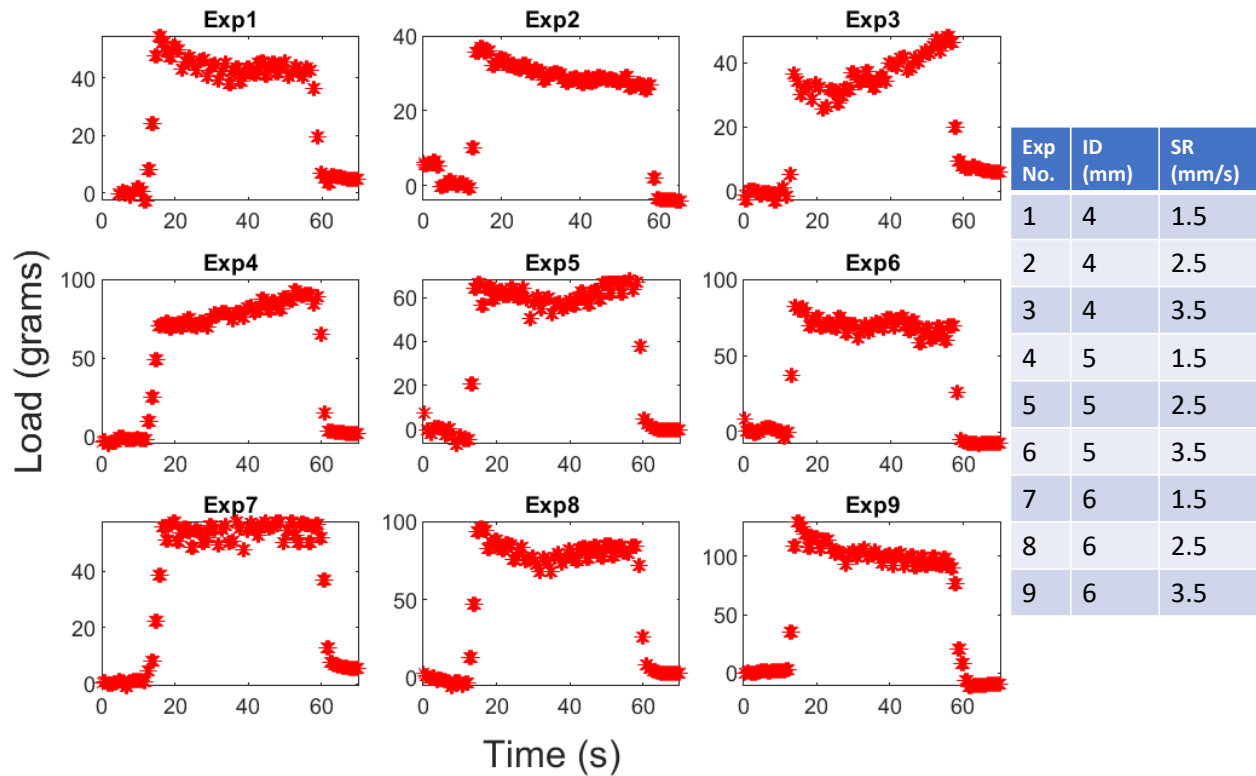


Figure 4.10: Tissue characterization experimental response of a participant for low, medium and high indentation depths and strain rates. (Note: ID is the indentation depth and SR is the strain rate)

Moreover, this characteristic behavior was prominent especially when experiments were conducted at low and medium indentation depths and at low and medium strain rates. It is worth noting that experiment 9 which is characterized by the greatest indentation depth ($6mm$) and fastest strain rate ($3.5mm/s$) consistently demonstrated a typical stress relaxation response across all participants (except for 3 outliers). As such, further investigation was performed with data collected by

using the maximum indentation and fastest strain rate only.

4.5.6 Effect of Age

This section will discuss the effect of age when the soft tissue was subjected to an indentation depth of 6mm and a strain rate of 3.5mm/s . The effect of age on the instantaneous shear modulus and the time constant were investigated using a scatter plot and, a box and whiskers plot as presented in figure 4.11(a, b) and (c, d) respectively.

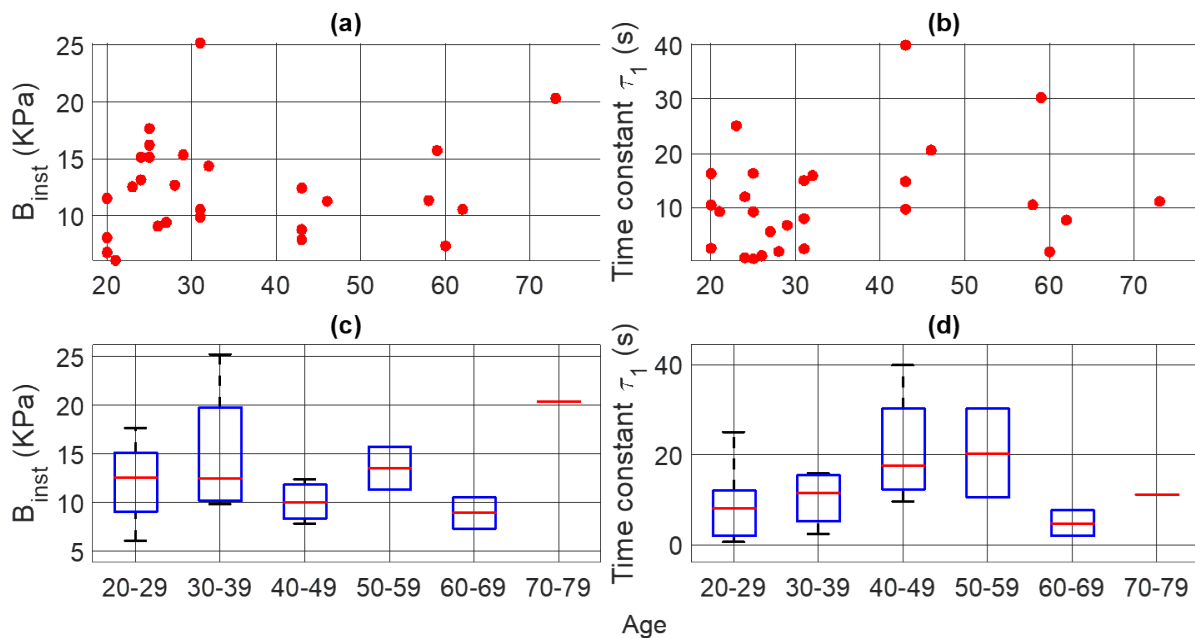


Figure 4.11: Effect of age on the viscoelastic properties of soft tissue

According to the plot in figure 4.11(a), the instantaneous shear modulus is within a band from 0 to 20kPa for all age groups investigated. The instantaneous shear modulus decreased with increasing age from 20 to 49 year old. Lee et al. found that factors related to the aging process affect the decrease in the instantaneous shear modulus leading to more compliant tissue for elder populations [109]. It can be inferred from figure 4.11(b) that the time constant is in a band from 0 to 20s with some outliers extending beyond 20s . The box and whiskers graph (figure 4.11(c))

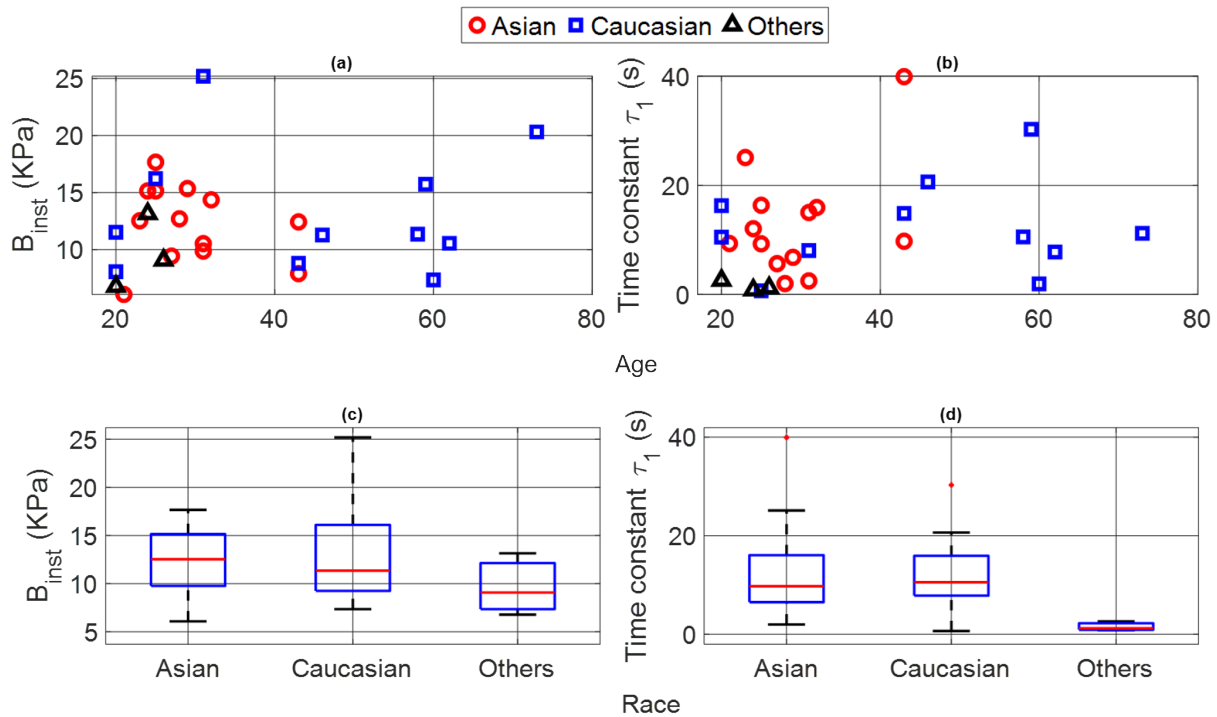
presents variations across age groups; the instantaneous shear modulus remains relatively constant for those between 20 and 70 years. The time constant for younger subjects (20 – 29) was evaluated to be 8s and kept on increasing to 11, 18, and 20s for participants in the age groups of 30 – 39, 40 – 49 and 50 – 59 years respectively. This behavior could be associated with aging tissue properties where the tissue becomes more compliant and takes longer to relax and return to its original state similar to findings by Lee et al. [109].

4.5.7 Effect of Race

This section will present the effect of race on the viscoelastic properties of soft tissue for an indentation depth of 6mm and a strain rate of 3.5mm/s. The discussion is limited to 27 out of 30 participants excluding the outliers. Figure 4.12(a) and (b) presents the scatter plot of the instantaneous shear modulus and time constant respectively across the participants grouped into three race categories Asian, Caucasian, and Others. There are no discernible trends in the instantaneous shear modulus or time constant as a function of race based on figure 4.12(a) and (b). A high number of participants were young Asian and a relatively high number of participants were elder Caucasian adults. As such, in order to draw meaningful conclusions, it is recommended to recruit more participants to attain more uniform racial demographics.

The box and whiskers plot (refer figure 4.12(c) and (d)) compliments the scatter plot by presenting a comprehensive view of the distribution of viscoelastic properties across the different racial categories. The median shear modulus for Asian, Caucasian, and Other participants were 12.5, 11.3, and 9kPa respectively. The median time constant across Asian and Caucasian populations was 10s. The range of time constant for individuals of other racial backgrounds was very

low (2s to 3s) compared to Asian (2 to 25s) and Caucasian (0.6 to 21s).



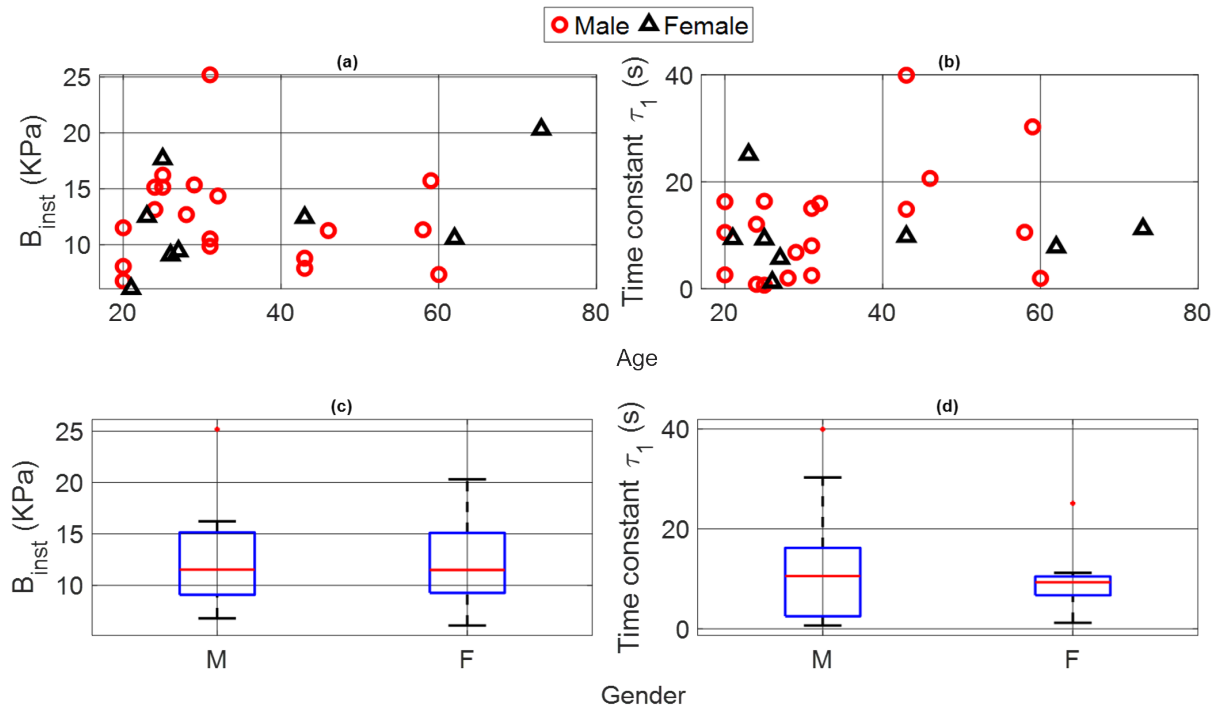


Figure 4.13: Effect of gender on the viscoelastic properties of soft tissue

modulus for the male participants spanned from 6.7 to 16.2kPa with the median at 11.5kPa while that for the female participants spanned from 6 to 20.3kPa with a median at 11.5kPa. The box and whiskers plot in figure 4.13(d) shows that the time constant for the male participants spanned from 0.6 to 30s with an outlier at 40s and median at 10s while that for the female participants spanned from 1 to 11s with an outlier at 25s and median at 9s. A lower time constant signifies that the relaxation response of the tissue is quicker which means that the tissue is stiffer.

4.5.9 Effect of Arm Strength Training

The effect of an individual performing arm strength training as opposed to those who were not on soft tissue properties for an indentation depth of 6mm and a strain rate of 3.5mm/s is discussed in this section. The scatter plot presented in figure 4.14(a) shows no significant difference in the instantaneous shear modulus among individuals who performed arm strength training and those

who did not. On the contrary, a noticeable difference is observed (figure 4.14(b)) for the time constant among individuals who performed arm strength training and those who do not, especially for the younger population.

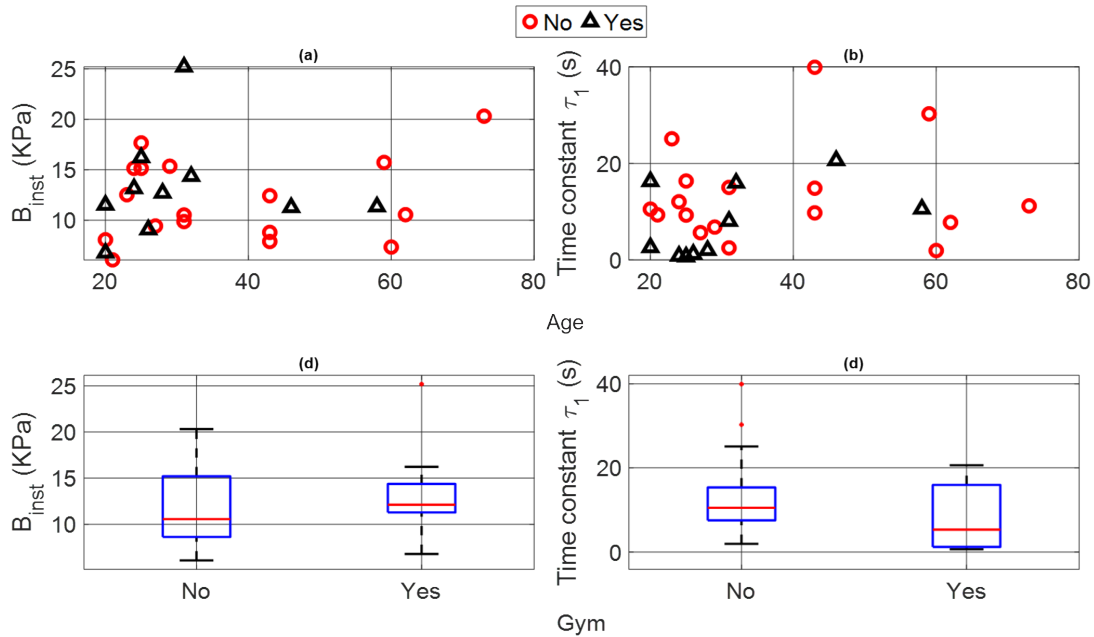


Figure 4.14: Effect of arm strength training on the viscoelastic properties of soft tissue

Figure 4.14(c) presents the box and whiskers plot for instantaneous shear modulus. For participants engaged in arm strength training, the median instantaneous shear modulus is $12.11kPa$ with a range from 6.7 to $16.2kPa$. In contrast, those who do not engage in arm strength training have a median instantaneous shear modulus of $10.5kPa$ with a broader range from 6.0 to $20.3kPa$. This indicates that arm strength training may be associated with a relatively higher shear modulus suggesting increased tissue stiffness.

Figure 4.14(d) presents the time constant for individuals categorized as engaged in arm strength training and those who are not. Participants who engaged in arm strength training exhibit a significantly lower median time constant of $5s$ with a range from 0.6 to $20s$. In contrast, the individuals who do not participate in arm strength training have a median time constant of $10s$ with a broader

range from 2 to 25s. This implies that participants associated with arm strength training have faster tissue relaxation particularly, the younger population. This means that individuals performing arm strength training have stiffer forearm tissue.

4.6 Summary of Tissue Characterization Results

The viscoelastic properties of soft tissues are affected by various factors. The factors investigated in this study were the indentation depth, strain rate, age, race, gender, and arm strength training. The instantaneous shear modulus and tissue relaxation time constant across all recruited participants is between $0kPa$ to $20kPa$ and $0s$ to $20s$ respectively (with some outliers). Age affects tissue properties with older individuals generally displaying a slower tissue relaxation response, which means that the tissue takes a longer time to return to its original state. No discernible trends in the instantaneous shear modulus and tissue relaxation time constant as a function of race were observed. The participants recruited during this research were skewed with young Asian, and elder Caucasian adults as such recruiting participants to attain more uniform racial demographics will assist in drawing more conclusive outcomes. No discernible differences were obtained in instantaneous shear modulus between the male and female population. However, with the current population sample size the females tend to have a relatively lower time constant (faster tissue relaxation response) signifying a relatively stiffer tissue. The participants recruited during this research were skewed with a larger number of male participants as opposed to female participants as such more females should be recruited in future studies. Arm strength training is associated with increased tissue stiffness and faster relaxation, particularly among younger individuals. Thus people engaged in arm strength training tend to have stiffer forearm tissue.

CHAPTER 5

CONCLUSIONS AND FUTURE DIRECTIONS

5.1 Conclusions

The aim of this dissertation was to develop a sensing system that could be outfitted at the tip of a micro-robot to aid in collecting palpated internal organ in vivo tissue relaxation forces. A uniaxial micro-force sensor was conceptualized considering a strain gauge-based technology; with sensor component features designed to be attached at the distal end of a hybrid-rigid continuum diagnostic robotic device for confined human spaces such as the bladder. The significance of this research arises from the limitations identified in the current technologies to quantitatively characterize the viscoelastic properties of soft tissue in the bladder through localized contact palpation methods to track disease progression. The sensing system was designed for the intended application of the confined space of the bladder while addressing the associated issues arising from accessing the bladder such as trauma and discomfort. Major contributions of this research include the conceptual design and optimization of the micro-force sensor, structural analysis, fabrication, functional prototyping and assembly, micro-force sensor performance characterization, and viscoelastic tissue characterization.

A sensing system design methodology was developed. The methodology was followed to establish the desired design specifications for the micro-force sensor, which included an overall diameter of $\leq 3.5mm$, an axial load bearing capacity of $1N$, a resolution of at least $20mN$, an accuracy of $\pm 30mN$ and a factor of safety of 3.5. The initial design concept of the micro-force

sensor presented in this research is composed of three major components; a sensor base, a sensing element, and a sensor head. The sensor head component was developed to interact with the tissue under investigation, the sensor base component was developed to be easily attachable to the micro-robot subsystem, and the sensing element was designed to sense the reaction forces during tissue palpation and interrogation. A miniature metal foil strain gauge was identified and its geometry and linear operating range ($\pm 3000\mu\epsilon$) were considered as driving parameters for the design of the sensing element. A design optimization problem was formulated and used to identify optimal values for the design parameters of the sensing element. An exhaustive search optimization process using FE-based analysis was implemented to evaluate the optimal values of the design parameters of the sensing element with a bend radius, bend angle, and thickness of $1.7mm$, 110° , and $0.3mm$ respectively. The cost of the objective function for the optimal design meeting all the desired design specifications and material and geometric constraints was $894.98\mu\epsilon$ with a factor of safety of 3.54.

Considering the results obtained from the design optimization, a $0.3mm$ thin aluminum sheet was used to fabricate the sensing element to the desired dimensions. The dimensions of the manufactured sensing element were measured to be $2.18mm$ bend radius, 104.9° bend angle, and $0.3mm$ thickness. FE analysis was performed using the fabricated dimensions yielding a cost of the objective function of $840.55\mu\epsilon$ with a factor of safety of 3.74. The inverted vat photopolymerization additive manufacturing methodology was used to prototype the sensor head and the sensor base components. A maximum absolute difference between desired and fabricated dimensions was measured to be $183\mu m$ for the sensor head diameter.

The fabricated micro-force sensor was characterized to evaluate its functionality and develop its performance matrix. An automated characterization setup was developed. The sensor perfor-

mance characteristics were found to be an accuracy of $\pm 28.6mN$, a precision of 87.22%, and a repeatability error of $\pm 0.025N$ ($\pm 3.13\%$). A custom software-controlled tissue characterization test bed was developed to acquire tissue relaxation responses from the sensor due to controlled indentation and strain rate.

A three element Maxwell-Wiechert model was developed to calculate tissue viscoelastic properties such as short-term shear modulus, long-term shear modulus, and relaxation time constant from acquired experimental data. The testing procedures were approved by the Institutional Review Board at The University of Texas at Arlington with protocol number 2023 – 0306. The controllable process parameters considered during tissue characterization experiments were the indentation depth (4, 5, and 6mm) and strain rate (1.5, 2.5, and 3.5mm/s). The recruited participants were classified according to their age, race, gender, and arm strength training. Meaningful data were obtained at the higher indentation depth (6mm) and strain rate (3.5mm/s) when the tests were performed on the forearm. The ranges of instantaneous shear modulus and tissue relaxation time constant were found to be from 0 to 20kPa and 0 to 20s respectively. The results indicate that the tissue becomes more compliant as a person ages. No discernable trends were identified for the viscoelastic properties of tissue as a function of race. When gender is considered, females exhibited relatively stiffer tissue. When arm strength training is analyzed, individuals associated with arm strength training had stiffer tissue.

5.2 Recommendations for Future Direction

The research presented in this dissertation provided promising results to employ the micro-force sensor to measure tissue relaxation response and evaluate the viscoelastic properties of soft tissue.

As such, one of the future directions could involve testing the performance of the sensor by enclosing it with a biocompatible sheath and studying its effect on the viscoelastic characterization of the tissue. Recruiting participants to evenly distribute the population sample size could help in drawing meaningful conclusions for viscoelastic characterization. Investigating the effects of biological factors such as body mass index, weight, height, and body-fat content of an individual on the viscoelastic properties of soft tissue. A machine-learning algorithm can be implemented as a tool to classify the viscoelastic properties of soft tissue as healthy or diseased, provided sufficient data is collected. The sensor could be employed to perform indentation tests at several locations on a targeted surface to create an area of influence map, which could provide information about the underlying viscoelastic properties and subsequently help to identify and localize abnormal surfaces. A future direction could potentially involve characterizing the entire system of a sensor-attached robot to palpate in an artificially developed confined space environment emulating the intended application of bladder tissue diagnosis.

APPENDIX A

A.1 Matlab snippet to post process and develop sensor characterization plots

```
clear all
close all
clc

Tst=10;          % Choose approximate start time closer to zero
% seconds and before loading cycle % (For eg: 20)
Tend=90;         % Choose approximate end time for loading
% cycle % (For eg: 155)
Mid=70;          % Choose approximate time just before loading
% cycle ends % (For eg: 150)
one_cycle=100;  % Choose approximate time for no_load+
% load stage only % (For eg: 160)
j=1;
fp=addpath("C:\Users\kumats\OneDrive - University of Texas at " + ...
    "Arlington\Shashank Weekly - Shiakolas Panos S files" + ...
    "\All_LabVIEW_Files\Characterization\Sensor_characterization" + ...
    "\Sensor-Characterization-raw09292022_Comprehensive");
for i=[3,4,5,6]
[New_T(:,j),New_E(:,j),New_R(:,j)]=...
    Exp_Parameters_Accuracy_Repeatability_Sensitivity...
    (i, Tst,Tend,Mid,one_cycle,fp,false);
j=j+1;
end
figure()
plot(New_T,New_E,'LineWidth',5)
grid on
xlabel('Time (seconds)')
ylabel('Strain (\mu\epsilon)')
yafs=35;
ax=gca;
ax.FontSize = yafs;
ax.GridAlpha =1;
legend('Exp-1','Exp-2','Exp-3','Exp-4')

% Calculate Precision
Precision=zeros(15,4); % Initialize precision matrix to
% total number of applied load and total number of experiments
for pi=1:15
nd=pi*100; % calculate precision to time defined as nd
% [100;200;300;400;500;600;700;800;900;1000;1100;1200;1305;1400;1500]
st=nd-20; % calculate precision from time
Time=reshape(New_T, [], 1);
E_st=find(abs(Time-st) < 0.01,1);
E_nd=find(abs(Time-nd) < 0.01,1);
```

```

E_mean=mean(New_E(E_st:E_nd,1:j-1));
Avgmsd=mean(mean(New_E(E_st:E_nd,1:j-1)));
Precision(pi, :)=(1-abs((E_mean-Avgmsd)/abs(Avgmsd)))*100;
end

%% Precision based of excel: 14_Sensor_Characterization
clearvars -except Precision
fp=addpath("C:\Users\kumats\OneDrive - University of Texas at Arlington\
    Shashank Weekly - Shiakolas Panos S files\All_Excel files");
excelFileName = '14_Sensor_Characterization_NEW_Assembly.xlsx';
[N T Res] = xlsread(excelFileName, '#1');
[N1 T1 Res1] = xlsread(excelFileName, 'Strain_Calc_#1');

% Exp1=N(19:33,1:9);
% Exp2=N(37:51,1:9);
Exp3=N(55:69,1:9);
Exp4=N(73:87,1:9);
Exp5=N(91:105,1:9);
Exp6=N(109:123,1:9);

% L=N1(1,2:16); % applied load in grams
L=N1(17:31,2); % Applied load in Newton
mean_S=N1(17:31,4)';

[p R]=polyfitZero(L,mean_S,1);
% [p R]=polyfit(L,mean_S,1);
R2=1 - (R.normr/norm(mean_S - mean(mean_S)))^2; %--> R^2 value for ...
% the curve fit
y_fit=polyval(p,L);

figure ()
yafs=35;
msize=15;
hold on
plot(Exp3(:,5).*0.0098,Exp3(:,9),'gs','MarkerSize', ...
    msize,'MarkerFacecolor','g','LineWidth',2);
plot(Exp4(:,5).*0.0098,Exp4(:,9),'kp','MarkerSize', ...
    msize,'MarkerFacecolor','k','LineWidth',2);
plot(Exp5(:,5).*0.0098,Exp5(:,9),'m^','MarkerSize', ...
    msize,'MarkerFacecolor','m','LineWidth',2);
plot(Exp6(:,5).*0.0098,Exp6(:,9),'cd','MarkerSize', ...
    msize,'MarkerFacecolor','c','LineWidth',2);
grid on
xlabel('Load(N)')

ylabel('\gamma_b (\mu\epsilon)')
ax=gca;
ax.FontSize = yafs;
ax.GridAlpha =1;
hold on

```

```

plot(L,y_fit,'--k','MarkerSize',30,'LineWidth',3)
% txt = sprintf('Strain (\mu\epsilon) = %.2f * Load
% (grams)+%.2f \n', p(1),p(2));
txt=['\gamma_b (\mu\epsilon) = ' num2str(p(1),'%0.2f') '* Load (N)'];
txt2=['R^2= ',num2str(R2,'%0.3f')];
str={txt,txt2};
dimen=[0.2,0.6,0.2,0.1];
a = annotation('textbox',dimen,'String',str,'FitBoxToText','on');
legend('Exp-1','Exp-2','Exp-3','Exp-4','Exp_{mean}')
a.BackgroundColor='w';
a.FontSize=25;
box on

clear all
clc
fp=addpath("C:\Users\kumats\OneDrive - University of Texas at " + ...
"Arlington\Shashank Weekly - Shiakolas Panos S files\All_Excel files");
excelFileName = '20_IEEE_Data_For_Plots.xlsx';
[N,~,raw] = xlsread(excelFileName,'Design_Optimization');

%% Define data from Excel
DesignPoint=N(1:end,1);
Raw_Stress=N(1:end,7);
Raw_FOS=N(1:end,8);
Max_top_strain=N(1:end,9);
Min_top_strain=N(1:end,10);
all_t=N(1:end,3);
all_BR=N(1:end,5);
all_theta=N(1:end,4);
all_FOS=N(1:end,8);

desiredFOS=3.5; % Desired FOS

objfun=abs(1e6.*Max_top_strain);

% Extract design with FOS >= 3.5
Fail_safe_Stress=Raw_Stress(Raw_FOS>=desiredFOS);
Fail_safe_DP=DesignPoint(Raw_FOS>=desiredFOS);
Fail_safe_obj=objfun(Raw_FOS>=desiredFOS);
% Extract design with thickness = 0.3
obj_t03=objfun(all_t==0.3);
DP_t03=DesignPoint(all_t==0.3);

%% Figure 5 Design Optimization Plot Raw Data
figure()
p1=plot(DesignPoint,objfun,'xk');
hold on
% plot(DesignPoint,objfun,'-k','MarkerSize',15,'LineWidth',2)
p2=plot(Fail_safe_DP,Fail_safe_obj,'or');
p3=plot(DP_t03,obj_t03,'db');
xlabel('Design Point Number')
ylabel('Objective Function (\mu \epsilon)')

```

```

legend('Objective function for each Design Point', ...
      'Design Points with N_f>3.50', 'Design Points with t=0.3mm')
plot_mod(p1)
plot_mod(p2)
plot_mod(p3)
dimen=[0.2,0.70,0.1,0.05];
str=[sprintf('Optimal Design \nR=1.7mm, \theta=110^\circ, t=0.3mm')];
a = annotation('textbox',dimen,'String',str,'FitBoxToText','on');
a.BackgroundColor='w';
a.FontSize=15;
str1=[sprintf('Fabricated Beam \nR=2.1mm, \theta=105^\circ, t=0.3mm ')];
a1 = annotation('textbox',dimen,'String',str1,'FitBoxToText','on');
a1.BackgroundColor='w';
a1.FontSize=15;

%% Figure 6 Effect of Bend radius on Obj Fun
thickness=0.3; % Choose thickness
br=0.2; % Bend Radius Lower limit
all_t=N(1:end-1,3);
all_BR=N(1:end-1,5);
all_theta=N(1:end-1,4);
Raw_FOS=N(1:end-1,8);
FS_FOS=Raw_FOS(all_t==thickness);
BR=all_BR(all_t==thickness);
theta=all_theta(all_t==thickness);
obj_BR_th=objfun(all_t==thickness);
figure()
p4=plot(theta(BR==br),obj_BR_th(BR==br),'xr','MarkerFaceColor','r');
hold on
p5=plot(theta(BR==br+0.5),obj_BR_th(BR==br+0.5), ...
      'ob','MarkerFaceColor','b');
p6=plot(theta(BR==br+1),obj_BR_th(BR==br+1),'sg', ...
      'MarkerFaceColor','g');
p7=plot(theta(BR==br+1.5),obj_BR_th(BR==br+1.5),'dk', ...
      'MarkerFaceColor','k');
p8=plot(theta(BR==br+2),obj_BR_th(BR==br+2),'^m', ...
      'MarkerFaceColor','m');
p9=plot(theta(BR==br+2.5),obj_BR_th(BR==br+2.5),'>c', ...
      'MarkerFaceColor','c');
p10=plot(theta(BR==br+3),obj_BR_th(BR==br+3),'<', 'Color', ...
      [1 0.5 0.5], 'MarkerFaceColor', [1 0.5 0.5]);
p11=plot(theta(BR==br+3.5),obj_BR_th(BR==br+3.5),'p', 'Color' ...
      , [0.5 0.25 1], 'MarkerFaceColor', [0.5 0.25 1]);
p12=plot(N(end,4),-N(end,9)*1e6,'+', 'Color', [0.75 0.2 0.75] ...
      , 'MarkerFaceColor', [0.75 0.2 0.75], 'LineWidth', 2);
p13=plot(theta(FS_FOS>=desiredFOS),obj_BR_th(FS_FOS>=desiredFOS) ...
      , 'o', 'Color', [0.63 0.23 0.02]);
p12_1=plot(N(end,4),-N(end,9)*1e6,'o', 'Color', [0.63 0.23 0.02]);
xlabel('\theta (deg)');
ylabel('Objective Function (\mu\epsilon)');
legend('R=0.2', 'R=0.7', 'R=1.2', 'R=1.7', 'R=2.2', 'R=2.7', 'R=3.2', 'R=3.7', ...
      'R_{fab}=2.18', 'N_f \geq 3.50');

plot_mod(p4)

```

```

plot_mod(p5)
plot_mod(p6)
plot_mod(p7)
plot_mod(p8)
plot_mod(p9)
plot_mod(p10)
plot_mod(p11)
plot_mod(p12)
plot_mod(p13)
plot_mod(p12_1)

%% Read Sensor Characterization Data-II
clear all
clc
E2 = '20_IEEE_Data_For_Plots.xlsx';
N2= readtable(E2,'Sheet','Strain_calc_All');

%% Figure 8 Sensitivity plot
displacement=N2.Var1(47:61);
dR=N2.Var4(47:61);

figure()
p14=plot(displacement,dR,'xk');
hold on
[const,R_nor]=lsqcurvefit(@pol_fit,[1 1],displacement,dR);
dR_fit=pol_fit(const,displacement);
p15=plot(displacement,dR_fit,'--k');
% Evaluate R squared
mean_dR=(1/length(dR))*(sum(dR));
SS_tot=sum((dR-mean_dR).^2);
R_sq=1-(R_nor)/(SS_tot);
dimen=[0.2,0.70,0.1,0.05];
str=sprintf(['\\DeltaR_{sg} = %.2e \\cdot \\Deltax^{2} + %.2e \\cdot' ...
' \\Deltax, \\n R^2=%.3f'],const(1),const(2),R_sq);
a = annotation('textbox',dimen,'String',str,'FitBoxToText','on');
a.BackgroundColor='w';
a.FontSize=15;

xlabel('Controlled displacement (\\mum)');
ylabel('\\Delta R_{sg} (\\Omega)');
legend('Micro-force sensor','Curve fit');
plot_mod(p14)
plot_mod(p15)

%% Figure 9 Sensitivity plot (Linear)
LC=N2.Var3(47:61);
S=N2.Var5(47:61);
S_fea=N2.Var16(47:61);

N3= readtable(E2,'Sheet','Sensitivity');
figure()
% p16=plot(LC,S,'ok');

```

```

p16_1=plot(N3.Loadcell,N3.Strain,'or');
hold on
p16_2=plot(N3.Loadcell_1,N3.Strain_1,'^b');
hold on
p16_3=plot(N3.Loadcell_2,N3.Strain_2,'hm');

[C2,R_nor1]=L_fit(LC,S,1);
hold on
dR_fit2=polyval(C2,LC);
p17=plot(LC,dR_fit2,'--k');
% Evaluate R squared
R2=1 - (R_nor1.normr/norm(S - mean(S)))^2; %--> R^2 value for the curve fit

p18=plot(LC,S_fea,'sk');
[C3,R_nor1]=L_fit(LC,S_fea,1);
S_fea_fit=polyval(C3,LC);
p17_1=plot(LC,S_fea_fit,'-k');

dimen=[0.3,0.70,0.1,0.05];
str=sprintf(['\\mu\\epsilon_{FEA} = %.3f \\cdot \\Delta F, ' ...
    '\\n\\mu\\epsilon_{exp} = %.3f \\cdot \\Delta F, \\nR^2=%.3f ' ] ...
    ,C3(1),C2(1),R2);
a = annotation('textbox',dimen,'String',str,'FitBoxToText','on');
a.BackgroundColor='w';
a.FontSize=15;

xlabel('Load Cell (N)');
ylabel('\\gamma_{sg} (\\mu\\epsilon)');
legend('Exp-1','Exp-2','Exp-3','Curve fit','FEA');
plot_mod(p16_1)
plot_mod(p16_2)
plot_mod(p16_3)
plot_mod(p17)
plot_mod(p17_1)
plot_mod(p18)

%% Hysteresis plot
mfs_L=N2.Var9(69:84);
mfs_UL=N2.Var10(69:84);
nd=[0;displacement];
figure()
p19=plot(nd,mfs_L,'sk');
hold on
p20=plot(nd,mfs_UL,'ok');

[mfs_CL,~]=lsqcurvefit(@pol_fit,[1 1],nd,mfs_L);
mfs_fit_L=pol_fit(mfs_CL,nd);
p21=plot(nd,mfs_fit_L,'-k');

[mfs_CUL,~]=lsqcurvefit(@pol_fit,[1 1],nd,mfs_UL);

mfs_fit_UL=pol_fit(mfs_CUL,nd);

```

```

p22=plot(nd,mfs_fit_UL,'-k');

p23=plot([nd(end) nd(end)],[mfs_fit_L(end) mfs_fit_UL(end)],'-k');

xlabel('Controlled displacement (\mum)')
ylabel('Micro-force sensor (N)')
legend('Loading','Unloading')

plot_mod(p19)
plot_mod(p20)
plot_mod(p21)
plot_mod(p22)
plot_mod(p23)

%% Performance Matrix

clear all
clc

one_cycle=82.6; % Choose approximate time for no_load+load...
% stage only % (For eg: 160)
mid=70;
end_time=one_cycle;
j=1;
calibration=[8.32;8.46;8.52];
fp=addpath("C:\Users\kumats\OneDrive - University of Texas at" + ...
    " Arlington\Shashank Weekly - Shiakolas Panos S files" + ...
    "\All_LabVIEW_Files\Characterization" + ...
    "\Sensor-Characterization-Motorized-raw-06022023");
for i=[4,5,6]
    dataname=sprintf('test_%d.lvm',i);
    data=load(dataname);
    T{:,j}=data(:,1);% Extract time series and reinitialize it to zero
    R{:,j}=data(:,4);% Extract raw resistance
    dR{:,j}=data(:,4)-data(1,4); % Extrarct change in resistance
    L{:,j}=data(:,3); % Extract Load cell (N)
    P{:,j}=data(:,2); % Extract Position data

    Res(j,1)=performace_post_process(i,one_cycle,mid,false,8.5);
    j=j+1;
clear dataname data
end
%% Precision Matrix just for Exp 4 5 and 6 ## Commet Hysteresis when...
% running this ##

% Use the following snippt to extract time values for each run by changing
% value of exp_no
%%%%%%%%%%%%%%%%%%%%%%%%%%%%%%%%%%%%%%%%%%%%%%%%%%%%%%%%%%%%%%%%%%%%%%%%
% exp_no=1;
% figure()
% plot(T{:,exp_no},L{:,exp_no})
% xlabel('Time (seconds)')

```

```

% ylabel('LoadCell (N)')
%%%%%%%%%%%%%%%%%%%%%%%%%%%%%%%%%%%%%%%%%%%%%%%%%%%%%%%%%%%%%%%%%%%%%%%%

T1=T(:,1);
L1=L(:,1);

Time_1_start=[982.76;410.36;573.56;0;164.86;328.25;492.25;1146.37;...
    246.16;737.26;82.72;901.36;1064.55;819.05;655.61];
Time_1_end=[1064.55;492.25;655.61;82.72;246.15;410.35;573.55;1229.10;...
    328.25;819.04;164.85;982.75;1146.36;901.35;737.26];
idx_R01=find(abs(R(:,1)-R(:,1))(1,1)<0.01);
MR1=mean(R(:,1)(idx_R01,1));
strain1=1e6.*dR(:,1)./(MR1*2.03);

SG1=0.0098.*strain1./calibration(1); % Load Sensed by SG in (N)

T2=T(:,2);
L2=L(:,2);

Time_2_start=[1068.28;248.26;493.48;658.19;0;986.98;821.79;1150.17;...
    739.98;83.28;904.38;411.68;575.28;329.28;165.58];
Time_2_end=[1150.17;329.28;575.27;739.98;83.28;1068.27;904.38;1232.11;...
    821.79;165.58;986.98;493.48;658.18;411.68;248.26];
idx_R02=find(abs(R(:,2)-R(:,2))(1,1)<0.01);
MR2=mean(R(:,2)(idx_R02,1));
strain2=1e6.*dR(:,2)./(MR2*2.03);

SG2=0.0098.*strain2./calibration(2); % Load Sensed by SG in (N)

T3=T(:,3);
L3=L(:,3);

Time_3_start=[905.23;330.13;247.52;164.72;1069.43;658.73;1151.72;...
    740.63;412.33;83.14;576.42;987.12;822.93;0;493.53];
Time_3_end=[987.12;412.33;330.13;247.52;1151.71;740.62;1233.61;822.92;...
    493.52;164.71;658.72;1069.42;905.12;83.14;576.42];
idx_R03=find(abs(R(:,3)-R(:,3))(1,1)<0.01);
MR3=mean(R(:,3)(idx_R03,1));
strain3=1e6.*dR(:,3)./(MR3*2.03);

SG3=0.0098.*strain3./calibration(3); % Load Sensed by SG in (N)

Time1=[];
Load1=[];
L_SG1=[];

```

```

Time2=[];
Load2=[];
L_SG2=[];

Time3=[];
Load3=[];
L_SG3=[];

for i=1: length(Time_1_start)
idx_s1=find(abs(Time_1_start(i)-T1)<0.01,1);
idx_e1=find(abs(Time_1_end(i)-T1)<0.01,1);

idx_s2=find(abs(Time_2_start(i)-T2)<0.01,1);
idx_e2=find(abs(Time_2_end(i)-T2)<0.01,1);

idx_s3=find(abs(Time_3_start(i)-T3)<0.01,1);
idx_e3=find(abs(Time_3_end(i)-T3)<0.01,1);

Load1=[Load1;L1(idx_s1:idx_e1)];
Time1=[Time1;linspace((i-1)*one_cycle+1,i*one_cycle,...
    length(T1(idx_s1:idx_e1)))'];
L_SG1=[L_SG1;SG1(idx_s1:idx_e1)];

Load2=[Load2;L2(idx_s2:idx_e2)];
Time2=[Time2;linspace((i-1)*one_cycle+1,i*one_cycle,...
    length(T2(idx_s2:idx_e2)))'];
L_SG2=[L_SG2;SG2(idx_s2:idx_e2)];

Load3=[Load3;L3(idx_s3:idx_e3)];
Time3=[Time3;linspace((i-1)*one_cycle+1,i*one_cycle,...
    length(T3(idx_s3:idx_e3)))'];
L_SG3=[L_SG3;SG3(idx_s3:idx_e3)];

i=i+1;
end

figure()
p1=plot(Time1,Load1,'r-');
hold on
p2=plot(Time2,Load2,'b-');
p3=plot(Time3,Load3,'k-');
xlabel('Time (seconds)')
ylabel('Load Cell (N)')
legend('Exp_1','Exp_2','Exp_3')

plot_mod(p1)
plot_mod(p2)
plot_mod(p3)

figure()

```

```

interval=100;
p4=plot(Time1(1:interval:end),L_SG1(1:interval:end),'ro');
hold on
p5=plot(Time2(1:interval:end),L_SG2(1:interval:end),'bx');
p6=plot(Time3(1:interval:end),L_SG3(1:interval:end),'ks');
xlabel('Time (seconds)')
ylabel('F_{mfs} (N)')
legend('Exp_1','Exp_2','Exp_3')
plot_mod(p4)
plot_mod(p5)
plot_mod(p6)

nd1=(1:1:length(Time_1_start))*one_cycle;
nd=nd1-10;
st=nd-20;

%% Calculate Precision Values
for i=1: length(Time_1_start)

E_st1(i)=find(abs(Time1-st(i)) < 0.01,1);
E_nd1(i)=find(abs(Time1-nd(i)) < 0.01,1);
E_mean1(i)=mean(L_SG1(E_st1(i):E_nd1(i)));
E_std1(i)=std(L_SG1(E_st1(i):E_nd1(i)));

E_mean1_LC(i)=mean(Load1(E_st1(i):E_nd1(i)));

E_st2(i)=find(abs(Time2-st(i)) < 0.01,1);
E_nd2(i)=find(abs(Time2-nd(i)) < 0.01,1);
E_mean2(i)=mean(L_SG2(E_st2(i):E_nd2(i)));
E_std2(i)=std(L_SG2(E_st2(i):E_nd2(i)));
E_mean2_LC(i)=mean(Load2(E_st2(i):E_nd2(i)));

E_st3(i)=find(abs(Time3-st(i)) < 0.01,1);
E_nd3(i)=find(abs(Time3-nd(i)) < 0.01,1);
E_mean3(i)=mean(L_SG3(E_st3(i):E_nd3(i)));
E_std3(i)=std(L_SG3(E_st3(i):E_nd3(i)));
E_mean3_LC(i)=mean(Load3(E_st3(i):E_nd3(i)));

Avgmsd(i)=mean([E_mean1(i);E_mean2(i);E_mean3(i)]);

Avgmsd_LC(i)=mean([E_mean1_LC(i);E_mean2_LC(i);E_mean3_LC(i)]);

Precision(i,1)=(1-abs((E_mean1(i)-Avgmsd(i)))/abs(Avgmsd(i)))*100;
Precision(i,2)=(1-abs((E_mean2(i)-Avgmsd(i)))/abs(Avgmsd(i)))*100;
Precision(i,3)=(1-abs((E_mean3(i)-Avgmsd(i)))/abs(Avgmsd(i)))*100;

Precision_LC(i,1)=(1-abs((E_mean1_LC(i)-Avgmsd_LC(i)))/...
abs(Avgmsd_LC(i)))*100;
Precision_LC(i,2)=(1-abs((E_mean2_LC(i)-Avgmsd_LC(i)))/...
abs(Avgmsd_LC(i)))*100;
Precision_LC(i,3)=(1-abs((E_mean3_LC(i)-Avgmsd_LC(i)))/...

```

```

    abs(Avgmsd_LC(i))*100;

end

%% Repeatability Graph
A=abs(E_mean1)-abs(E_mean2);
max_A=max(A);
err_A=abs(E_std1)-abs(E_std2);
B=abs(E_mean2)-abs(E_mean3);
max_B=max(B);
err_B=abs(E_std2)-abs(E_std3);
C=abs(E_mean1)-abs(E_mean3);
max_C=max(C);
err_C=abs(E_std1)-abs(E_std3);
All=[max_A;max_B;max_C];
max_all=max(All);
LC=[E_mean1_LC;E_mean2_LC;E_mean3_LC];
Load=abs(mean(LC,1));
figure()
p7=plot(Load,A,'bo',Load,B,'mx',Load,C,'rs');

hold on
errorbar(Load,A,err_A,'b','LineStyle','None','LineWidth',3)
errorbar(Load,B,err_B,'m','LineStyle','None','LineWidth',3)
errorbar(Load,C,err_C,'r','LineStyle','None','LineWidth',3)
yline(max_all,'k--','LineWidth',5)
yline(-max_all,'k--','LineWidth',5)
dimen=[0.4,0.20,0.1,0.05];
str1=[sprintf('Repeatability: \x00B1 0.025 N (3.13%)')];
a1 = annotation('textbox',dimen,'String',str1,'FitBoxToText','on');
xlabel('\DeltaF-Load cell (N)')
ylabel('\DeltaF_{mfs} (N)')
legend('(F_{exp1}-F_{exp2})','(F_{exp2}-F_{exp3})','(F_{exp1}-F_{exp3})')
a1.BackgroundColor='w';
a1.FontSize=15;
plot_mod(p7)

```

APPENDIX B

B.1 Matlab code to evaluate viscoelastic coefficients using three element Maxwell-Wiechert model

```
clear all
close all
clc

Parti_ID=115; % Participant ID
SH_R=3.3; % Sensor head diameter

% Get LabVIEW file directory
id=num2str(Parti_ID);
direc=['C:\Users\kumats\OneDrive - University of Texas at Arlington' ...
      '\IRB MicroForceSensor and HRI\Shashank IRB forms' ...
      '\0IRB 2023-0306_Data\Data\CollectedData\Test1\'];
str=[direc,id,'\'];
fp=fullfile(str);

%% Data Trimming
j=1;
for i=1:9
    str=sprintf('Experiment %d.lvm',i);
    dataname=fullfile(fp,str);
    if isfile(dataname)
        data=load(dataname);
        Result=V1_Forearm_datatrimming(data,i,40,true);
        res(j,1)=Result; % Result (1,1).Time would give a
        % the time vector for 1st exp
        clear dataname data
        j=j+1;
    end
end
close all
```

```

else
    data=NaN;
    Result=V1_Forearm_datatrimming(data,i,40,true);
    res(j,1)=Result; % Result (1,1).Time would give a the
    % time vector for 1st exp
    clear dataname data
    j=j+1;
    close all
end

end

end

%% Perform Curve fit to obtain force coefficients using MW-3
for exp=1:length(res)
    flag1=true;
    depth(exp,1)=res(exp).Pos(1);
    T1=res(exp,1).Time;
    L1=res(exp,1).SG_1;

    % Setup bounds and initial points
    lb=[0 0 0];
    ub=[100 100 100];

    p0=[1 1 1];

    [const,R_nor,]=lsqcurvefit(@Maxwell_1_arm,p0,T1,L1,lb,ub);

    % Setup the problem for multistart to avoid local minimum
    problem=createOptimProblem('lsqcurvefit','x0',p0,'objective',@Maxwell_1_arm,'
        lb',lb,'ub',ub,'xdata',T1,'ydata',L1);
    ms=MultiStart();
    [xmulti,errormulti] = run(ms,problem,50);

    % plot trim data by setting flag1=true
    if flag1==false
        plot_stress_relax(const, T1, L1, R_nor)
    end
end

```

```

end

vis_prop(exp, :)=[const,R_nor];
vis_prop2(exp, :)=[xmulti,errormulti]; % Solution with multi start to avoid
    local minima

clear const R_nor xmulti errormulti T1 L1

end

%% Create Subplot with raw data (N) for all 9 exp on single participant
t = tiledlayout(3,3,'TileSpacing','Compact','Padding','Compact');
nexttile
T1=res(1).Raw_Time;
L1=res(1).Raw_Load;
trim_load1=res(1).SG_1;
T1_fit=res(1).Time;
L1_fit=Maxwell_1_arm(vis_prop2(1,(1:3)),T1_fit);
plot(T1,L1,'r*')
title('Exp1')

nexttile
T2=res(2).Raw_Time;
L2=res(2).Raw_Load;
T2_fit=res(2).Time;
trim_load2=res(2).SG_1;
L2_fit=Maxwell_1_arm(vis_prop2(2,(1:3)),T2_fit);
plot(T2,L2,'r*')
title('Exp2')

nexttile
T3=res(3).Raw_Time;
L3=res(3).Raw_Load;
T3_fit=res(3).Time;

```

```

trim_load3=res(3).SG_l;
L3_fit=Maxwell_1_arm(vis_prop2(3,(1:3)),T3_fit);
plot(T3,L3,'r*')
title('Exp3')

nexttile
T4=res(4).Raw_Time;
L4=res(4).Raw_Load;
T4_fit=res(4).Time;
trim_load4=res(4).SG_l;
L4_fit=Maxwell_1_arm(vis_prop2(4,(1:3)),T4_fit);
plot(T4,L4,'r*')
title('Exp4')

nexttile
T5=res(5).Raw_Time;
L5=res(5).Raw_Load;
T5_fit=res(5).Time;
trim_load5=res(5).SG_l;
L5_fit=Maxwell_1_arm(vis_prop2(5,(1:3)),T5_fit);
plot(T5,L5,'r*')
title('Exp5')

nexttile
T6=res(6).Raw_Time;
L6=res(6).Raw_Load;
T6_fit=res(6).Time;
trim_load6=res(6).SG_l;
L6_fit=Maxwell_1_arm(vis_prop2(6,(1:3)),T6_fit);
plot(T6,L6,'r*')
title('Exp6')

nexttile

```

```

T7=res(7).Raw_Time;
L7=res(7).Raw_Load;
T7_fit=res(7).Time;
trim_load7=res(7).SG_1;
L7_fit=Maxwell_1_arm(vis_prop2(7,(1:3)),T7_fit);
plot(T7,L7,'r*')
title('Exp7')

nexttile
T8=res(8).Raw_Time;
L8=res(8).Raw_Load;
T8_fit=res(8).Time;
trim_load8=res(8).SG_1;
L8_fit=Maxwell_1_arm(vis_prop2(8,(1:3)),T8_fit);
plot(T8,L8,'r*')
title('Exp8')

nexttile
T9=res(9).Raw_Time;
L9=res(9).Raw_Load;
T9_fit=res(9).Time;
trim_load9=res(9).SG_1;
L9_fit=Maxwell_1_arm(vis_prop2(9,(1:3)),T9_fit);
plot(T9,L9,'r*')
title('Exp9')

ylabel(t,'Load (grams)',fontsize=15);
xlabel(t,'Time (s)',fontsize=15);

copygraphics(t,'BackgroundColor','none')

%% Create subplot for trimmed data
figure();
curvefit_linewidth=5;

```

```

t1 = tiledlayout(3,3,'TileSpacing','Compact','Padding','Compact');
nexttile
p1=plot(T1_fit,L1_fit,'b-',T1_fit,trim_load1, 'r*');
p1(1).LineWidth=curvefit_linewidth;
title('Exp1')

nexttile
p2=plot(T2_fit,L2_fit,'b-',T2_fit,trim_load2, 'r*');
p2(1).LineWidth=curvefit_linewidth;
title('Exp2')

nexttile
p3=plot(T3_fit,L3_fit,'b-',T3_fit,trim_load3, 'r*');
p3(1).LineWidth=curvefit_linewidth;
title('Exp3')

nexttile
p4=plot(T4_fit,L4_fit,'b-',T4_fit,trim_load4, 'r*');
p4(1).LineWidth=curvefit_linewidth;
title('Exp4')

nexttile
p5=plot(T5_fit,L5_fit,'b-',T5_fit,trim_load5, 'r*');
p5(1).LineWidth=curvefit_linewidth;
title('Exp5')

nexttile
p6=plot(T6_fit,L6_fit,'b-',T6_fit,trim_load6, 'r*');
p6(1).LineWidth=curvefit_linewidth;
title('Exp6')

nexttile
p7=plot(T7_fit,L7_fit,'b-',T7_fit,trim_load7, 'r*');
p7(1).LineWidth=curvefit_linewidth;
title('Exp7')

```

```

nexttile
p8=plot(T8_fit,L8_fit,'b-',T8_fit,trim_load8, 'r*');
p8(1).LineWidth=curvefit_linewidth;
title('Exp8')

nexttile
p9=plot(T9_fit,L9_fit,'b-',T9_fit,trim_load9, 'r*');
p9(1).LineWidth=curvefit_linewidth;
title('Exp9')

ylabel(t1,'Load (grams)',fontsize=15);
xlabel(t1,'Time (s)',fontsize=15);

%% Obtain Shear Modulus Viscoelastic parameters
B0=vis_prop2(:,1).*0.0098./(depth(:,1).^ (3/2) .* ((8/3) .*sqrt(SH_R))) .*1e3;
B1=vis_prop2(:,2).*0.0098./(depth(:,1).^ (3/2) .* ((8/3) .*sqrt(SH_R))) .*1e3;
B=[B0 B1 vis_prop2(:,3)];

%% Save data to Post-ProcessedData

fp1=addpath('C:\Users\kumats\OneDrive - University of Texas at Arlington\IRB
    MicroForceSensor and HRI\Shashank IRB forms\0IRB 2023-0306_Data\Data');
filename='Post-ProcessedData.xlsx';
filename_Ident='IdentifierInformation.xlsx';

raw_data=readtable('Post-ProcessedData.xlsx');
raw_data_Ident=readtable("IdentifierInformation.xlsx");
demographics=raw_data_Ident((Parti_ID-100),3:7);

B_all=reshape(B',27,1)'; %X_ij= ith coefficient for jth experiment %[B01 B11
    Tau01 B02 B12 Tau02 B03 B13 Tau03 ...]
B_all_table=num2cell(B_all);
new_data1=[Parti_ID,demographics.Gender,demographics.Age,demographics.
    Age_5year_Span,demographics.Race,demographics.Gym_,B_all_table];

```

```

new_data=cell2table(new_data1,'VariableNames',raw_data.Properties.
    VariableNames);

raw_data=[raw_data;new_data];

%% Save to Excel?
save_flag=questdlg('Do you want to save this data to Postprocessed output
    file?','Append data?','Yes','No','No');

switch save_flag
    case 'Yes'
        disp('Saved')
        writetable(raw_data,'C:\Users\kumats\OneDrive - University of Texas
            at Arlington\Shashank Weekly - Shiakolas Panos S files\Dissertation
            Proposal Documents-PreviousLabMembers\Shashank\0DissertationDocument\
            Tissuecharacterization_Data\Post-ProcessedData.xlsx')
    case 'No'
        disp('Not Saved')
end

%% V1_Forearm_datatrimming
function Result=V1_Forearm_datatrimming (data,exp_num,hld_t,flag)
    if isnan(data)
        T=0;
        P=0;
        Rsg=0;
        L=0;
        exp.T=0;
        exp.L=0;
        Result=struct('Time',T,'Pos',P,'SG_r',Rsg,'SG_l',L,'Raw_Time',exp.T,'
            Raw_Load',exp.L);
    else
        exp.num=['exp' num2str(exp_num)]; % generate list of experiment
        numbers
    end
end

```

```

exp.T=data(:,1);
exp.d=data(:,2)./1000; % desired distance travel in mm
exp.R=data(:,4);
exp.L=data(:,5); % Load sensed by strain gauge (grams)

if flag==true
    figure(exp_num)
    plot(exp.T,exp.L)
    xlabel('Time')
    ylabel('Load (grams)')
end

%% Code patch to manually select start location on the Graph
dcmObject = datacursormode;
pause
datacursormode off
cursor = getCursorInfo(dcmObject);
y= cursor.Position(2);
idx_strt=find(abs(exp.L-y)<=0.5,1);
%%
% [~, idx_strt]=max(exp.L(:));
strt_T=exp.T(idx_strt);
stp_T=strt_T+hld_t;
idx_stp=find(abs(exp.T-stp_T)<=0.5,1);

T=linspace(0,hld_t,(idx_stp-idx_strt+1))';
P=exp.d(idx_strt:idx_stp);
Rsg=exp.R(idx_strt:idx_stp);
L=exp.L(idx_strt:idx_stp);

% Define output
Result=struct('Time',T,'Pos',P,'SG_r',Rsg,'SG_l',L,'Raw_Time',exp.T,'
Raw_Load',exp.L,'Raw_Pos',exp.d);

end

```

```

end

%% Maxwell_1_arm
function f=Maxwell_1_arm(const,x)
    E0=const(1);
    E1=const(2);
    tau1=const(3);
    f=E0+(E1*exp(-x/tau1));
end

%% Plot stress_relax

function plot_stress_relax(const, T1, L1, R_nor)
L1_fit=Maxwell_1_arm(const,T1);
figure ()
plot(T1,L1,'ro','MarkerSize',20)
hold on
plot(T1,L1_fit,'k-','LineWidth',5)
legend('Experimental data','Curvefit','FontSize',25)
grid on
% Evaluate R squared
mean_L=(1/length(L1))*(sum(L1));
% SS_res=sum((Load-yfit).^2);
SS_tot=sum((L1-mean_L).^2);
R_sq=1-(R_nor)/(SS_tot);
str=[sprintf('f(t) = '), sprintf('%.2f+%.2f*e^{(-t/%.2f)}}, R^2=%.3f',const(1)
    ,const(2),const(3),R_sq)];
xl = xlim;
yl = ylim;
xt = 0.20 * (xl(2)-xl(1)) + xl(1);
yt = 0.78 * (yl(2)-yl(1)) + yl(1);
dimen=[0.3,0.70,0.3,0.2];
ytickformat('%.2f')
xlabel("Time (seconds)")

```

```
ylabel("Tissue Reaction (grams)")
a = annotation('textbox',dimen,'String',str,'FitBoxToText','on');
a.BackgroundColor='w';
a.FontSize=25;
box on
yafs=25; % Yaxis Tick Font size
ax.YAxis.FontSize = yafs;
ax.XAxis.FontSize = yafs;
ax.GridAlpha =1;
grid on
grid minor
pbaspect([1.25 1 1]);
end
```

APPENDIX C

C.1 LabVIEW Stepper-Motor Control VI

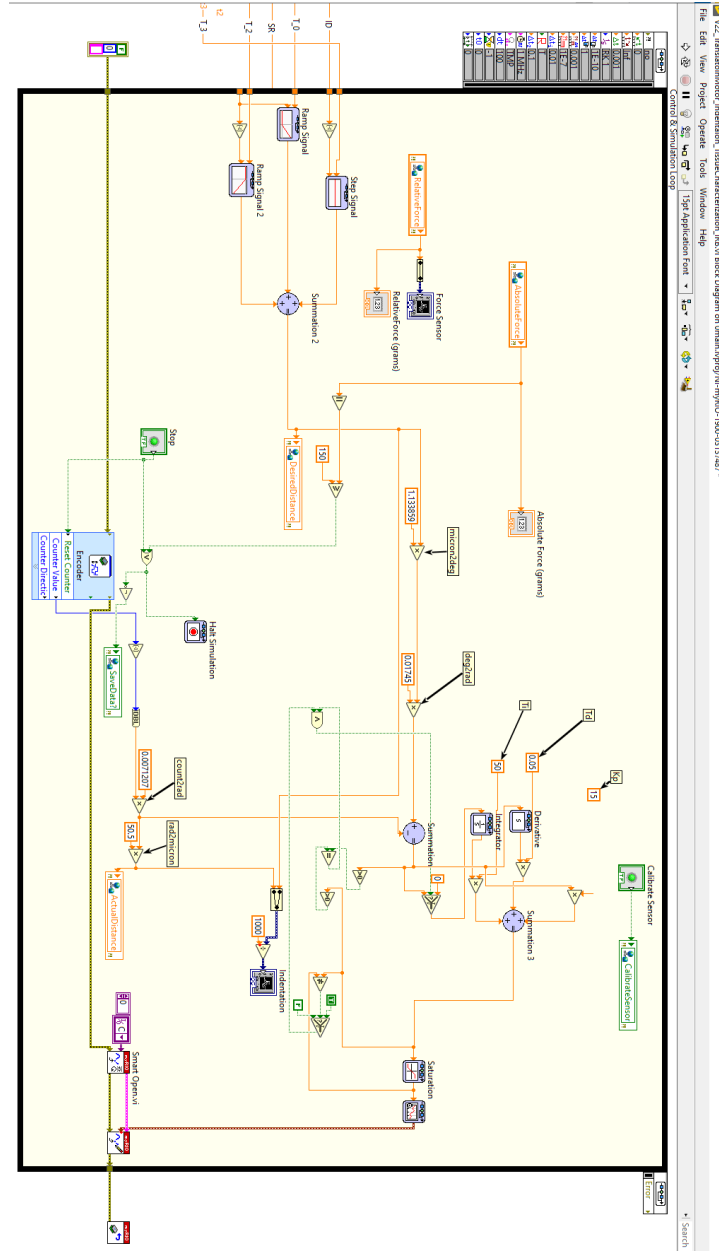


Figure C.1: Stepper motor control block diagram

C.2 LabVIEW Servo-Motor Control VI for Tissue characterization

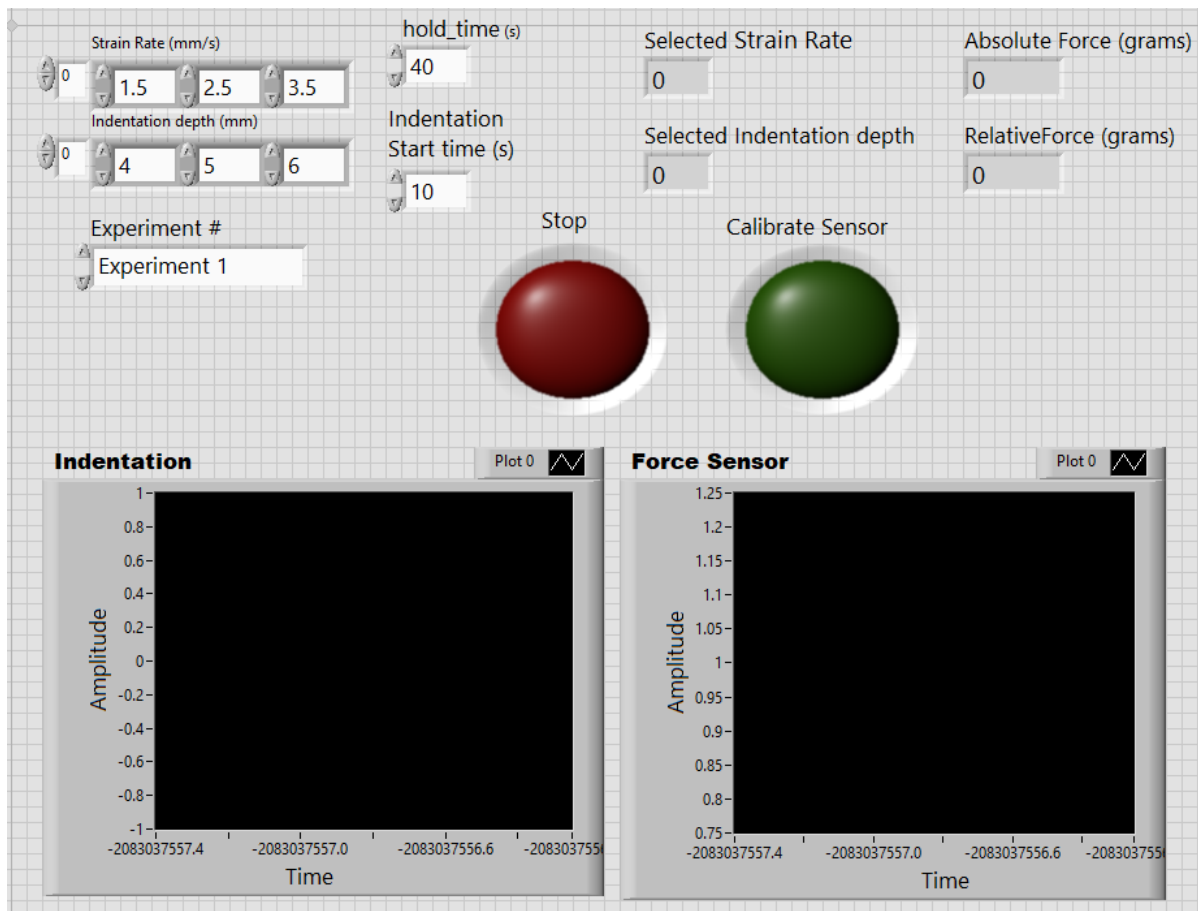


Figure C.2: Servo motor control front panel

BIBLIOGRAPHY

- [1] J. Guo, B. Xiao, and H. Ren, “Compensating uncertainties in force sensing for robotic-assisted palpation,” Applied Sciences, vol. 9, p. 2573, 6 2019.
- [2] H. Benzon, S. Fishman, S. Liu, S. P. Cohen, and S. N. Raja, Essentials of Pain Medicine. Elsevier, 2011.
- [3] G. K. Bigley, Sensation. 1990.
- [4] A. Westerband, G. C. Hunter, I. Cintora, S. W. Coulthard, M. L. Hinni, A. T. Gentile, J. Devine, and J. L. Mills, “Current trends in the detection and management of carotid body tumors,” Journal of Vascular Surgery, vol. 28, pp. 84–93, 7 1998.
- [5] S. Huang and D. E. Ingber, “Cell tension, matrix mechanics, and cancer development,” Cancer Cell, vol. 8, pp. 175–176, 9 2005.
- [6] G. Y. Lee and C. T. Lim, “Biomechanics approaches to studying human diseases,” Trends in Biotechnology, vol. 25, pp. 111–118, 3 2007.
- [7] A. Fuhrmann, J. R. Staunton, V. Nandakumar, N. Banyai, P. C. W. Davies, and R. Ros, “Afm stiffness nanotomography of normal, metaplastic and dysplastic human esophageal cells,” Physical Biology, vol. 8, p. 015007, 2 2011.
- [8] M. Prabhune, G. Belge, A. Dotzauer, J. Bullerdiek, and M. Radmacher, “Comparison of mechanical properties of normal and malignant thyroid cells,” Micron, vol. 43, pp. 1267–1272, 12 2012.
- [9] G. Ferraioli, C. Filice, L. Castera, B. I. Choi, I. Sporea, S. R. Wilson, D. Cosgrove, C. F. Dietrich, D. Amy, J. C. Bamber, R. Barr, Y.-H. Chou, H. Ding, A. Farrokh, M. Friedrich-Rust, T. J. Hall, K. Nakashima, K. R. Nightingale, M. L. Palmeri, F. Schafer, T. Shiina, S. Suzuki, and M. Kudo, “Wfumb guidelines and recommendations for clinical use of ultrasound elastography: Part 3: Liver,” Ultrasound in Medicine & Biology, vol. 41, pp. 1161–1179, 5 2015.
- [10] T. Shiina, K. R. Nightingale, M. L. Palmeri, T. J. Hall, J. C. Bamber, R. G. Barr, L. Castera, B. I. Choi, Y.-H. Chou, D. Cosgrove, C. F. Dietrich, H. Ding, D. Amy, A. Farrokh, G. Ferraioli, C. Filice, M. Friedrich-Rust, K. Nakashima, F. Schafer, I. Sporea, S. Suzuki, S. Wilson, and M. Kudo, “Wfumb guidelines and recommendations for clinical use of ultrasound elastography: Part 1: Basic principles and terminology,” Ultrasound in Medicine & Biology, vol. 41, pp. 1126–1147, 5 2015.
- [11] R. G. Barr, K. Nakashima, D. Amy, D. Cosgrove, A. Farrokh, F. Schafer, J. C. Bamber, L. Castera, B. I. Choi, Y.-H. Chou, C. F. Dietrich, H. Ding, G. Ferraioli, C. Filice, M. Friedrich-Rust, T. J. Hall, K. R. Nightingale, M. L. Palmeri, T. Shiina, S. Suzuki, I. Sporea, S. Wilson, and M. Kudo, “Wfumb guidelines and recommendations for clinical use of ultrasound elastography: Part 2: Breast,” Ultrasound in Medicine & Biology, vol. 41, pp. 1148–1160, 5 2015.

- [12] R. G. Barr, D. Cosgrove, M. Brock, V. Cantisani, J. M. Correas, A. W. Postema, G. Salomon, M. Tsutsumi, H.-X. Xu, and C. F. Dietrich, “Wfumb guidelines and recommendations on the clinical use of ultrasound elastography: Part 5. prostate,” Ultrasound in Medicine & Biology, vol. 43, pp. 27–48, 1 2017.
- [13] J.-L. Hsu, C.-H. Lee, and C.-H. Hsieh, “Digitizing abdominal palpation with a pressure measurement and positioning device,” PeerJ, vol. 8, p. e10511, 12 2020.
- [14] A. K. Czech, K. Gronostaj, J. Fronczek, J. Frydrych, V. Bezshapkin, M. Przydacz, P. Dudek, L. Curylo, T. Wiatr, J. Gasowski, and P. L. Chlosta, “Diagnostic accuracy of bimanual palpation in bladder cancer patients undergoing cystectomy: A prospective study,” Urologic oncology, vol. 41, pp. 390.e27–390.e33, 9 2023.
- [15] P. Culmer, J. Barrie, R. Hewson, M. Levesley, M. Mon-Williams, D. Jayne, and A. Neville, “Reviewing the technological challenges associated with the development of a laparoscopic palpation device,” The International Journal of Medical Robotics and Computer Assisted Surgery, vol. 8, pp. 146–159, 6 2012.
- [16] C.-Z. Zhu, H.-N. Ting, K.-H. Ng, and T.-A. Ong, “A review on the accuracy of bladder cancer detection methods,” Journal of Cancer, vol. 10, pp. 4038–4044, 2019.
- [17] S. Kaulitzki, “Human bladder in pelvis, illustration stock photo - alamy,” 2013.
- [18] JohnHopkinsMedicine, “Anatomy of the urinary system — johns hopkins medicine.”
- [19] J. L. Gleason, “Cystoscopy and other urogynecologic procedures,” Obstetrics and Gynecology Clinics of North America, vol. 40, pp. 773–785, 12 2013.
- [20] C. R. UK, “What are cystoscopy and ureteroscopy?.”
- [21] R. Alteri, C. Ogoro, and B. Lubejko, “About bladder cancer,” 2019.
- [22] R. L. Siegel, K. D. Miller, N. S. Wagle, and A. Jemal, “Cancer statistics, 2023.,” CA: a cancer journal for clinicians, vol. 73, pp. 17–48, 1 2023.
- [23] O. Clark, T. Sarmiento, A. Eccleston, J. Brinkmann, R. Picoli, V. Daliparthi, J. Voss, S. Chandrasekar, A. Thompson, and J. Chang, “Economic impact of bladder cancer (bc) in the united states (us).,” Journal of Clinical Oncology, vol. 41, pp. 479–479, 2 2023.
- [24] I. Milsom, K. S. Coyne, S. Nicholson, M. Kvasz, C.-I. Chen, and A. J. Wein, “Global prevalence and economic burden of urgency urinary incontinence: A systematic review,” European Urology, vol. 65, pp. 79–95, 1 2014.
- [25] K. S. Coyne, “Economic burden of urgency urinary incontinence in the united states: A systematic review,” tech. rep., 2014.
- [26] A. Ansardamavandi, M. Tafazzoli-Shadpour, R. Omidvar, and I. Jahanzad, “Quantification of effects of cancer on elastic properties of breast tissue by atomic force microscopy,” Journal of the Mechanical Behavior of Biomedical Materials, vol. 60, pp. 234–242, 7 2016.

- [27] M. Kauer, V. Vuskovic, J. Dual, G. Szekely, and M. Bajka, "Inverse finite element characterization of soft tissues," 2001.
- [28] T. P. Prevost, G. Jin, M. A. de Moya, H. B. Alam, S. Suresh, and S. Socrate, "Dynamic mechanical response of brain tissue in indentation in vivo, in situ and in vitro," Acta Biomaterialia, vol. 7, pp. 4090–4101, 12 2011.
- [29] M. P. Ottensmeyer, A. E. Kerdok, R. D. Howe, and S. L. Dawson, "The effects of testing environment on the viscoelastic properties of soft tissues," 2004.
- [30] F. Carter, T. Frank, P. Davies, D. McLean, and A. Cuschieri, "Measurements and modelling of the compliance of human and porcine organs," Medical Image Analysis, vol. 5, pp. 231–236, 12 2001.
- [31] J. Kim, B. K. Tay, N. Stylopoulos, D. W. Rattner, and M. A. Srinivasan, "Characterization of intra-abdominal tissues from in vivo animal experiments for surgical simulation," 2003.
- [32] S. Barnes, B. Lawless, D. Shepherd, D. Espino, G. Bicknell, and R. Bryan, "Viscoelastic properties of human bladder tumours," Journal of the Mechanical Behavior of Biomedical Materials, vol. 61, pp. 250–257, 8 2016.
- [33] P. Puangmali, H. Liu, L. D. Seneviratne, P. Dasgupta, and K. Althoefer, "Miniature 3-axis distal force sensor for minimally invasive surgical palpation," IEEE/ASME Transactions on Mechatronics, vol. 17, pp. 646–656, 8 2012.
- [34] H.-K. Lee, J. Chung, S.-I. Chang, and E. Yoon, "Normal and shear force measurement using a flexible polymer tactile sensor with embedded multiple capacitors," Journal of Microelectromechanical Systems, vol. 17, pp. 934–942, 8 2008.
- [35] P. Polygerinos, P. Puangmali, T. Schaeffter, R. Razavi, L. D. Seneviratne, and K. Althoefer, "Novel miniature mri-compatible fiber-optic force sensor for cardiac catheterization procedures," pp. 2598–2603, IEEE, 5 2010.
- [36] M. Tanimoto, F. Arai, T. Fukuda, H. Iwata, K. Itoigawa, Y. Gotoh, M. Hashimoto, and M. Negoro, "Micro force sensor for intravascular neurosurgery and in vivo experiment," pp. 504–509, IEEE, 1998.
- [37] E. Samur, M. Sedef, C. Basdogan, L. Avtan, and O. Duzgun, "A robotic indenter for minimally invasive measurement and characterization of soft tissue response," Medical Image Analysis, vol. 11, pp. 361–373, 8 2007.
- [38] M. Abraham, "Automated system for the characterization of the biomechanical properties of human soft tissue," 2016.
- [39] T. Li, A. Pan, and H. Ren, "A high-resolution triaxial catheter tip force sensor with miniature flexure and suspended optical fibers," IEEE Transactions on Industrial Electronics, vol. 67, pp. 5101–5111, 6 2020.

- [40] S. S. Kumat and P. S. Shiakolas, “Design, inverted vat photopolymerization 3d printing, and initial characterization of a miniature force sensor for localized in vivo tissue measurements,” 3D Printing in Medicine, vol. 8, p. 1, 12 2022.
- [41] M. C. Yip, S. G. Yuen, and R. D. Howe, “A robust uniaxial force sensor for minimally invasive surgery,” IEEE transactions on bio-medical engineering, vol. 57, pp. 1008–11, 5 2010.
- [42] B. Alekya, V. S. N. S. V., A. B. S., and H. J. Pandya, “Sensor for meso-scale tissue stiffness characterization,” IEEE Sensors Journal, vol. 22, pp. 6442–6453, 4 2022.
- [43] Z. Tang, S. Wang, M. Li, and C. Shi, “Development of a distal tri-axial force sensor for minimally invasive surgical palpation,” IEEE Transactions on Medical Robotics and Bionics, vol. 4, pp. 145–155, 2 2022.
- [44] J. Palacio-Torralba, S. Hammer, D. W. Good, S. A. McNeill, G. D. Stewart, R. L. Reuben, and Y. Chen, “Quantitative diagnostics of soft tissue through viscoelastic characterization using time-based instrumented palpation,” Journal of the Mechanical Behavior of Biomedical Materials, vol. 41, pp. 149–160, 1 2015.
- [45] M. A. Soebadi, T. Weydts, L. Brancato, L. Hakim, R. Puers, and D. D. Ridder, “Novel implantable pressure and acceleration sensor for bladder monitoring,” International Journal of Urology, vol. 27, pp. 543–550, 6 2020.
- [46] A. Maccabi, A. Shin, N. K. Namiri, N. Bajwa, M. S. John, Z. D. Taylor, W. Grundfest, and G. N. Saddik, “Quantitative characterization of viscoelastic behavior in tissue-mimicking phantoms and ex vivo animal tissues,” PLOS ONE, vol. 13, p. e0191919, 1 2018.
- [47] M. H. Friedman, “Biomechanics: Mechanical properties of living tissues y. c. fung,” The Quarterly Review of Biology, vol. 69, pp. 572–573, 12 1994.
- [48] X. Wang, J. A. Schoen, and M. E. Rentschler, “A quantitative comparison of soft tissue compressive viscoelastic model accuracy,” Journal of the Mechanical Behavior of Biomedical Materials, vol. 20, pp. 126–136, 4 2013.
- [49] S. Adejokun and P. Shiakolas, “A compliant manipulator for confined space tissue diagnostics: Kinematic and force analyses and initial characterization experiments,” Journal of Mechanisms and Robotics, pp. 1–23, 6 2023.
- [50] S. A. Adejokun, S. S. Kumat, and P. S. Shiakolas, “A microrobot with an attached microforce sensor for natural orifice access to the bladder interior wall,” American Society of Mechanical Engineers, 10 2022.
- [51] S. A. Adejokun, S. S. Kumat, and P. S. Shiakolas, “A microrobot with an attached microforce sensor for transurethral access to the bladder interior wall,” Journal of Engineering and Science in Medical Diagnostics and Therapy, vol. 6, pp. 1–29, 8 2023.
- [52] B. Luo, Y. Deng, T. Yang, S. Dai, and G. Song, “Design of a miniature fiber optic sensor to measure axial force at the tip of a robotic flexible ureteroscopy,” pp. 2554–2559, IEEE, 11 2019.

- [53] D. Shin, H.-U. Kim, A. Kulkarni, Y.-H. Kim, and T. Kim, "Development of force sensor system based on tri-axial fiber bragg grating with flexure structure," *Sensors*, vol. 22, p. 16, 12 2021.
- [54] W. Wang, Y. Zhao, and Q. Lin, "An integrated mems tactile tri-axial micro-force probe sensor for minimally invasive surgery," pp. 71–76, *IEEE*, 2009.
- [55] Y. Deng, T. Yang, S. Dai, and G. Song, "A miniature triaxial fiber optic force sensor for flexible ureteroscopy," *IEEE Transactions on Biomedical Engineering*, vol. 68, pp. 2339–2347, 8 2021.
- [56] S. Standing, *The anatomical basis of clinical practice*. Jeremy Bowes, 2016.
- [57] G. S. Bhat, M. Shivalingiah, G. G. Nelivigi, and C. Ratkal, "The size of external urethral meatus on maximum stretch in indian adult males," *Indian Journal of Surgery*, vol. 76, pp. 85–89, 2 2014.
- [58] C. D. BERRY, "Urethral meatal caliber in circumcised and uncircumcised males," *Archives of Pediatrics & Adolescent Medicine*, vol. 92, p. 152, 8 1956.
- [59] R. G. Hudson, M. J. Conlin, and D. H. Bagley, "Ureteric access with flexible ureteroscopes: effect of the size of the ureteroscope," *BJU International*, vol. 95, pp. 1043–1044, 5 2005.
- [60] A. Miernik, K. Wilhelm, P. U. Ardel, F. Adams, F. E. Kuehhas, and M. Schoenthaler, "Standardized flexible ureteroscopic technique to improve stone-free rates," *Urology*, vol. 80, pp. 1198–1202, 12 2012.
- [61] S. K. Lildal, K. H. Andreassen, H. Jung, M. R. Pedersen, and P. J. S. Osther, "Evaluation of ureteral lesions in ureterorenoscopy: impact of access sheath use," *Scandinavian Journal of Urology*, vol. 52, pp. 157–161, 3 2018.
- [62] T. Li, C. Shi, and H. Ren, "Three-dimensional catheter distal force sensing for cardiac ablation based on fiber bragg grating," *IEEE/ASME Transactions on Mechatronics*, vol. 23, pp. 2316–2327, 10 2018.
- [63] A. Gao, Y. Zhou, L. Cao, Z. Wang, and H. Liu, "Fiber bragg grating-based triaxial force sensor with parallel flexure hinges," *IEEE Transactions on Industrial Electronics*, vol. 65, pp. 8215–8223, 10 2018.
- [64] P. Puangmali, K. Althoefer, L. D. Seneviratne, D. Murphy, and P. Dasgupta, "State-of-the-art in force and tactile sensing for minimally invasive surgery," *IEEE Sensors Journal*, vol. 8, pp. 371–381, 4 2008.
- [65] Y. Hu, R. B. Katragadda, H. Tu, Q. Zheng, Y. Li, and Y. Xu, "Bioinspired 3-d tactile sensor for minimally invasive surgery," *Journal of Microelectromechanical Systems*, vol. 19, pp. 1400–1408, 12 2010.
- [66] C. Shi, T. Li, and H. Ren, "A millinewton resolution fiber bragg grating-based catheter two-dimensional distal force sensor for cardiac catheterization," *IEEE Sensors Journal*, vol. 18, pp. 1539–1546, 2 2018.

- [67] N. Kumar, O. Piccin, L. Meylheuc, L. Barbe, and B. Bayle, “Design and modeling of a polymer force sensor,” IEEE/ASME Transactions on Mechatronics, vol. 21, pp. 1–1, 2015.
- [68] I. V. P. Group, “Linear patterns — single grid advanced sensors linear patterns — single grid,” 2021.
- [69] J. M. Gere and B. J. Goodno, Mechanics of Materials. Cengage Learning, seventh ed ed., 2009.
- [70] A. Festas, A. Ramos, and J. Davim, “Medical devices biomaterials ;scpl– a;/scpl review,” Proceedings of the Institution of Mechanical Engineers, Part L: Journal of Materials: Design and Applications, vol. 234, pp. 218–228, 1 2020.
- [71] R. L. Norton, Machine Design An Integrated Approach. Pearson Education, fourth ed., 2010.
- [72] S. Kalpakjian and S. R. Schmid, Manufacturing Engineering and Technology Forth Edition. Prentice hall, 2000.
- [73] Matweb, “Overview of materials data for Aluminum Alloy.” <https://www.matweb.com/search/datasheet.aspx?matguid=ab8aeb2d293041c4a844e397b5cfbd4e{&}n=1>.
- [74] Formlabs, “Which Formlabs resins print with the Form 3/Form 3B?” https://support.formlabs.com/s/article/What-Formlabs-resins-work-with-the-new-Form-3?language=en_US, mar 2020.
- [75] C. Duarte, I. Babuška, and J. Oden, “Generalized finite element methods for three-dimensional structural mechanics problems,” Computers & Structures, vol. 77, pp. 215–232, 6 2000.
- [76] FormLabs, “Design specifications for 3d models (form 3/form 3b).” https://support.formlabs.com/s/article/Design-specifications-for-3D-models-form-3?language=en_US, 2020.
- [77] N. Instruments, “Ni-9219 specifications,” 2023.
- [78] W. Bolton, Instrumentation and Control Systems. Oxford: Newnes, first ed., 2004.
- [79] N. Instruments, “Understanding instrument specifications – how to make sense out of the jargon - ni,” 2019.
- [80] W. Nawrocki, “Measurement systems and sensors,” Choice Reviews Online, vol. 43, pp. 43–4048–43–4048, 3 2006.
- [81] J. J. Carr, Introduction to Biomedical Equipment Technology. Pearson Education, 2001.

- [82] L. S. Taylor, A. L. Lerner, D. J. Rubens, and K. J. Parker, “A kelvin-voight fractional derivative model for viscoelastic characterization of liver tissue,” pp. 447–448, *ASME*, 1 2002.
- [83] D. Gutierrez-Lemini, *Engineering Viscoelasticity*. Springer US, 2013.
- [84] R. Zhang, P. Iravani, and P. S. Keogh, “Modelling dielectric elastomer actuators using higher order material characteristics,” *Journal of Physics Communications*, vol. 2, p. 045025, 4 2018.
- [85] C.-J. Chuong, M. Ma, R. C. Eberhart, and P. Zimmern, “Viscoelastic properties measurement of the prolapsed anterior vaginal wall: a patient-directed methodology,” *European Journal of Obstetrics & Gynecology and Reproductive Biology*, vol. 173, pp. 106–112, 2 2014.
- [86] C. N. Wang, M. R. Abraham, C. E. Abrego, P. S. Shiakolas, A. Christie, and P. E. Zimmern, “An operator-independent artificial finger can differentiate anterior vaginal wall indentation parameters between control and prolapse patients,” *Journal of Biomechanics*, vol. 120, p. 110378, 5 2021.
- [87] J. M. Mattice, A. G. Lau, M. L. Oyen, and R. W. Kent, “Spherical indentation load-relaxation of soft biological tissues,” *Journal of Materials Research*, vol. 21, pp. 2003–2010, 8 2006.
- [88] M. L. Oyen, “Spherical indentation creep following ramp loading,” *Journal of Materials Research*, vol. 20, pp. 2094–2100, 8 2005.
- [89] B. Qiang, J. Greenleaf, M. Oyen, and X. Zhang, “Estimating material elasticity by spherical indentation load-relaxation tests on viscoelastic samples of finite thickness,” *IEEE Transactions on Ultrasonics, Ferroelectrics and Frequency Control*, vol. 58, pp. 1418–1429, 7 2011.
- [90] T. A. Krouskop, T. M. Wheeler, F. Kallel, B. S. Garra, and T. Hall, “Elastic moduli of breast and prostate tissues under compression,” *Ultrasonic Imaging*, vol. 20, pp. 260–274, 10 1998.
- [91] S. A. Kruse, J. A. Smith, A. J. Lawrence, M. A. Dresner, A. Manduca, J. F. Greenleaf, R. L. Ehman, S. A. Kruse, J. A. Smith, A. J. Lawrence, M. A. Dresner, A. Manduca, and J. F. Greenleaf, “Tissue characterization using magnetic resonance elastography: preliminary results*,” *Physics in Medicine and Biology*, vol. 45, pp. 1579–1590, 6 2000.
- [92] Y. Zheng and A. Mak, “Extraction of effective young’s modulus of skin and subcutaneous tissues from manual indentation data,” vol. 5, pp. 2246–2249, *IEEE*.
- [93] K. Ohsugi, T. Uchiyama, and M. Murayama, “Elastic- and viscous-like properties of the upper arm estimated by the indentation method,” pp. 268–269, *IEEE*, 2003.
- [94] C. Pailler-Mattei, S. Bec, and H. Zahouani, “In vivo measurements of the elastic mechanical properties of human skin by indentation tests,” *Medical Engineering & Physics*, vol. 30, pp. 599–606, 6 2008.

- [95] J. Su, H. Zou, and T. Guo, “The study of mechanical properties on soft tissue of human forearm in vivo,” pp. 1–4, *IEEE*, 6 2009.
- [96] B. Ahn and J. Kim, “Measurement and characterization of soft tissue behavior with surface deformation and force response under large deformations,” *Medical Image Analysis*, vol. 14, pp. 138–148, 4 2010.
- [97] M. R. Baroudi, P. C. Ferguson, J. S. Wunder, M. H. Isler, S. Mottard, J. A. Werier, and R. E. Turcotte, “Forearm soft tissue sarcoma: Tumors characteristics and oncologic outcomes following limb salvage surgery,” *Journal of Surgical Oncology*, vol. 110, pp. 676–681, 11 2014.
- [98] R. Eberhart, C. Chuong, and P. Zimmern, “Exploring biomechanical methods to study the human vaginal wall,” *Neurourology and Urodynamics*, vol. 36, pp. 499–506, 2 2017.
- [99] S. Park, “Biochemical, structural and physical changes in aging human skin, and their relationship,” *Biogerontology*, vol. 23, pp. 275–288, 6 2022.
- [100] S. Park, J. Tao, L. Sun, C.-M. Fan, and Y. Chen, “An economic, modular, and portable skin viscoelasticity measurement device for in situ longitudinal studies,” *Molecules*, vol. 24, p. 907, 3 2019.
- [101] S. Park, A. L. Chien, I. D. Brown, and J. Chen, “Characterizing viscoelastic properties of human melanoma tissue using prony series,” *Frontiers in Bioengineering and Biotechnology*, vol. 11, 4 2023.
- [102] M. F. Teodoro, “Mechanical behavior of the skin: Men versus women, a preliminary analysis,” 2022.
- [103] L. Qian, H. Zhao, Y. Guo, Y. Li, M. Zhou, L. Yang, Z. Wang, and Y. Sun, “Influence of strain rate on indentation response of porcine brain,” *Journal of the Mechanical Behavior of Biomedical Materials*, vol. 82, pp. 210–217, 6 2018.
- [104] W. Hayes, L. Keer, G. Herrmann, and L. Mockros, “A mathematical analysis for indentation tests of articular cartilage,” *Journal of Biomechanics*, vol. 5, pp. 541–551, 9 1972.
- [105] B. Johnson, S. Campbell, and N. Campbell-Kyureghyan, “Biomechanical properties of abdominal organs under tension with special reference to increasing strain rate,” *Journal of Biomechanics*, vol. 109, p. 109914, 8 2020.
- [106] Y. Zheng and A. Mak, “Extraction of effective young’s modulus of skin and subcutaneous tissues from manual indentation data,” vol. 5, pp. 2246–2249, *IEEE*.
- [107] M. Shojaeizadeh, V. Spartacus, and C. J. Sparrey, “A constitutive model to characterize in vivo human palmar tissue,” *Journal of Biomechanical Engineering*, vol. 145, 2 2023.
- [108] B. Rashid, M. Destrade, and M. D. Gilchrist, “Mechanical characterization of brain tissue in compression at dynamic strain rates,” *Journal of the Mechanical Behavior of Biomedical Materials*, vol. 10, pp. 23–38, 6 2012.

- [109] M. T. Lee, C. Y. Wu, C. W. Chen, H. L. Cheng, C. C. Chen, and Y. W. Hsieh, “Age and sex differences in the biomechanical and viscoelastic properties of upper limb muscles in middle-aged and older adults: A pilot study,” Journal of Biomechanics, vol. 134, 3 2022.